



ATLAS Note

ANA-HDBS-2020-09-INT1

23rd January 2023



Draft version 0.1

1

2 Search for $t\bar{b}$ resonance using boosted top-quark 3 topology in the lepton+jets final state at $\sqrt{s} = 13$ 4 TeV with the ATLAS detector

5

Sato, Koji^a, Hirose, Shigeki^a, Yamauchi, Hiroki^a, Salvador Salas, Adrian^b, Riu,
6 Imma^b, Mir Martinez, Lluisa Maria^b

7

^a*University of Tsukuba (JP)*

8

^b*The Barcelona Institute of Science and Technology (BIST) (ES)*

9

A search for $t\bar{b}$ resonances with a boosted top tagging technique is presented, with focusing on the final state consisting of a single charged lepton and multiple jets as well as a top-tagged large- R jet. The analysis is based on the 139 fb^{-1} of the pp collision data at the centre-of-mass energy of 13 TeV collected with the ATLAS detector. As a hypothetical particle with spin-0(1), a charged Higgs boson (a W' boson) scenario is searched in the mass range from 1 TeV up to 5 TeV.

10

11

12

13

14

15 © 2023 CERN for the benefit of the ATLAS Collaboration.

16 Reproduction of this article or parts of it is allowed as specified in the CC-BY-4.0 license.

17 **Contents**

18	1 Introduction	7
19	2 Data and MonteCarlo Simulated Events	8
20	2.1 Data Sample	8
21	2.2 Signal Samples	8
22	2.2.1 $t\bar{b}H^+$ Samples	8
23	2.3 Background Samples	9
24	2.3.1 $t\bar{t}$ +jets	9
25	2.3.2 $t\bar{t}H$	10
26	2.3.3 $t\bar{t}V$	10
27	2.3.4 Single top	11
28	2.3.5 tH	12
29	2.3.6 Rare t processes	12
30	2.3.7 Vector bosons plus jets	13
31	2.3.8 Dibosons	13
32	2.3.9 Summary	13
33	3 Object Reconstruction	15
34	3.1 Electrons	15
35	3.2 Muons	15
36	3.3 Taus	15
37	3.4 Small- R jets and b -tagging	15
38	3.5 Large- R jets and top-tagging	16
39	3.6 Overlap Removal	16
40	4 Analysis Strategy	18
41	4.1 Event Selection	18
42	4.1.1 Signal region (SR)	18
43	4.1.2 Control region (CR)	19
44	4.1.3 Summary	20
45	4.2 Multivariable analysis using BDT	21
46	4.2.1 Signal and background definition in BDT training	21
47	4.2.2 BDT training settings	22
48	4.2.3 Input variables in BDT	23
49	4.2.4 Results of BDT training	25
50	5 Background modeling	30
51	5.1 Blind strategy	30
52	5.2 Data/MC comparison for BDT input variables	30
53	5.3 Data/MC comparison for BDT distributions	32
54	6 Systematics Uncertainties	37
55	6.1 Luminosity and pile-up modeling	37
56	6.1.1 Luminosity	37
57	6.1.2 Pile-up modeling	37

58	6.2	Reconstructed objects	37
59	6.2.1	Charged leptons	37
60	6.2.2	Small- R jets, Large- R jets	39
61	6.3	Signal modeling	41
62	6.3.1	H^+ signal	41
63	6.4	Background modeling	41
64	6.4.1	$t\bar{t}$ +jets	41
65	6.4.2	Other backgrounds	43
66	7	Profile Likelihood Fit (Without reweighting)	45
67	7.1	Method	45
68	7.2	Pruning and smoothing of systematic uncertainties	45
69	7.3	Asimov fit results	46
70	7.4	Post-fit plots for Asimov fit	63
71	7.5	Asimov fit results summary	67
72	7.6	Upper cross-section limits as a function of the H^+ mass	68
73	8	Test of tbW' generation	69
74	8.1	tbW' MC generation in private	69
75	8.2	Kinematics study in truth level	69
76	8.2.1	Reconstructed truth objects	69
77	8.2.2	Event selection	70
78	8.2.3	Kinematics comparison with tbH^+ events	70
79	9	Summary and Conclusions	76
80	Appendices		85
81	A	TOPQ1 DAOD list	85
82	A.1	Data	85
83	A.2	$\bar{t}bH^+$	85
84	A.3	$t\bar{t}$ + jets	85
85	A.4	$t\bar{t}H$	86
86	A.5	$t\bar{t}V$	87
87	A.6	Single top	87
88	A.7	tH	88
89	A.8	Rare t processes	88
90	A.9	Vector bosons plus jets	88
91	A.9.1	W + jets	88
92	A.9.2	Z + jets	89
93	A.10	Diboson	91
94	B	Signal/background comparisons	92
95	B.1	BDT input variables	92
96	B.2	BDT output	94

97	C Pruning	98
98	C.1 Asimov fit	98

99 List of contributions

Sato, Koji	Analysis contact, supervision of Hiroki
Hirose, Shigeki	Analysis contact, ntuple production, BDT training, MC production, supervision of Hiroki
Yamauchi, Hiroki	Main analyser: ntuple production, fit studies and limits extraction
100 Salvador Salas, Adrian	Main analyser of resolved analysis, providing technical support; ntuple production
Riu, Imma	Signal AODs and TOPQ1s production; provision of other technical support from resolved analysis
101 Mir Martinez, Lluisa Maria	Monte Carlo production

102 **Remaining to do**

103 **The reweighting method:** A complete proposal is to be discussed at the EB request (HBSM meeting) on
104 21st July, and incorporate comments and discussions there for the method, summarize them in the
105 note in 1-2 weeks after the meeting.

106 **W' MC production:** Validations are to be finalized by the end of July so that the MC generator can be
107 implemented into the ATLAS official software. We aim for finishing the MC production as well as
108 limit evaluations by the end of September. This is to be done in parallel to EB review, as agreed with
109 the HBSM / HDBS conveners.

110 **Theoretical interpretation:** Interpret limits in terms of the theoretical H+/W' scenarios, such as hMSSM
111 and XXX. This will be done by the end of September.

112 **Version log with major updates:**

113 1 Introduction

114 The discovery of a neutral boson with a measured mass around 125 GeV at the Large Hadron Collider
 115 (LHC) in 2012 [1–3], opens the question whether this is the Higgs boson of the Standard Model (SM)
 116 or part of an extended scalar sector. Indeed, charged Higgs bosons¹ are predicted in several extensions
 117 of the SM, which add a second doublet [4–7] or triplets [7–11] to its scalar sector. In CP-conserving
 118 Two-Higgs-Doublet Models (2HDMs) H^+ production and decay at tree level depend on its mass and
 119 two parameters: the mixing angle α of the neutral CP-even Higgs bosons, and the ratio of the vacuum
 120 expectation values of the two Higgs doublets ($\tan \beta$).

121 For H^+ masses above the top-quark mass the leading production mode is $gg \rightarrow tbH^+$ and, close to the
 122 alignment limit when $\cos(\beta - \alpha) \approx 0$, the dominant decay mode is $H^+ \rightarrow tb$. For lower H^+ masses, the
 123 dominant decay mode is $H^+ \rightarrow \tau\nu$, as well as for large values of $\tan \beta$ irrespective of the charged Higgs
 124 mass. Therefore, the two decay modes naturally complement each other in searches for charged Higgs
 125 bosons.

126 The ATLAS and CMS collaborations have searched for charged Higgs bosons in pp collisions at $\sqrt{s} = 7, 8$
 127 and 13 TeV, probing the mass range below the top-quark mass in the $\tau\nu$ [12–17], cs [18, 19], and cb [20]
 128 decay modes, as well as above the top-quark mass in the $\tau\nu$ and tb decay modes [14, 16, 17, 21–27]. In
 129 addition, $H^+ \rightarrow WZ$ was searched for in the vector-boson-fusion production mode [28, 29]. No evidence for
 130 charged Higgs bosons was found in any of these searches.

131 This note presents a search for H^+ production in the $H^+ \rightarrow tb$ decay mode using pp collisions at $\sqrt{s} = 13$
 132 TeV. Events with one charged lepton ($l = e, \mu$) and jets in the final state are considered. Compared with the
 133 previous analysis using the same final state and the dataset [24] (so-called ‘resolved analysis’), boosted
 134 top tagging technique is used to identify a hadronically decaying top quark originated from the decay
 135 of the heavy H^+ . This technique allows to improve sensitivities in the high mass regions, where all top
 136 decay products are merged into a single large jet, and therefore cannot be reconstructed in the resolved
 137 analysis [24]. To separate signal from SM background, multivariate discriminants are employed in the
 138 regions where the signal rate is expected to be largest. Limits on the $H^+ \rightarrow tb$ production cross-section are
 139 set by a simultaneous fit of BDT distributions.

140 Furthermore, the analysis technique is extended to a search for the $W' \rightarrow tb$ decay, where W' is produced in
 141 association with tb .

142 The analysis replies on ATLAS official background as well as requested H^+ and W' signal samples, as
 143 detailed in Section 2, with the TOPQ1 derivation. The ntuples are produced using the TTHbbAnalysis
 144 software package.² These ntuples are used as inputs to TRExFitter to perform statistical analysis.³

¹ Charge-conjugate is implied elsewhere in this note.

² https://gitlab.cern.ch/atlasHTop/TTHbbAnalysis/-/tree/user/hyamauch/pflow_dev_HplusBoosted

³ <https://gitlab.cern.ch/hyamauch/TRExFitter>

145 2 Data and MonteCarlo Simulated Events

146 2.1 Data Sample

147 This analysis uses pp collision data collected from 2015 to 2018 by the ATLAS detector at $\sqrt{s} = 13$ TeV.
 148 Selected events are recorded using unprescaled triggers, as detailed in Table 1. Only runs with stable
 149 colliding beams and all ATLAS subsystems operational are used. These are summarized in the Good
 150 Run Lists (GRL) shown in Table 2, together with the integrated luminosity collected each year. The total
 151 integrated luminosity is 139 fb^{-1} [30].

Year	Single-electron triggers
2015	e24_lhmedium_L1EM20VH_OR_e60_lhmedium_OR_e120_lhloose
2016-2018	e26_lhtight_nod0_ivarloose_OR_e60_lhmedium_nod0_OR_e140_lhloose_nod0

(a)

Year	Single-muon triggers
2015	mu20_iloose_L1MU15_OR_mu50
2016-2018	mu26_ivarmedium_OR_mu50

(b)

Table 1: Single-electron (a) and single-muon (b) trigger menus used depending on the year of data-taking.

Year	Luminosity (pb^{-1})	GRL
2015	3219.6	data15_13TeV/20170619/physics_25ns_21.0.19.xml
2016	32988.1	data16_13TeV/20180129/physics_25ns_21.0.19.xml
2017	44307.4	data17_13TeV/20180619/physics_25ns_Triggerno17e33prim.xml
2018	58450.1	data18_13TeV/20190318/physics_25ns_Triggerno17e33prim.xml

Table 2: Integrated luminosity for each year of data-taking, computed with the OffLumi-13TeV-010 luminosity tag [31], together with the corresponding GRLs [32].

152 2.2 Signal Samples

153 2.2.1 $\bar{t}bH^+$ Samples

154 The H^+ signal samples are generated with MadGraph5_aMCatNLO (MG5_aMC) [33], which is a generator
 155 based on a four-flavor scheme (4FS) next-to-leading order (NLO) in QCD [34]. The NNPDF2.3NLO
 156 [35] parton distribution function (PDF) set is used. ⁴ The width of the H^+ is set to zero. Dynamic QCD
 157 factorisation and renormalisation scales (μ_f and μ_r) are set to $\frac{1}{3} \sum_i \sqrt{m(i)^2 + p_T(i)^2}$, where i runs over the
 158 final state particles (H^+ , t and b) used in the generation. The events are showered with Pythia 8.212 [37]
 159 with the A14 [38] set of underlying-event related parameters tuned to ATLAS. Ten different H^+ mass points
 160 between 1000 and 5000 GeV are generated as detailed in Table 3. The table also shows cross sections from

⁴ The samples with masses of 4 and 5 TeV are generated using NNPDF3.0NLO [36] PDF set.

¹⁶¹ MG5_aMC and Santander-matched cross sections for 2HDM type-II (a la MSSM), but without SUSY
¹⁶² QCD corrections [33, 39–41]. All samples are fully simulated with the proportions of mc16a, mc16d and
¹⁶³ mc16e corresponding to the amount of data recorded in the 2015–2016, 2017 and 2018 data-taking years.

DSID	H^+ mass [GeV]	Size	$\sigma^{\text{MG5_aMC}}$ [fb]	$\sigma_{\tan\beta=1}^{\text{MSSM}}$ [fb]	$\sigma_{\tan\beta=60}^{\text{MSSM}}$ [fb]
450004	1000	1.0M	3.28	40.9	37.8
450598	1200	1.0M	1.31	16.4	15.1
450599	1400	1.0M	5.62×10^{-1}	7.1	6.5
450600	1600	1.2M	2.54×10^{-1}	3.2	3.0
450601	1800	1.3M	1.21×10^{-1}	1.5	1.4
450602	2000	1.9M	5.90×10^{-2}	0.8	0.7
451490	2500	1.9M	1.11×10^{-2}	<i>Not available</i>	
451491	3000	1.9M	2.34×10^{-3}	<i>Not available</i>	
508710	4000	1.9M	9.75×10^{-5}	<i>Not available</i>	
508711	5000	1.9M	4.28×10^{-6}	<i>Not available</i>	

Table 3: Generated H^+ samples. All samples are simulated with FullSim and available in the appropriate proportions of mc16a, mc16d and mc16e. The cross-section values for $\tan\beta = 1$ or $\tan\beta = 60$ take into account the production of H^\pm .

¹⁶⁴ The W' sample is produced only privately at this point. In this version of the note, all information regarding
¹⁶⁵ W' is summarised in Section 8.

¹⁶⁶ 2.3 Background Samples

¹⁶⁷ 2.3.1 $t\bar{t}$ +jets

¹⁶⁸ The production of $t\bar{t}$ events is modeled using the PowhegBox [42–45] v2 generator, which provides matrix
¹⁶⁹ element (ME) at NLO in the strong coupling constant (α_S) with the NNPDF3.0NLO PDF set [36] and
¹⁷⁰ the h_{damp} parameter ⁵ set to $1.5m_{\text{top}}$ [46]. The functional form of μ_f and μ_r is set to the default scale
¹⁷¹ $\sqrt{m_t^2 + p_{T,t}^2}$. The events are showered with Pythia 8.230 [47].

¹⁷² The uncertainty due to initial-state-radiation (ISR) is estimated using weights in the ME and in the parton
¹⁷³ shower (PS). To simulate higher parton radiation μ_f and μ_r are varied by a factor of 0.5 in the ME while
¹⁷⁴ using the *Var3c* upward variation from the A14 tune. For lower parton radiation, μ_f and μ_r varied by a
¹⁷⁵ factor of 2.0 while using the *Var3c* downward variation in the PS. The impact of final-state-radiation (FSR)
¹⁷⁶ is evaluated using PS weights which vary μ_r for QCD emission in the FSR by a factor of 0.5 and 2.0,
¹⁷⁷ respectively. The impact of the PS and hadronisation model is evaluated by changing the showering of the
¹⁷⁸ nominal PowhegBox events from Pythia to Herwig 7.04 [48, 49].

¹⁷⁹ To assess the uncertainty due to the choice of the matching scheme, the Powheg sample is compared to a
¹⁸⁰ sample of events generated with MG5_aMC v2.6.0 and the NNPDF3.0NLO PDF set showered with Pythia

⁵ The h_{damp} parameter controls the transverse momentum of the first additional emission beyond the LO Feynman diagram in the parton shower and therefore regulates the high- p_T emission against which the $t\bar{t}$ system recoils.

181 8.230. The shower starting scale has the functional form $\mu_q = H_T/2$ [50], where H_T is defined as the scalar
 182 sum of the p_T of all outgoing partons. Choice of μ_f and μ_r is the same as that for the Powheg setup.

183 To enhance the statistics in the phase-space relevant for this analysis, for all the samples described above,
 184 dedicated filtered samples were produced, requiring b - or c -hadrons in addition to those arising from the
 185 decays of the top quarks, as follows:

- 186 • One sample was produced with at least two additional b -hadrons with $p_T > 15$ GeV.
- 187 • One sample was produced with at least one additional b -hadron with $p_T > 5$ GeV and failing the
 188 previous requirement.
- 189 • One sample was produced with at least one additional c -hadron with $p_T > 15$ GeV and failing the
 190 previous two requirements.

191 The combined use of the unfiltered and filtered samples is done by assuring no overlap between them (by
 192 the use of the heavy flavour filter flag, *TopHeavyFlavorFilterFlag*) and weighted with the appropriate
 193 cross-section and filter efficiencies.

194 2.3.2 $t\bar{t}H$

195 The production of $t\bar{t}H$ events is modeled in the 5F scheme using PowhegBox [51] at NLO in α_S with
 196 the NNPDF3.0NLO PDF set. The h_{damp} parameter is set to $3/4 \times (m_t + m_{\bar{t}} + m_H) = 352.5$ GeV. The
 197 events are showered with Pythia 8.230. The uncertainties due to ISR, FSR, PS and hadronisation model,
 198 as well as that due to the matching scheme, are evaluated with the same procedures used for the $t\bar{t}$ + jets
 199 background.

200 2.3.3 $t\bar{t}V$

201 The production of $t\bar{t}V$ events is modeled using the MG5_aMC v2.3.3 generator, which provides ME at
 202 NLO in α_S with the NNPDF3.0NLO PDF set. The functional form of μ_f and μ_r is set to the default scale
 203 $0.5 \times \sum_i \sqrt{m_i^2 + p_{T,i}^2}$ where the sum runs over all the particles generated from the ME calculation. The
 204 events are showered with Pythia 8.210.

205 Additional $t\bar{t}V$ samples are produced with Sherpa 2.2.0 [52] at LO accuracy, using the MEPS@LO setup
 206 [53, 54] with up to one additional parton for the $t\bar{t}V$ sample and two additional partons for the others. A
 207 dynamic μ_r is used, defined similarly to that of the nominal MG5_aMC+Pythia samples. The CKKW
 208 matching scale of the additional emissions is set to 30 GeV. The default Sherpa 2.2.0 PS is used along with
 209 the NNPDF3.0NNLO PDF set.

210 **2.3.4 Single top**

211 ***t*-channel**

212 Single-top *t*-channel production is modeled using the PowhegBox v2 generator, which provides ME
 213 at NLO in α_S in the 4F scheme with the NNPDF3.0NLOnf4 PDF set. The functional form of μ_f and
 214 μ_r is set to $\sqrt{m_b^2 + p_{T,b}^2}$, following the recommendation of Ref. [55]. The events are showered with
 215 Pythia 8.230.

216 The impact of the PS and hadronisation model is evaluated by comparing the nominal generator
 217 setup with a sample produced with the PowhegBox v2 generator at NLO in QCD in the 4FS using
 218 the NNPDF3.0NLOnf4 PDF set. The same events produced for the nominal PowhegBox+Pythia8
 219 sample are used. The events are showered with Herwig 7.04.

220 To assess the uncertainty due to choice of the matching scheme, the nominal sample is compared
 221 to a sample generated with the MG5_aMC v2.6.2 generator at NLO in QCD in the 4FS, using the
 222 NNPDF3.0NLOnf4 PDF set. Top quarks are decayed at LO using MadSpin [56, 57] to preserve all
 223 spin correlations. The events are showered with Pythia 8.230.

224 ***s*-channel**

225 Single-top *s*-channel production is modeled using the PowhegBox v2 generator, which provides ME
 226 at NLO in α_S in the 5F scheme with the NNPDF3.0NLO PDF set. The functional form of μ_f and μ_r
 227 is set to the default scale, which is equal to the top quark mass. The events are showered with Pythia
 228 8.230.

229 The impact of the PS and hadronisation model is evaluated by comparing the nominal generator
 230 setup with a sample produced with the PowhegBox v2 generator at NLO in QCD in the 5FS using the
 231 NNPDF3.0NLO PDF set. The same events produced for the nominal PowhegBox+Pythia8 sample
 232 are used. The events are showered with Herwig 7.04.

233 To assess the uncertainty due to choice of the matching scheme, the nominal sample is compared
 234 to a sample generated with the MG5_aMC v2.6.2 generator at NLO in QCD in the 5FS, using
 235 the NNPDF3.0NLO PDF set. Top quarks are decayed at LO using MadSpin to preserve all spin
 236 correlations. The events are showered with Pythia 8.230.

237 ***tW***

238 Single-top *tW* associated production is modeled using the PowhegBox v2 generator, which provides ME
 239 at NLO in α_S in the 5F scheme with the NNPDF3.0NLO PDF set. The functional form of μ_f and μ_r
 240 is set to the default scale, which is equal to the top quark mass. The diagram removal scheme
 241 [58] is employed to handle the interference with $t\bar{t}$ production [46]. The events are showered with
 242 Pythia 8.230.

243 The nominal Powheg+Pythia8 sample is compared to an alternative sample generated using the
 244 diagram subtraction scheme [46, 58] to estimate the uncertainty due to the interference with $t\bar{t}$
 245 production.

246 The impact of the PS and hadronisation model is evaluated by comparing the nominal generator
 247 setup with a sample produced with the Powheg v2 generator at NLO in QCD in the 5FS using the
 248 NNPDF3.0NLO PDF set. The same events produced for the nominal Powheg+Pythia8 sample are
 249 used. The events are showered with Herwig 7.04.

250 To assess the uncertainty due to the choice of the matching scheme, the nominal sample is compared
 251 to a sample generated with the MG5_aMC v2.6.2 generator at NLO in QCD in the 5FS, using the
 252 NNPDF2.3NLO PDF set. The events are showered with Pythia 8.230.

253 **2.3.5 tH**

254 **$tHjb$ production**

255 The production of $tHjb$ events is modeled in the 4F scheme using the MG5_aMCv2.6.0 with
 256 the NNPDF3.0NLOnf4 PDF set. The functional form of μ_f and μ_r is set to the default scale
 257 $1/2 \times \sum_i \sqrt{m_i^2 + p_{T,i}^2}$, where the sum runs over all the particles generated from the ME calculation.
 258 The shower starting scale has the functional form $\mu_q = H_T/2$, where H_T is defined as the scalar sum
 259 of the p_T of all outgoing partons. The events are showered with Pythia 8.230.

260 **tHW production**

261 The production of tHW events is modeled in the 5F scheme using the MG5_aMCv2.6.2 with the
 262 NNPDF3.0NLO PDF set. The functional form μ_f and μ_r is set to the default scale $1/2 \times \sum_i \sqrt{m_i^2 + p_{T,i}^2}$
 263 where the sum runs over all the particles generated from the ME calculation. The shower starting
 264 scale has the functional form $\mu_q = H_T/2$, where H_T is defined as the scalar sum of the p_T of all
 265 outgoing partons. The events are showered with Pythia 8.235.

266 **2.3.6 Rare t processes**

267 **tZq**

268 The tZq MC samples [59] are generated at LO in α_S using MG5_aMC 2.3.3 in the 4F scheme,
 269 with the CTEQ6L1 [60] LO PDF set. Following the recommendations taken from Ref. [55], the
 270 renormalisation and factorisation scales are set to $4 \times \sum_b \sqrt{m_i^2 + p_{T,b}^2}$, where the b -quark is the one
 271 coming from the gluon splitting. The events are showered with Pythia 8.212.

272 **tZW**

273 The tZW sample is simulated using the MG5_aMC v2.3.3 generator at NLO in α_S with the
 274 NNPDF3.0NLO PDF set. The top quark is decayed inclusively while the Z boson decays to a pair of
 275 leptons, by means of Pythia 8.212. The 5F scheme is used where all the quark masses are set to zero,
 276 except for the top quark. μ_f and μ_r are set to the top quark mass. The DR1 scheme [58] is employed
 277 to handle the interference between tWZ and ttZ , and is applied to the tWZ sample.

278 **4 tops**

279 The production of 4 tops events is modeled using the MG5_aMC v2.3.3 generator, which provides
 280 ME at NLO in α_S with the NNPDF3.1NLO PDF set. The functional form of μ_f and μ_r is set to
 281 $0.25 \times \sum_i \sqrt{m_i^2 + p_{T,i}^2}$, where the sum runs over all the particles generated from the ME calculation,
 282 following the Ref.[61]. The events are showered with Pythia 8.230.

283 2.3.7 Vector bosons plus jets

284 QCD vector bosons plus jets production is simulated with the Sherpa v2.2.1 PS Monte Carlo generator. In
285 this setup, NLO-accurate ME for up to two jets, and LO-accurate ME for up to four jets are calculated with
286 the Comix [62] and OpenLoops [63, 64] libraries. The default Sherpa PS [65] based on Catani-Seymour
287 dipoles and the cluster hadronisation model [66] are used. They employ the dedicated set of tuned parameters
288 developed by the Sherpa authors for this version based on the NNPDF3.0nnlo set. The NLO ME of a
289 given jet-multiplicity are matched to the PS using a colour-exact variant of the MC@NLO algorithm [67].
290 Different jet multiplicities are then merged into an inclusive sample using an improved CKKW matching
291 procedure [53, 54], which is extended to NLO accuracy using the MEPS@NLO prescription [68]. The
292 merging cut is set to $Q_{\text{cut}} = 20 \text{ GeV}$.

293 QCD scale uncertainties are evaluated on-the-fly [69] using 7-point variations of μ_f and μ_r in the ME. The
294 scales are varied independently by factors of 0.5 and 2 but avoiding opposite factors. PDF uncertainties for
295 the nominal PDF set are evaluated using the 100 variation replicas, as well as ± 0.001 shifts of α_S .

296 2.3.8 Dibosons

297 Diboson samples are simulated with the Sherpa v2.2 generator. In this setup multiple ME are matched
298 and merged with the Sherpa PS based on Catani-Seymour dipole using the MEPS@NLO prescription.
299 For semileptonically and fully leptonically decaying diboson samples, as well as loop-induced diboson
300 samples, the virtual QCD correction for ME at NLO accuracy are provided by the OpenLoops library.
301 For electroweak $VVjj$ production, the calculation is performed in the G_μ scheme, ensuring an optimal
302 description of pure electroweak interactions at the electroweak scale. All samples are generated using
303 the NNPDF3.0nnlo set, along with the dedicated set of tuned PS parameters developed by the Sherpa
304 authors.

305 2.3.9 Summary

306 The samples and their basic generation parameters are summarized in Table 4. Exact dataset names of
307 TOPQ1 DAODs are shown in App. A

Physics process	Generator	PS generator	Normalisation	PDF set
$t b H^+ (M_{H^+} \leq 3.0 \text{ TeV})$	MG5_aMC 2.6.2	Pythia 8.212	NLO	NNPDF2.3NLO
$t b H^+ (M_{H^+} = 4.0, 5.0 \text{ TeV})$	MG5_aMC 2.8.1	Pythia 8.244	NLO	NNPDF3.0NLO
$t\bar{t} + \text{jets}$	PowhegBox v2	Pythia 8.230	NNLO+NNLL	NNPDF3.0NLO
$t\bar{t}H$	PowhegBox v2	Pythia 8.230	NNLO	NNPDF3.0NLO
$t\bar{t}V$	MG5_aMC 2.3.3	Pythia 8.210	NLO	NNPDF3.0NLO
Single top t-chan.	PowhegBox v2	Pythia 8.230	aNNLO	NNPDF3.0NLOnf4
Single top s-chan.	PowhegBox v2	Pythia 8.230	aNNLO	NNPDF3.0NLO
Single top tW	PowhegBox v2	Pythia 8.230	aNNLO	NNPDF3.0NLO
$tHjb$	MG5_aMC 2.6.X	Pythia 8.230	NLO	NNPDF3.0NLOnf4
tHW	MG5_aMC 2.6.2	Pythia 8.235	NLO	NNPDF3.0NLO
tZq	MG5_aMC 2.3.3	Pythia 8.212	NLO	CTEQ6L1LO
tZW	MG5_aMC 2.3.3	Pythia 8.212	NLO	NNPDF3.0NLO
4 tops	MG5_aMC 2.3.3	Pythia 8.230	NLO	NNPDF3.1NLO
$V + \text{jets}$	Sherpa 2.2.1	Sherpa 2.2.1	NNLO	NNPDF3.0NLO
Diboson	Sherpa 2.2	Sherpa 2.2	NLO	NNPDF3.0NLO

Table 4: Nominal simulated signal and background event samples. The generator, parton shower generator and cross-section used for normalisation are shown together with the applied PDF set.

308 3 Object Reconstruction

309 3.1 Electrons

310 Electrons are reconstructed from energy clusters in the electromagnetic calorimeter matched to tracks
 311 reconstructed in the inner detector (ID) [70, 71], and are required to have $p_T > 10$ GeV and $|\eta| < 2.47$.
 312 Candidates in the barrel–endcap transition region of the calorimeter ($1.37 < |\eta| < 1.52$) are excluded.
 313 Electrons must satisfy the *tight* identification criterion based on a likelihood discriminant described in
 314 Ref. [71] and the following constraints in the longitudinal and transverse impact parameters: $|z_0| < 0.5$ mm
 315 and $|d_0|/\sigma_{d_0} < 5$. The impact parameters are defined with respect to beam line. Electrons are required to
 316 satisfy the *FCTight* isolate criteria [72].

317 3.2 Muons

318 Muons are reconstructed from either track segments or full tracks in the muon spectrometer which are
 319 matched to tracks in the ID [73]. Tracks are then re-fitted using information from both detector system.
 320 Muons are required to have $p_T > 10$ GeV and $|\eta| < 2.5$ and the following constraints in the longitudinal
 321 and transverse impact parameters: $|z_0| < 0.5$ mm and $|d_0|/\sigma_{d_0} < 3$. Muons should satisfy the *medium*
 322 identification and the *FCTightTrackOnly* isolation criteria [72].

323 3.3 Taus

324 Hadronically decaying tau leptons (τ_{had}) are distinguished from jets using the track multiplicity and the
 325 τ_{had} identification algorithm based on a recurrent neural network [74]. This algorithm exploits the track
 326 collimation, jet substructure, kinematic information and so on. These τ_{had} candidates are required to have
 327 $p_T > 25$ GeV, $|\eta| < 2.5$ and pass the *Medium τ* -identification working point. Although taus are not used in
 328 the analysis, the consistent configuration with the resolved analysis as well as the $t\bar{t}H(\rightarrow bb)$ analysis is
 329 kept.

330 3.4 Small- R jets and b -tagging

331 Jets are reconstructed using the anti- k_t clustering algorithm [75] on particle-flow objects [76] with a radius
 332 of $R = 0.4$. Jets are calibrated using the standard jet calibration procedure, which corrects the jet energy to
 333 match on average the true jet energy at particle level and applies an in-situ correction for data [77]. The
 334 jet collection name in ATLAS is `AntiKt4EMPF1lowJets_BTagging201903`. Jets are required to have
 335 $|\eta| < 2.5$ such that they are within the acceptance of the ID and the recommended jet vertex tagging (JVT)
 336 requirement [78] is applied to jets with $p_T < 60$ GeV in order to remove jets originating from pile-up.

337 Small- R jets originating from the hadronisation of b -quarks (referred to as b -jets hereafter) are identified
 338 using an algorithm based on multivariate techniques to combine information from the impact parameters
 339 of displaced tracks as well as properties of secondary and tertiary decay vertices reconstructed within the
 340 jets. In this analysis, b -tagging relies on the *DL1r* tagger [79], trained on simulated $t\bar{t}$ events, and the event
 341 selection makes use of jets b -tagged with the *DL1r* algorithm at the 70% efficiency working point.

342 3.5 Large- R jets and top-tagging

343 Top quarks with high transverse momentum ($p_T \gtrsim 2m_t$) are expected to result in decay products that are
 344 colimated. For top quarks decaying hadronically (bqq'), the three quarks may not be resolved as three
 345 separate jets. In order to reconstruct these boosted hadronically-decaying top quarks, large-radius (large- R)
 346 jets are used. The large- R jets are formed from the topological clusters of calorimeter cells which are
 347 calibrated to the hadronic energy scale using the local calibration weighting method [80], and reconstructed
 348 using the anti- k_t algorithm with radius parameter of $R = 1.0$. The jet collection name in ATLAS is
 349 `AntiKt10LCTopoTrimmedPtFrac5SmallR20Jets`. These jets are further trimmed to remove the effects
 350 of pile-up and underlying event. The trimming [81] is done by reclustering the original constituents of a
 351 large- R jet into a collection of R_{sub} subjets using k_t algorithm [82]. The subjets are then discarded if they
 352 carry less than a specific fraction (f_{cut}) of the p_T of the original large- R jet. In this analysis, the optimized
 353 values ($R_{\text{sub}} = 0.2$, $f_{\text{cut}} = 5\%$) are used [83]. The large- R jet energy and mass scale are then calibrated
 354 using correction factors derived from simulation. The mass of the large- R jets is calculated using tracking
 355 and calorimeter information, so called combined mass technique [84]. Only the large- R jets that satisfy
 356 $200 < p_T < 3000 \text{ GeV}$, $|\eta| < 2.0$ and $40 < m_{\text{comb}} < 600 \text{ GeV}$ are considered in this analysis.

357 The identification of hadronically decaying top quarks that are reconstructed as large- R jets is performed
 358 using a multivariate classification algorithm employed in a deep neural network [85]. In the kinematic
 359 region of interest in this search, a single large- R jet captures the top quark decay products, resulting in a
 360 characteristic multi-core structure within the jet, in contrast to a typical single-core structure associated
 361 with jets in multijet. In order to exploit this characteristic behaviour for the top quark identification, a
 362 multivariate top-tagging classifier was developed. The tagger uses multiple jet-level discriminants as
 363 inputs, such as calibrated jet p_T and mass, information about the dispersion of the jet constituents such as
 364 N -subjettiness [86], splitting scales [87] and energy correlation functions [88]. Top-tagging, associated
 365 scale factors and uncertainties are only provided for jets with $350 < p_T < 2500 \text{ GeV}$. The tagger used is
 366 optimized for the contained top definition, in which the signal category is defined using jets matched to a
 367 truth top quark. In addition, a truth jet matched to the reconstructed jet is required to have a mass above
 368 140 GeV and at least one b -hadron ghost matched to it.

369 In this analysis, large- R jets which pass the 80% efficiency working point of the contained top-tagging
 370 criterion ($J_{\text{top-tagged}}$) are chosen as the boosted top candidates. Especially, the leading boosted top candidate
 371 out of them is represented by $J_{\text{top-tagged}}^{\text{1st}}$ in the following sections.

372 3.6 Overlap Removal

373 In order to avoid counting a single detector response as more than one lepton or jet, the following overlap
 374 removal procedure is applied.

375 To prevent double-counting of electron energy deposits as jets, the small- R jet within $\Delta R_y = \sqrt{(\Delta y)^2 + (\Delta\phi)^2} =$
 376 0.2 of a selected electron is removed. Here, the rapidity is defined as $y = \frac{1}{2} \ln \frac{E+p_z}{E-p_z}$, where E is the energy
 377 and p_z is the longitudinal component of the momentum along the beam pipe. If the nearest small- R jet
 378 surviving that selection is within $\Delta R_y = 0.4$ of the electron, the electron is discarded. In the case that a
 379 large- R jet is found within $\Delta R = 1.0$ of the electron, the large- R jet is removed.⁶

⁶ Following the recommendation for ATLAS analyses in Run 2 [89], the overlap removal implemented in the `AssociationUtils` package [90] is based on ΔR_y . It is found more appropriate in the case of non-massless objects [91]. However, overlap removal

- 380 Muons are removed if their distance from the nearest small- R jet is within $\Delta R_y < 0.4$. This treatment
 381 reduces the background from heavy-flavor decays inside small- R jets. However, if this small- R jet has
 382 fewer than three associated tracks, the muon is kept and the small- R jet is removed instead. This avoids an
 383 inefficiency for high-energy muons undergoing significant energy loss in the calorimeter.
- 384 A τ_{had} candidate is rejected if it is within $\Delta R_y < 0.2$ from any selected electron or muon. Also, small- R
 385 jets with $\Delta R_y < 0.2$ around a τ_{had} candidate are rejected. The overlap removal with τ_{had} is applied in order
 386 to keep consistency with the $t\bar{t}H(\rightarrow bb)$ analysis as well as the $H^+ \rightarrow tb$ analysis.
- 387 Small- R jets within $\Delta R < 1.0$ of a leading top-tagged large- R jet are removed⁶ to prevent double-counting
 388 of jet energy deposits. All of the above overlap removal procedures are summarized in Table 5.

Reject	Against	Criteria
Small- R jet	Electron	$\Delta R_y < 0.2$
Electron	Small- R jet	$0.2 < \Delta R_y < 0.4$
Small- R jet	Muon	$N_{\text{track}} < 3$ in jet and $\Delta R_y < 0.4$
Muon	Small- R jet	$\Delta R_y < 0.4$
τ_{had}	Electron	$\Delta R_y < 0.2$
τ_{had}	Muon	$\Delta R_y < 0.2$
Small- R jet	τ_{had}	$\Delta R_y < 0.2$
Large- R jet	Electron	$\Delta R < 1.0$
Small- R jet	Leading top-tagged large- R jet	$\Delta R < 1.0$

Table 5: Summary of overlap removal procedures in this analysis.

for large- R jets is performed in the ttHOffline software, and is computed based on ΔR .

389 4 Analysis Strategy

390 4.1 Event Selection

391 In this analysis, two regions, “Signal region (SR)” and “Control region (CR)”, are defined according to the
 392 number of lepton, top tagged large- R jets and b -tagged small- R jets as following.

393 4.1.1 Signal region (SR)

394 Figure 1 show the feynman diagram and the schematic of boosted event topology in case of $H^+ \rightarrow tb$ event.
 395 An signal event is expected to have one $J_{\text{top-tag}}$, three b -jets and one lepton+MET. However, the b -jet
 396 originated from the gluon is typically not detected, because it tend to fly in the forward directions and
 397 therefore outside the detector acceptance. Threfore, at least two b -jets are required in this analysis.

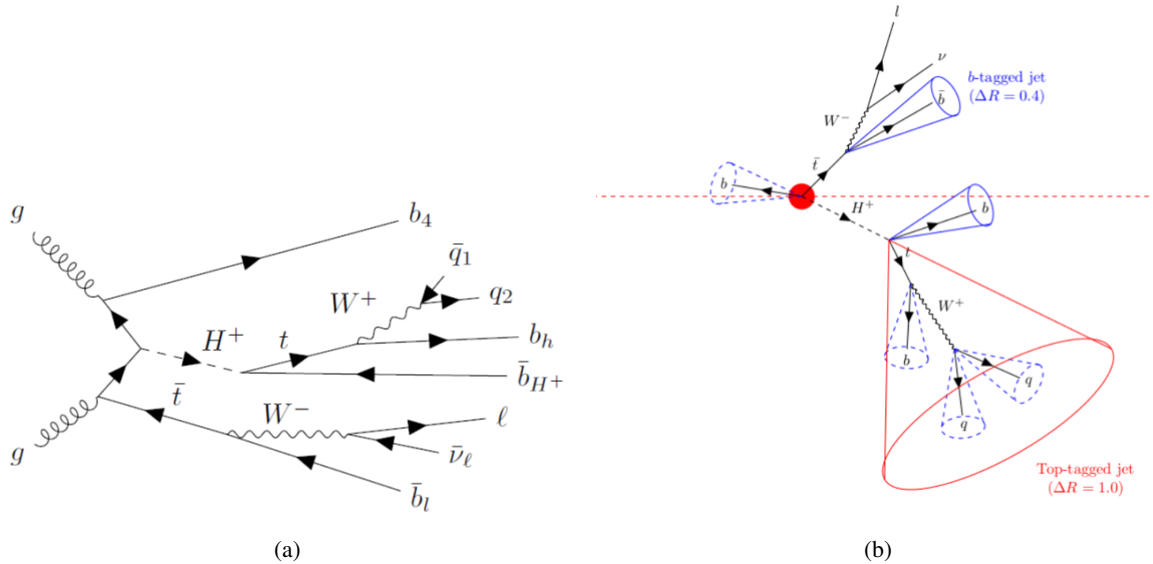


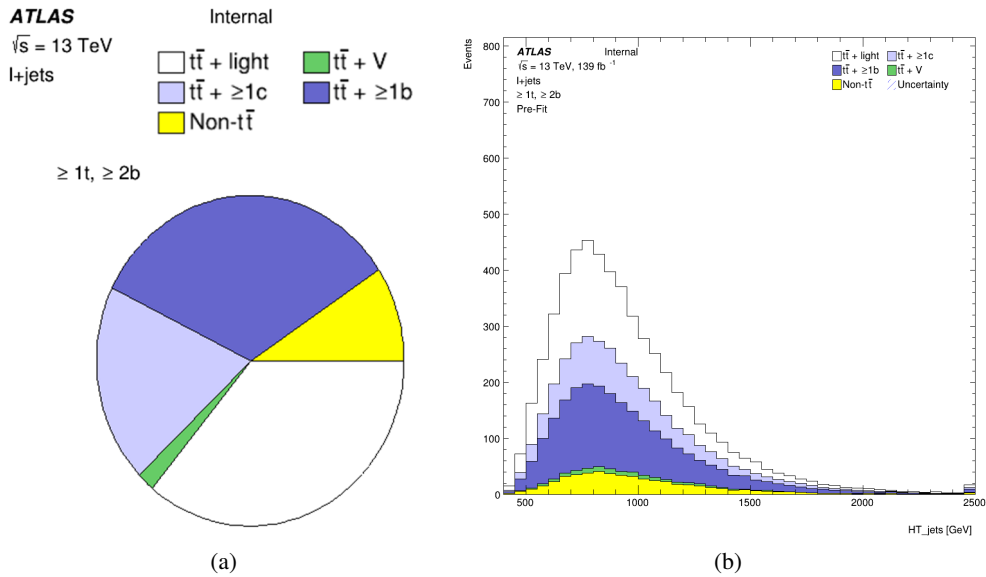
Figure 1: Feynman diagram (a) and schematic of boosted event topology (b). Signal event has at least one $J_{\text{top-tag}}$ and at least two b -tagged small- R jets.

398 To be consistent with the signal event as shown in Figure 1, events are required to have exactly one lepton
 399 (e or μ) that is matched to the one firing one of the single lepton triggers. Events are also required to have
 400 at least one top-tagged large- R jet and at least two b -tagged small- R jets. The b -jets must additionally
 401 satisfy $\Delta R(J_{\text{top-tag}}^{1st}, b\text{-jet}) > 1.0$ to ensure these b -jets are not consituent of the leading top-tagged jet. These
 402 selections are summarized in Table 6.

Cut	Criteria
leptons	Exactly 1 lepton in event
	<u>Electron</u> <u>Muon</u>
	$p_T > 27 \text{ GeV}$ $p_T > 27 \text{ GeV}$
	$ \eta < 1.37 \text{ or } 1.52 < \eta < 2.47$ $ \eta < 2.5$
Top-tagged large- R jets	≥ 1 top-tagged large-R jets
	$350 \text{ GeV} < p_T < 2500 \text{ GeV}$
	$ \eta < 2.0$
b -tagged small- R jets	≥ 2 b-tagged small-R jets
	$p_T > 25 \text{ GeV}$
	$ \eta < 2.5$
	$\Delta R(J_{\text{top-tag}}^{1\text{st}}, b\text{-jet}) > 1.0$

Table 6: Event selections in the SR.

403 Events passing the event selections in Table 6 are expected to have the boosted-topology as shown in Figure
 404 1. The expected background composition and distributions in the SR is illustrated in Figure 2. Events
 405 containing $t\bar{t}$ fully dominate the SR. In this figure, H_T^{jet} denotes the sum of p_T of $J_{\text{top-tag}}^{1\text{st}}$ and all small- R
 406 jets in event, and enhances the characteristics of the signal events which have high p_T jets from the heavy
 407 H^+ decay.

Figure 2: Background composition in the SR is shown in the pie chart (a) and the H_T^{jets} distributions (b).

408 4.1.2 Control region (CR)

409 In order to constrain the yields of events with $t\bar{t}$ in association with at least one light-flavor jet, a dedicated
 410 control region (CR) is prepared. Requirements in the CR are identical to that in the SR, except the number of
 411 b -tagged small- R jets. Exactly one b -tagged small- R jet is required in the CR in order to keep orthogonality

to the SR where two or more b -tagged small- R jets are required. The selections in the CR are summarized in Table 7.

Cut	Criteria
leptons	Same as in the SR
Top-tagged large- R jets	Same as in the SR
b -tagged small- R jets	Exactly one b -tagged small- R jet Other kinematic requirements are the same as in the SR

Table 7: Event selections in the CR.

After applying the event selections for the CR, the events mostly contain $t\bar{t}$ in association with at least one light-flavor jet. The background composition is illustrated in Figure 3. This CR is included in the profile likelihood fit discussed in Section 7.

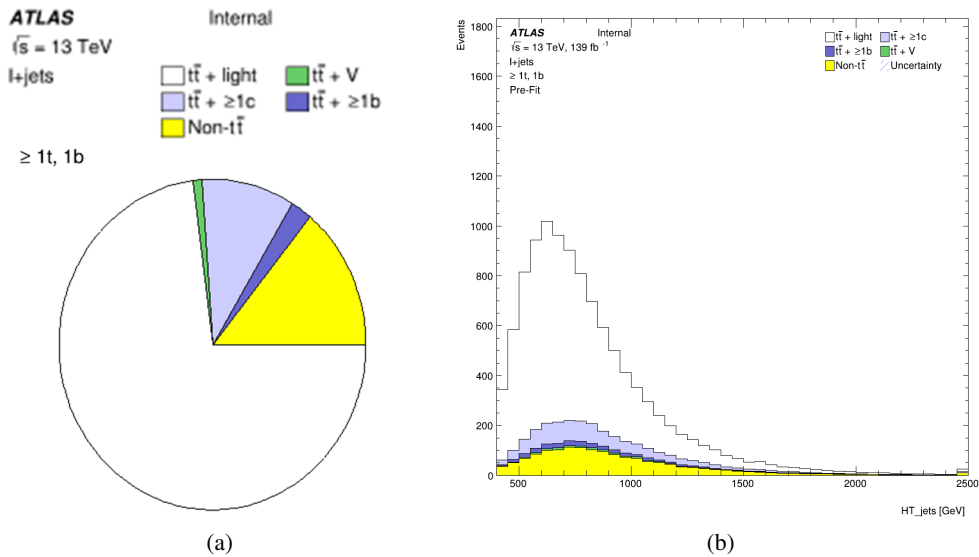


Figure 3: Background composition in the CR is shown in the pie chart (a) and the H_T^{jets} distributions (b).

4.1.3 Summary

The number of expected signal and background events in the SR and CR are shown in Table 8. The predicted number of H^+ signal events for the 1000 and 3000 GeV mass hypothesis assume $\sigma \times Br = 0.046$ pb. This is the upper limit at $M_{H^+} = 1000$ GeV obtained from the resolved analysis.

	SR	CR
$t\bar{t}$ + light	1979 ± 89	7848 ± 329
$t\bar{t}+ \geq 1c$	1070 ± 56	1052 ± 38
$t\bar{t}+ \geq 1b$	1840 ± 84	246 ± 11
$t\bar{t} + W$	38 ± 20	52 ± 27
$t\bar{t} + Z$	67 ± 34	49 ± 6
Wt channel	183 ± 93	422 ± 212
t channel	37 ± 3	63 ± 5
Other top sources	38 ± 15	11 ± 1
$VV, V+jets$	152 ± 55	1001 ± 342
$t\bar{t}H$	103 ± 4	18 ± 0
Total	5565 ± 256	10763 ± 566
H^+ 1000 GeV	58 ± 6	4 ± 0
H^+ 3000 GeV	67 ± 16	13 ± 3

Table 8: Number of expected and selected events split according to the analysis region. The quoted uncertainties include both statistical and systematic uncertainties before fitting.

421 4.2 Multivariable analysis using BDT

422 In this search, the most important background is $t\bar{t}$ + jets as discussed in Section 4.1.1. To enhance
 423 separation between signal and background, multivariable analysis is performed using Boosted Decision
 424 Trees (BDT) technique. Obtained BDT score distribution is used in the profile likelihood fit as a final
 425 discriminant (Section 7).

426 4.2.1 Signal and background definition in BDT training

427 To classify H^+ signal and $t\bar{t}$ + jets background events, BDTs are trained using the simulated H^+ signal and
 428 $t\bar{t}$ + jets background samples, as summarized in Table 9. Ten different H^+ mass hypotheses are considered
 429 in this analysis, and the training is performed on each H^+ mass hypothesis. On the other hand, the $t\bar{t}$ + jets
 430 background samples are common in each training. Since kinematics of H^+ signals become harder in higher
 431 mass hypotheses, as shown in Section 4.2.3, the BDTs trained using the higher H^+ mass samples typically
 432 have greater separation power.

H^+ mass point	DSID (Signal sample)	DSID (Background sample)
$M_{H^+} = 1000$ GeV	450004	
$M_{H^+} = 1200$ GeV	450598	$t\bar{t} + \text{jets (Inclusive):}$ [410470, 410471]
$M_{H^+} = 1400$ GeV	450599	$t\bar{t} + \text{jets (BBFilter):}$ [411073, 411076]
$M_{H^+} = 1600$ GeV	450600	
$M_{H^+} = 1800$ GeV	450601	
$M_{H^+} = 2000$ GeV	450602	$t\bar{t} + \text{jets (BFilterBBVeto):}$ [411074,411077]
$M_{H^+} = 2500$ GeV	451490	
$M_{H^+} = 3000$ GeV	451491	$t\bar{t} + \text{jets (CFilterBVeto):}$ [411075,411078]
$M_{H^+} = 4000$ GeV	508710	
$M_{H^+} = 5000$ GeV	508711	

Table 9: Signal and background samples used for BDT training.

4.2.2 BDT training settings

In order to make full use of statistics of simulation samples, 4-fold cross-validation is used. Each simulation sample is divided into four sub-datasets at random by a seed value based on the MC event number, and labeled by “TRAIN”, “VALID” and “TEST”. Two of the four sub-datasets are assigned “TRAIN”, which are used for BDT training. One of the other sub-datasets are assigend “VALID”, and is used to optimize the BDT performance. The last sample, “TEST” is used to construct a fit template. There are four possible combinations for sub-division of the samples as shown in Figure 4. The four statistically-independent BDTs are obtained from the four “TEST” sub-datasets, and they are combined into one fit template, which is used in the profile likelihood fit (Section. 7).

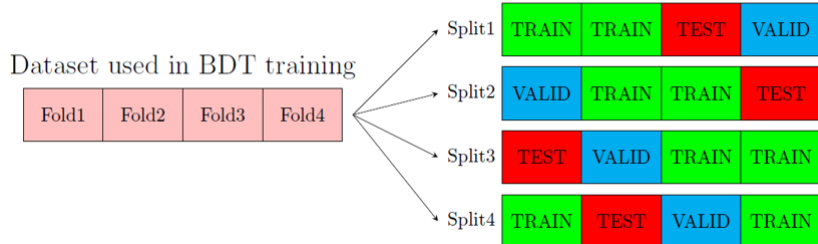


Figure 4: Scheme of 4-fold cross-validation in this analysis.

Hyperparamerters for the BDTs are summarized in Table. 10. Those hyperparameters are chosen to obtain the best sensitivity.

Configuration	
Algorithm	Gradient boosting
<i>Hyperparameters</i>	
NTrees	100
MinNodeSize	2.5
MaxDepth	3
nCuts	20

Table 10: List of hyperparameters used in the trainging of a BDT

4.2.3 Input variables in BDT

Jets originating from an H^+ decay have higher p_T comparing with $t\bar{t} + \text{jets}$ events due to its heavy mass. Additionally, correlation among jets are different between H^+ and $t\bar{t} + \text{jets}$ events because H^+ creates a resonance. The BDT is trained in order to fully exploit these kinematic characteristics. List of variables used in BDT training is summarized in Table 11. In Figure 5, each distribution in the H^+ sample with a mass of 3000 GeV is compared with the $t\bar{t} + \text{jets}$ background.

Symbol	Description
HT_jets	Scalar sum of the transverse energy of all jets
LeadingJet_pt	Leading jet p_T
Mjjj_MaxPt	Invariant mass of the jet triplet with maximum p_T
Mbb_MaxPt	Invariant mass of the b-jet pair with maximum p_T
Muu_MinR	Invariant mass of the untagged jet-pair with minimum ΔR
dRlepb_MinR	ΔR between the lepton and the pair of b-jets with smallest ΔR
dRbb_avg	Average ΔR between all b-jet pairs in the event
Centrality_all	Centrality calculated using all jets and leptons
H1_all	Second Fox-Wolfram moment calculated using all jets and leptons
LeadingTop_pt	Leading top-tagged jet p_T
LeadingTop_m	Invariant mass of leading top-tagged jet
Pt_tb	p_T of the pair of leading top-tagged jet and leading b-jet
M_tb	Invariant mass of the pair of leading top-tagged jet and leading b-jet
PtAsymm_tb	p_T asymmetry between leading top-tagged jet and leading b-jet

Table 11: List of variables included in the training of the BDT

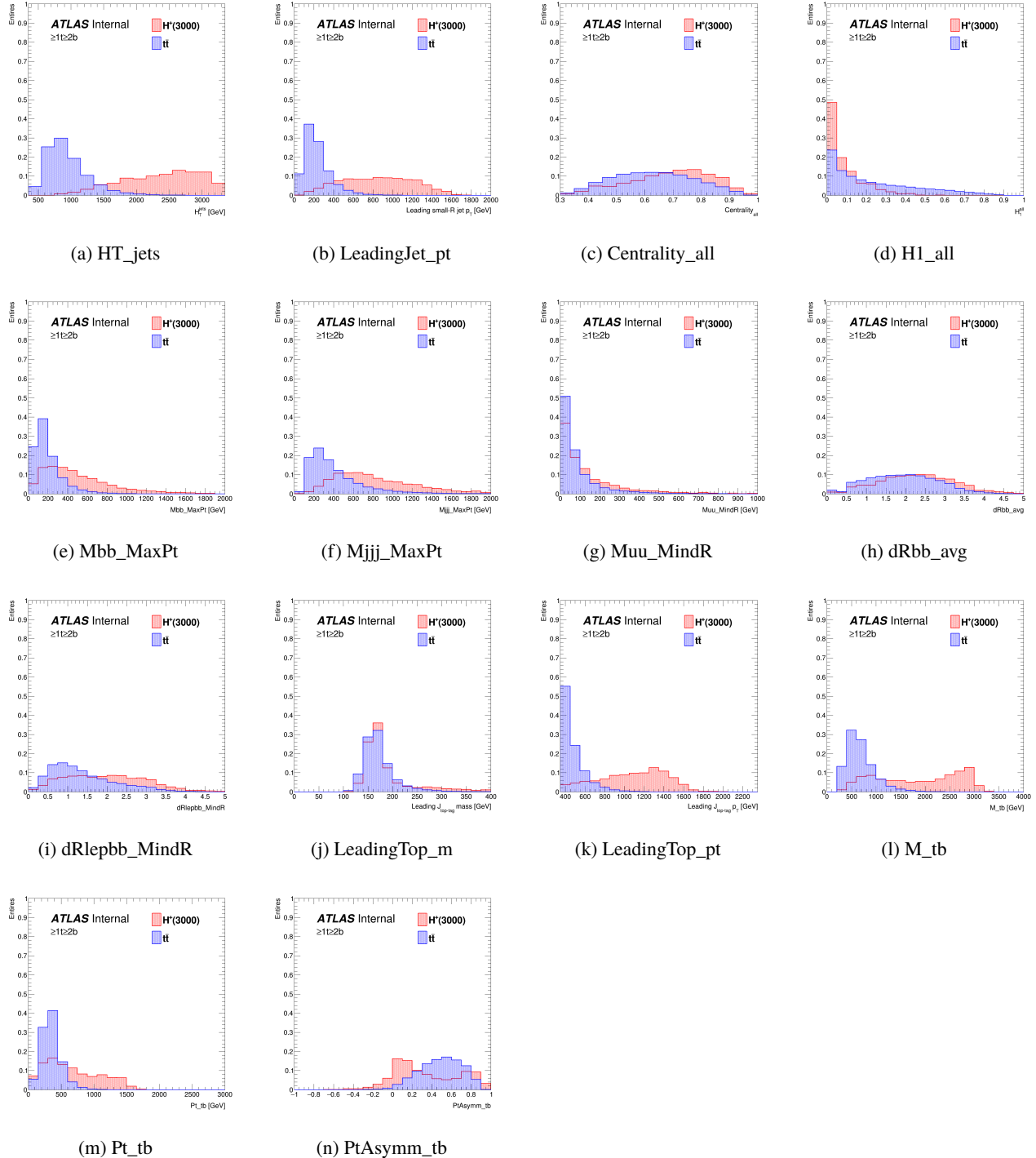


Figure 5: Comparison of input variables for BDT training between H^+ and $t\bar{t} + \text{jets}$ events under $3000 \text{ GeV } H^+$ mass hypothesis.

450 4.2.4 Results of BDT training

451 The BDT output distributions for signal and background in the analysis region for different values of the
 452 H^+ mass are shown in Figure 6 to 13, together with receiver operating characteristic (ROC) curves.

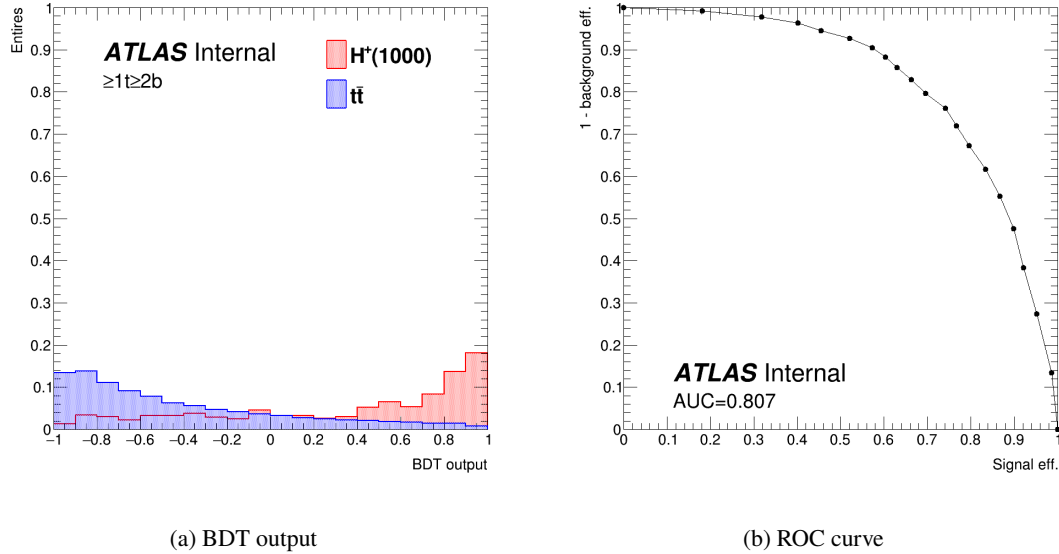


Figure 6: BDT distribution and ROC curve for the 1000 GeV H^+ mass hypothesis.

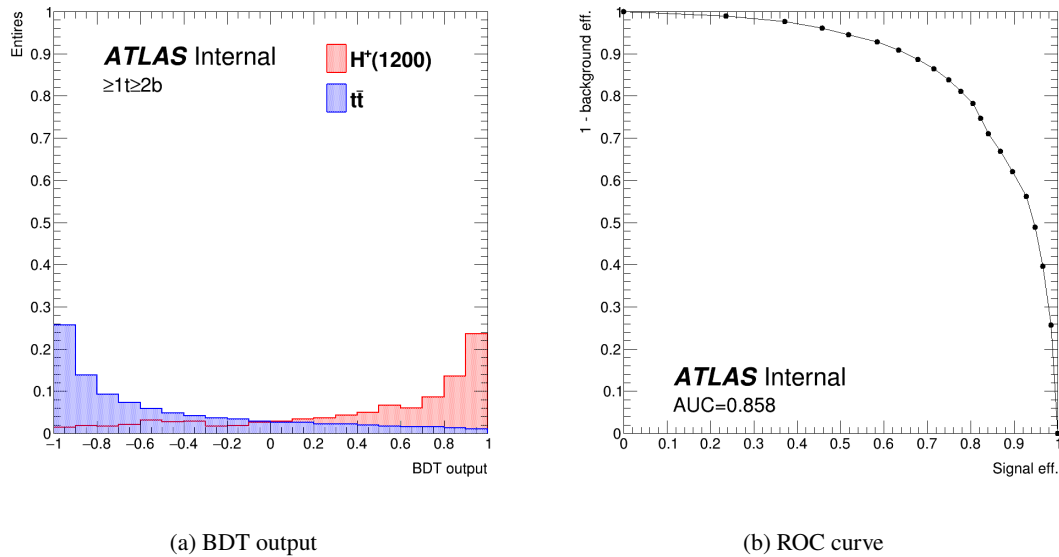


Figure 7: BDT distribution and ROC curve for the 1200 GeV H^+ mass hypothesis.

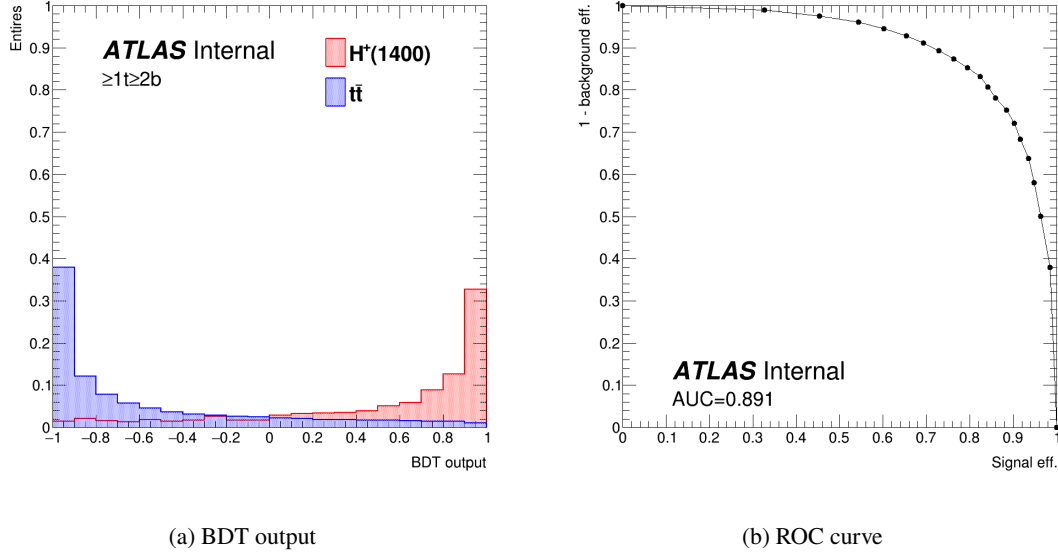


Figure 8: BDT distribution and ROC curve for the 1400 GeV H^+ mass hypothesis.

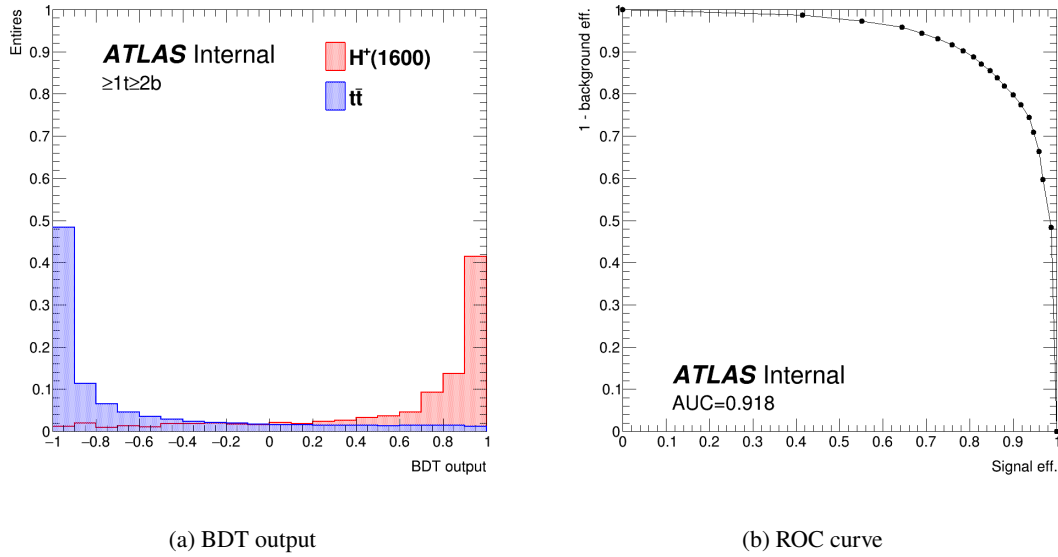


Figure 9: BDT distribution and ROC curve for the 1600 GeV H^+ mass hypothesis.

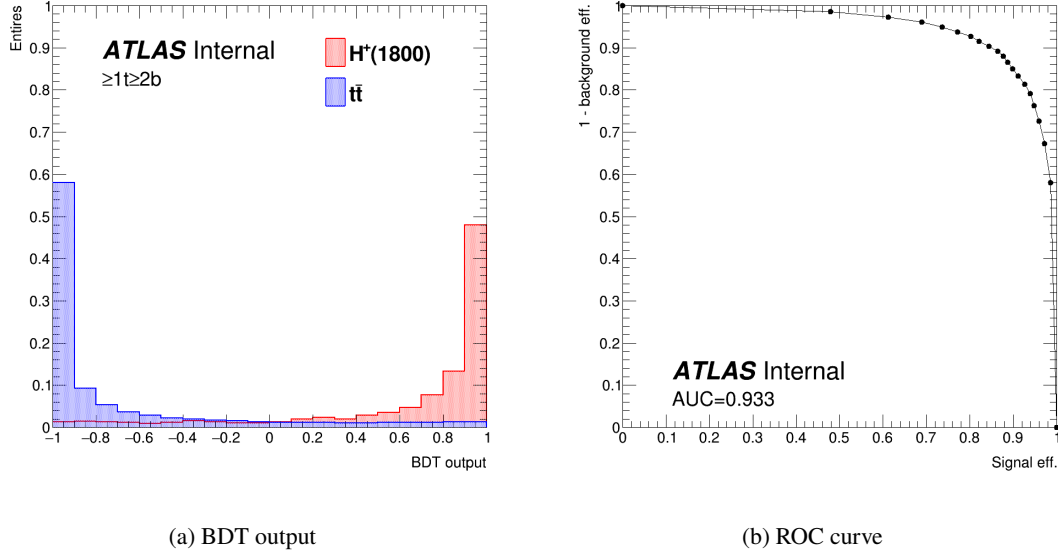


Figure 10: BDT distribution and ROC curve for the 1800 GeV H^+ mass hypothesis.

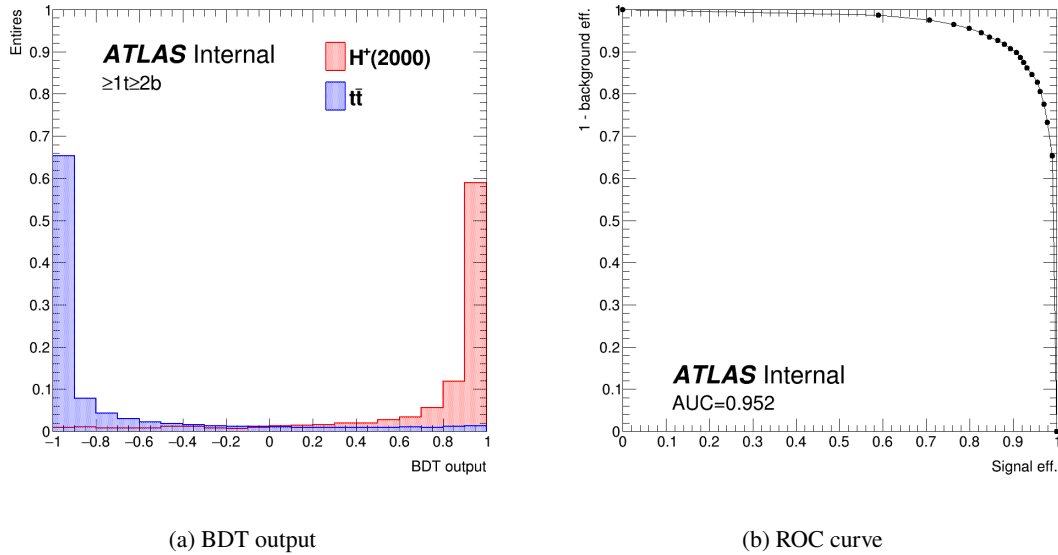


Figure 11: BDT distribution and ROC curve for the 2000 GeV H^+ mass hypothesis.

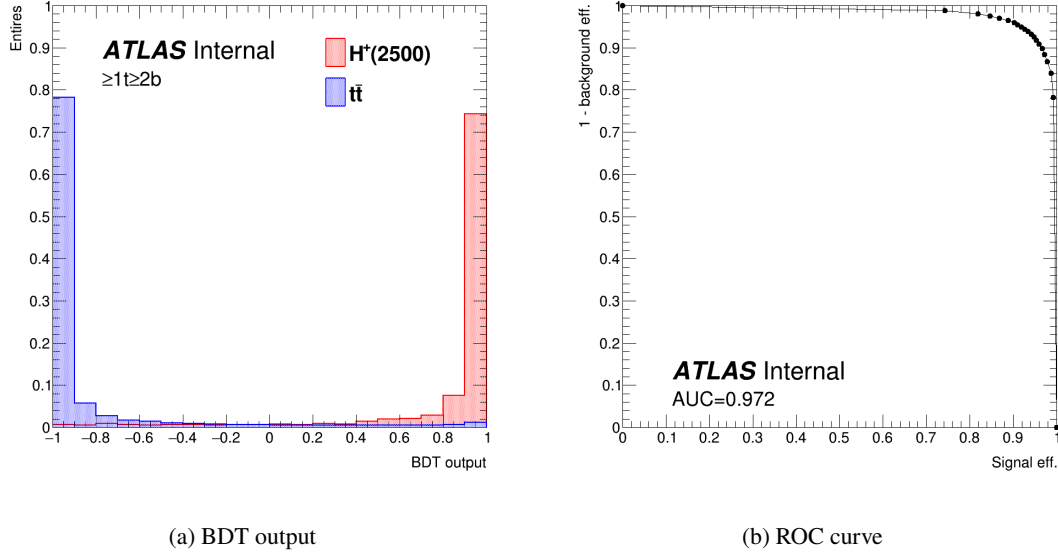


Figure 12: BDT distribution and ROC curve for the 2500 GeV H^+ mass hypothesis.

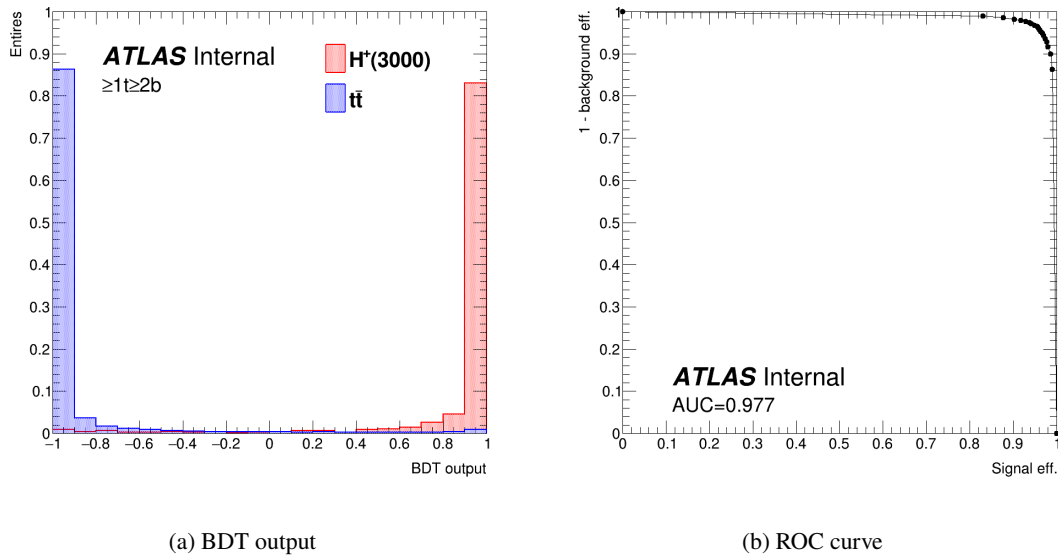


Figure 13: BDT distribution and ROC curve for the 3000 GeV H^+ mass hypothesis.

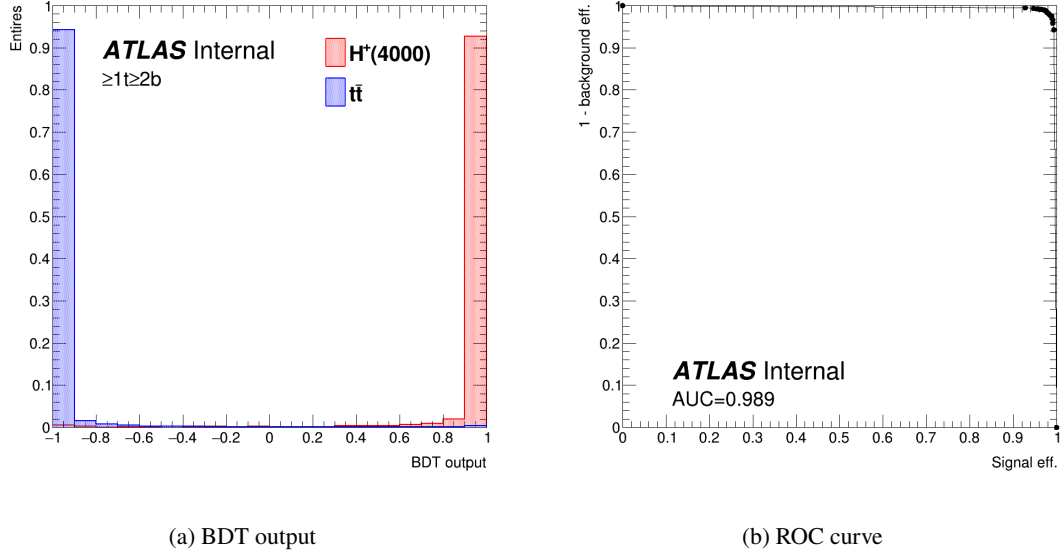


Figure 14: BDT distribution and ROC curve for the 4000 GeV H^+ mass hypothesis.

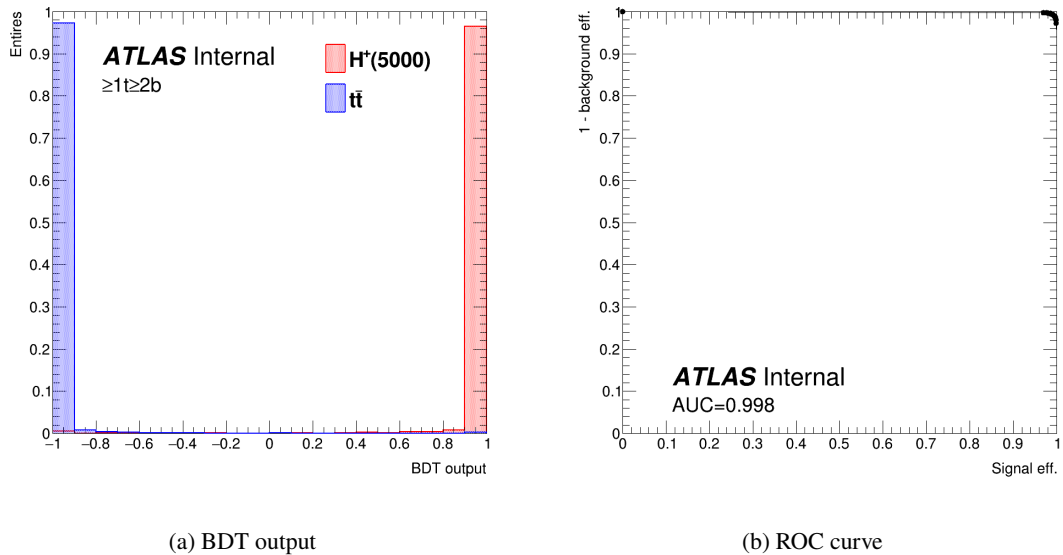


Figure 15: BDT distribution and ROC curve for the 5000 GeV H^+ mass hypothesis.

453 5 Background modeling

454 5.1 Blind strategy

455 In the following sections, modeling of kinematic distributions, in particular ones used for BDT training, of
456 the $t\bar{t}$ + jets background is checked by comparing the data and MC. In order to avoid observing signals or
457 any other biases before fixing the analysis procedure, following blinding strategy is applied. The signal to
458 noise ratio (S/B) is calculated in each bin of each distribution for all H^+ mass hypothesis (more details
459 in Appendix B). The signal cross section (σ_{signal}) on each H^+ mass hypothesis is set to 0.046 pb, which is
460 the upper limits at 1 TeV H^+ mass point obtained from the resolved $H^+ \rightarrow tb$ search [24], and therefore it
461 can be considered as the most conservative assumption. The data in bins with $S/B > 0.05$ in at least one
462 H^+ mass hypothesis are blinded when the data is compared with MC.

463 5.2 Data/MC comparison for BDT input variables

464 Figures 16 show the distributions of input variables for BDT training. Data are blinded according to
465 the blind strategy in Section 5.1. No significant difference between the data and MC is found in each
466 variable.

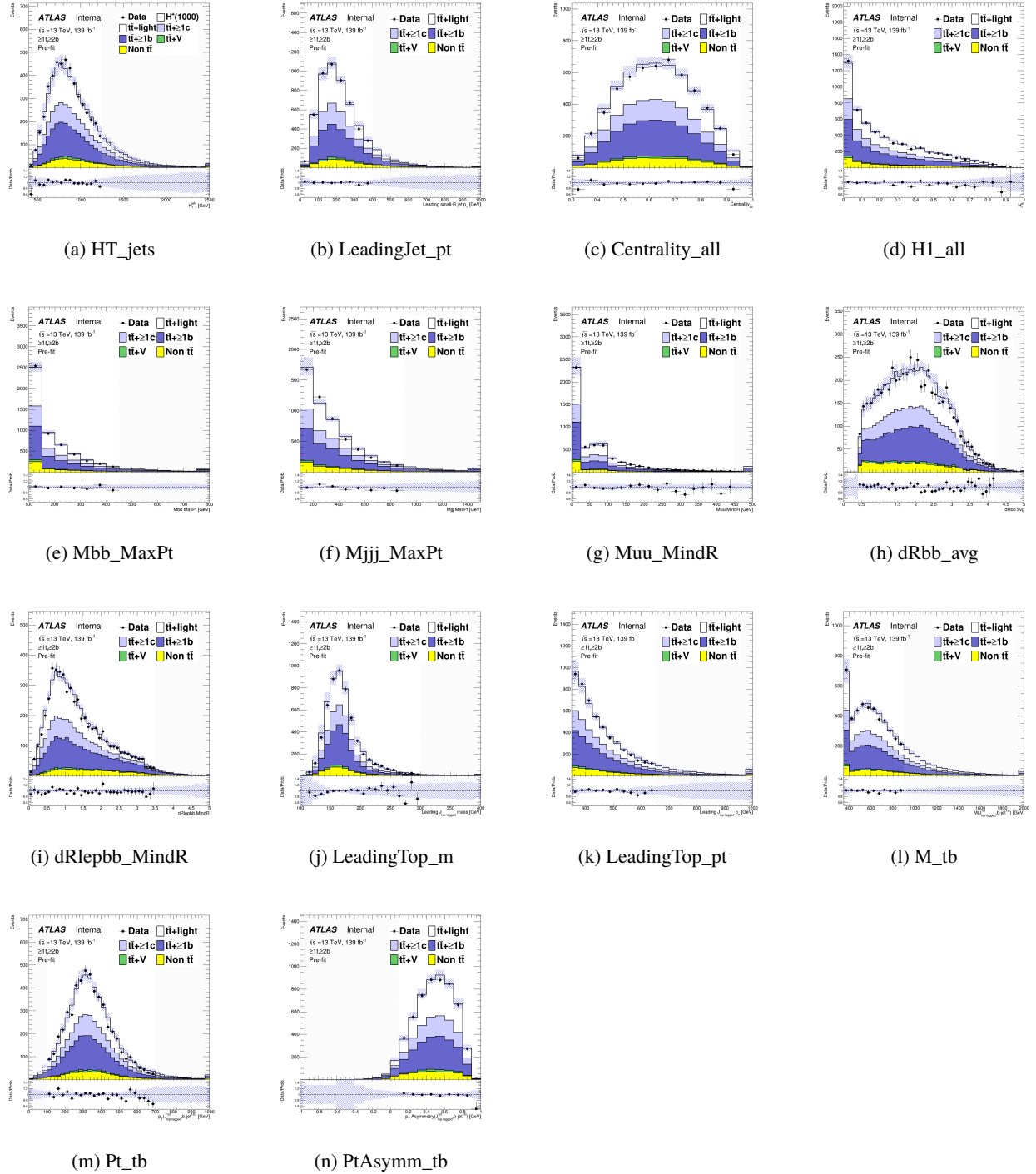


Figure 16: Comparison of the kinematic variables included in the BDT in the SR for the data and MC.

467 5.3 Data/MC comparison for BDT distributions

468 Figures 17 to 24 show the distributions of BDT output in SR and H_T^{jets} in CR. The distributions are input into
 469 the profile likelihood fit on each H^+ mass hypothesis as shown in Section 7. It is observed that the data/MC
 470 ratio tends to be lower for the high BDT score regions, which may bias search for the signal in the highest
 471 BDT bins. The reweighting to correct for the slope is discussed in Section ???. In H_T^{jets} distributions, there
 472 is no significant difference in the shape, while the normalization is significantly different. The $t\bar{t}$ + light
 473 yields are therefore determined by floating them in the fit.

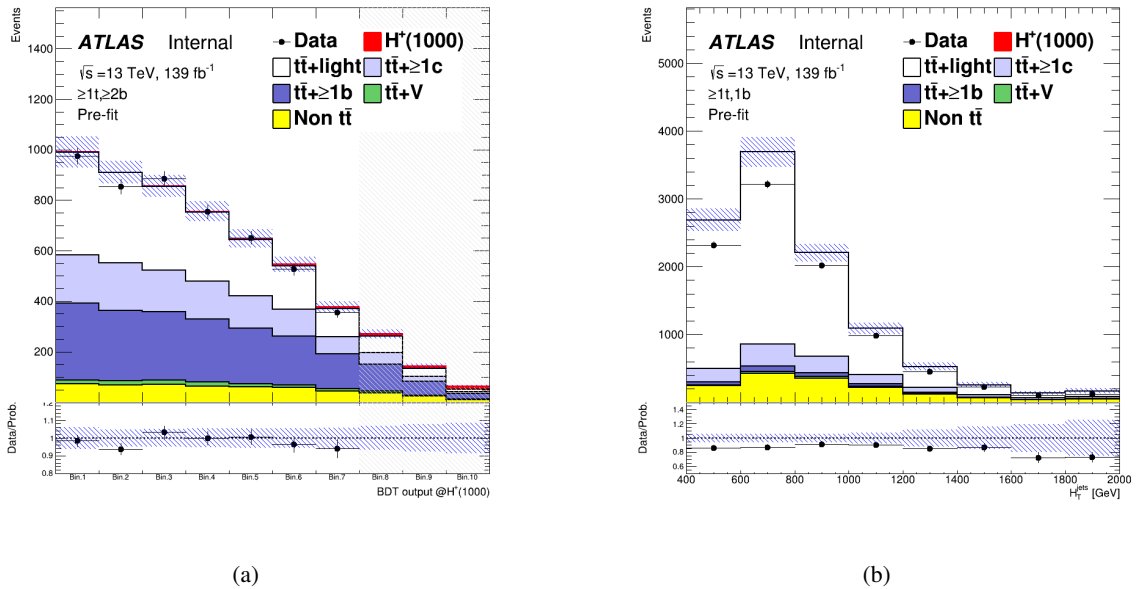


Figure 17: Pre-fit distribution of BDT output in the SR (a) and H_T^{jets} in the CR for the 1000 GeV H^+ mass hypotheses.

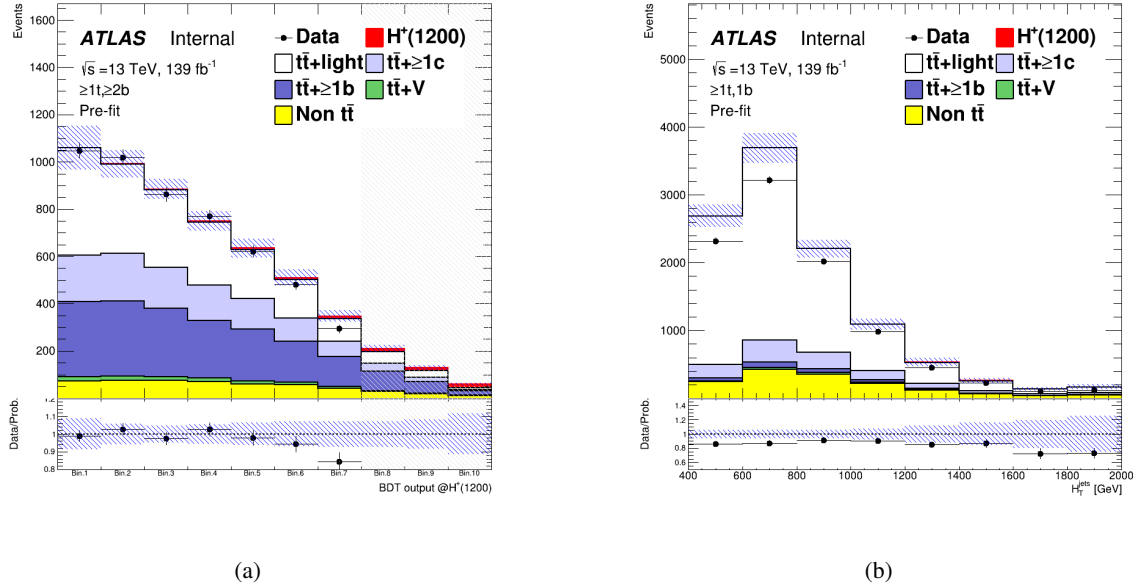


Figure 18: Pre-fit distribution of BDT output in the SR (a) and H_T^{jets} in the CR for the 1200 GeV H^+ mass hypotheses.

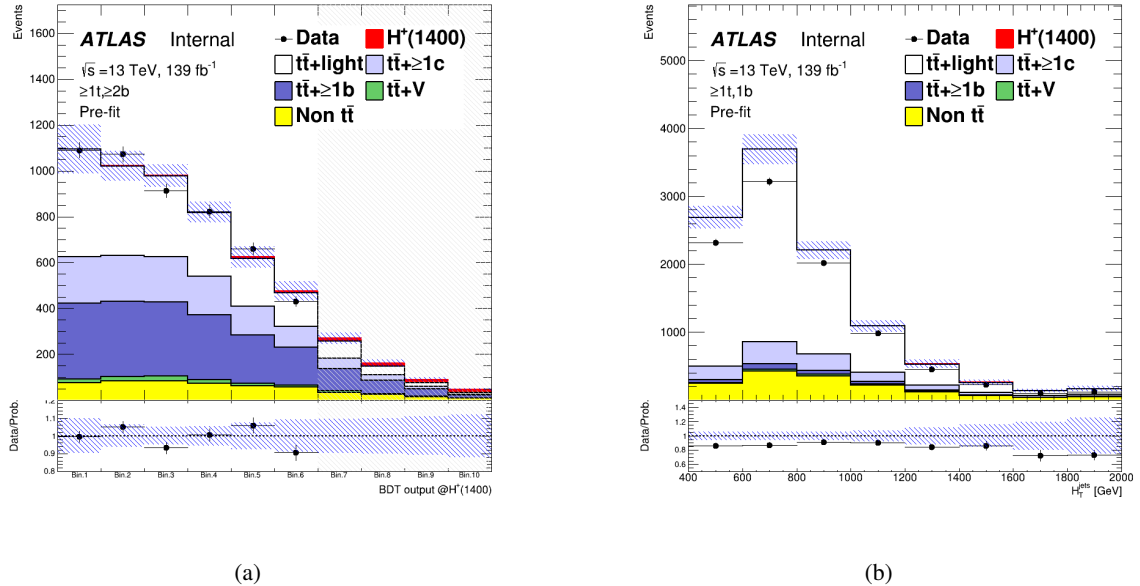


Figure 19: Pre-fit distribution of BDT output in the SR (a) and H_T^{jets} in the CR for the 1400 GeV H^+ mass hypotheses.

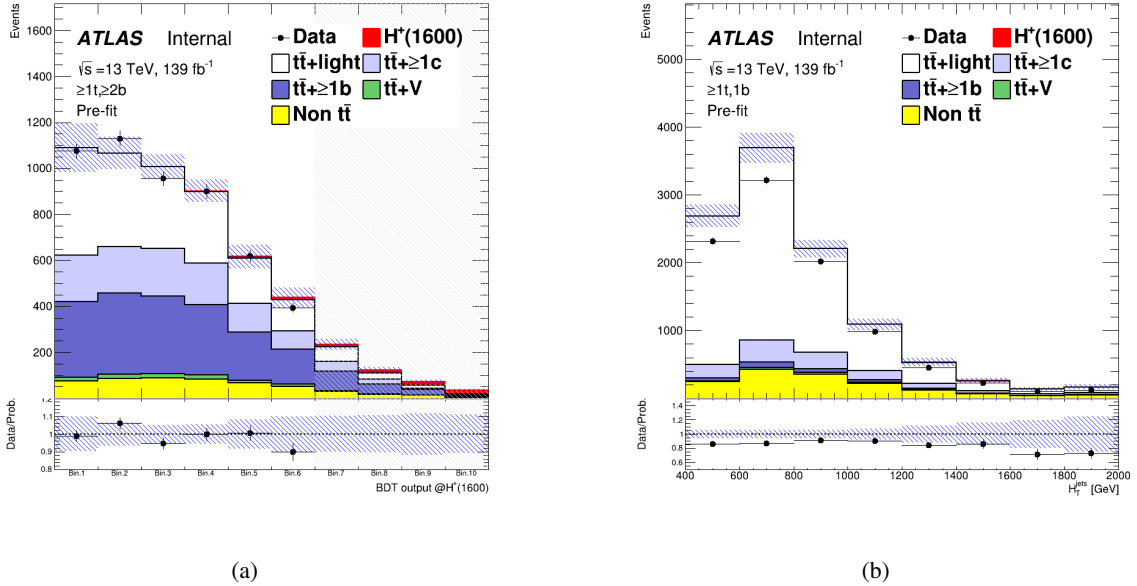


Figure 20: Pre-fit distribution of BDT output in the SR (a) and H_T^{jets} in the CR for the 1600 GeV H^+ mass hypotheses.

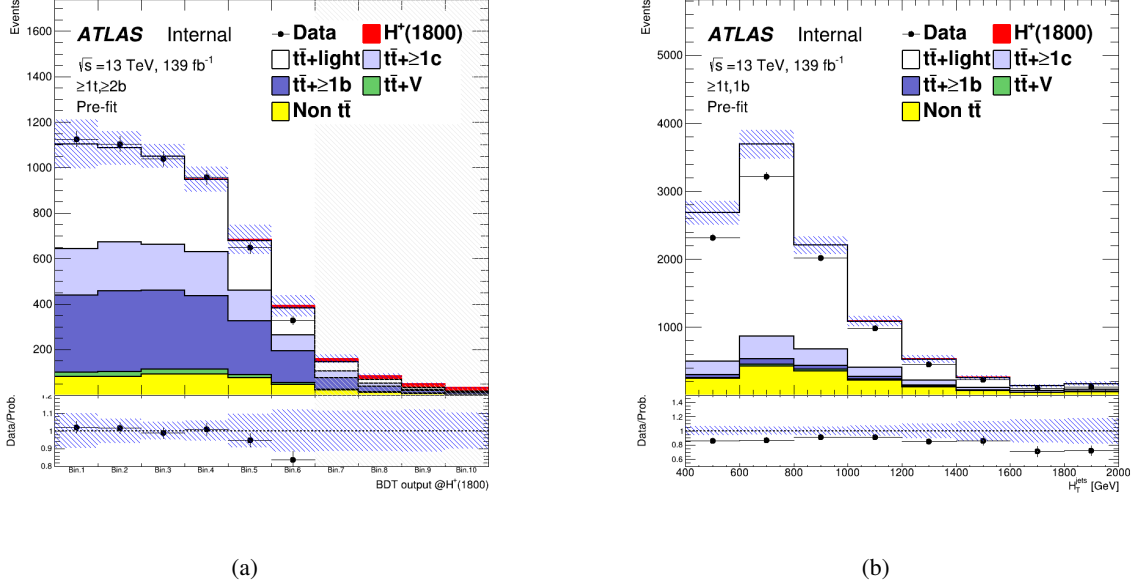


Figure 21: Pre-fit distribution of BDT output in the SR (a) and H_T^{jets} in the CR for the 1800 GeV H^+ mass hypotheses.

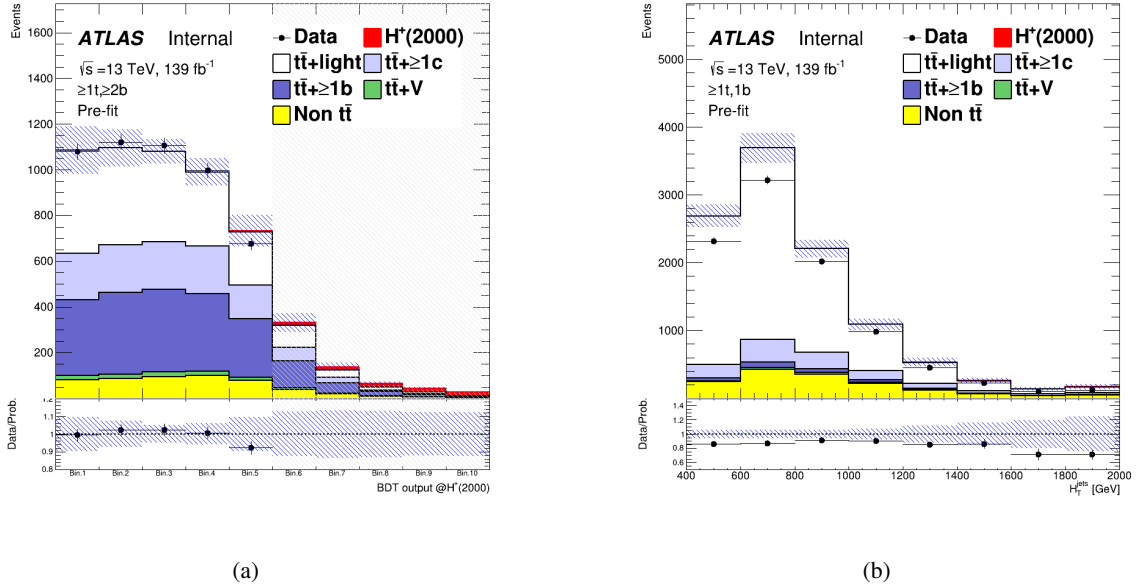


Figure 22: Pre-fit distribution of BDT output in the SR (a) and H_T^{jets} in the CR for the 2000 GeV H^+ mass hypotheses.

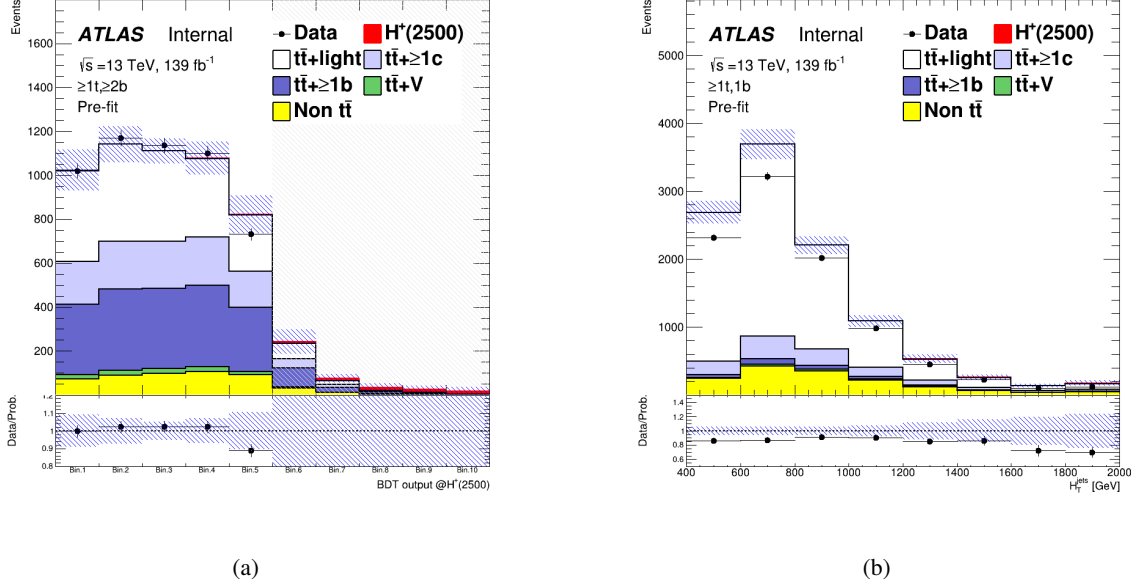


Figure 23: Pre-fit distribution of BDT output in the SR (a) and H_T^{jets} in the CR for the 2500 GeV H^+ mass hypotheses.

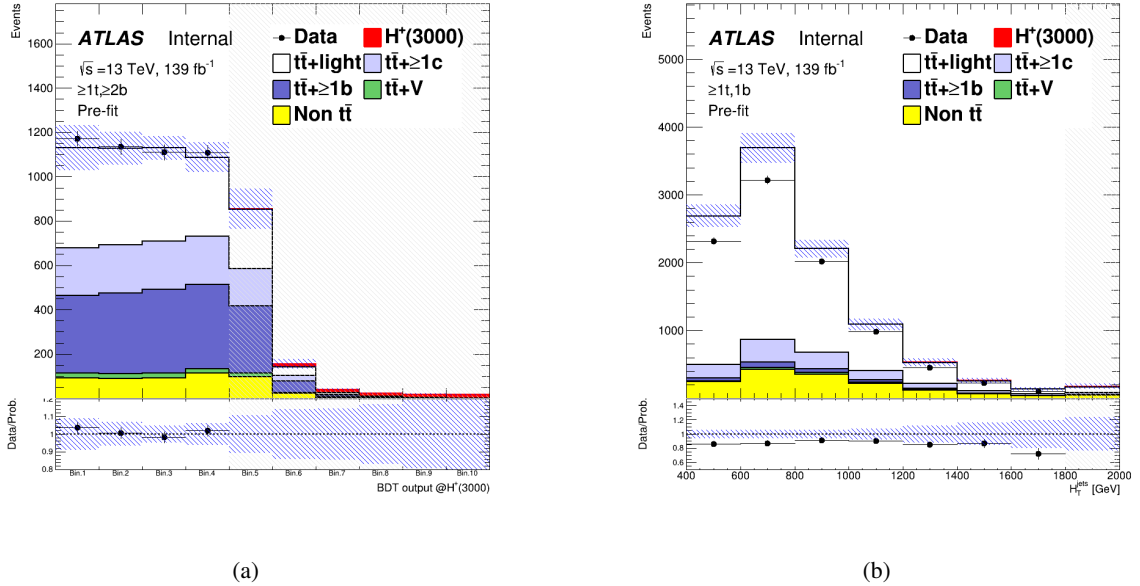


Figure 24: Pre-fit distribution of BDT output in the SR (a) and H_T^{jets} in the CR for the 3000 GeV H^+ mass hypotheses.

474 6 Systematics Uncertainties

475 The uncertainties considered in the following may affect the overall normalization of the process, the shapes
 476 of the BDT and H_T^{jets} , or both. All the experimental uncertainties considered, with the exception of that in
 477 the luminosity, affect both normalization and shape in all the simulated samples. Uncertainties related
 478 to the modeling of the signal and background affect both normalization and shape, with the exception of
 479 cross-section and $t\bar{t}$ modeling uncertainties. The former only affect the normalization of the considered
 480 sample, while the latter only affect the shape of $t\bar{t}$ samples. Nevertheless, the normalization uncertainties
 481 modify the relative fractions of the different samples, leading to a shape uncertainty in the final BDT and
 482 H_T^{jets} distributions.

483 A single independent nuisance parameter is assigned to each source of systematic uncertainty in the statistical
 484 analysis. Some of the systematic uncertainties, in particular most of the experimental ones, are decomposed
 485 into several independent sources, as specified in the following. Each individual source then has a correlated
 486 effect across all analysis regions and signal and background samples. Table 12 presents a list of all
 487 systematic uncertainties considered and indicates for each category the number of independent components
 488 and whether they affect normalisation or shape.

489 6.1 Luminosity and pile-up modeling

490 6.1.1 Luminosity

491 The uncertainty on the integrated luminosity for the full Run-2 data-set is 1.7% [30], obtained using
 492 LUCID-2 detector [92] for the primary luminosity measurement.

493 6.1.2 Pile-up modeling

494 A variation in the pile-up reweighting of the simulated events is included to cover the uncertainties in the
 495 ratio of the predicted and measured inelastic cross-sections in the fiducial volume defined by $M_X > 13$
 496 GeV, where M_X is the mass of the hadronic system [93].

497 6.2 Reconstructed objects

498 6.2.1 Charged leptons

499 Uncertainties associated with charged leptons arise from the trigger selection, the object reconstruction,
 500 identification and isolation criteria, as well as the lepton momentum scale and resolution. The reconstruction,
 501 identification and isolation efficiency of electrons and muons, as well as efficiency of the trigger used
 502 to record the events, differ slightly between data and simulation, which is compensated for by dedicated
 503 scale factors (SFs). Efficiency SFs are measured using tag-and-probe techniques on $Z \rightarrow l^+l^-$ data and
 504 simulated samples [73, 94], and are applied to the simulation to correct for the differences. The effect of
 505 these SFs as well as of their uncertainties are propagated as corrections to the MC event weight. In total,
 506 four independent components are considered for electrons and ten for muons.

Systematics uncertainty	Type	Components
Experimental uncertainties		
Luminosity	N	1
Pileup modeling	SN	1
<i>Physics objects</i>		
Electrons	SN	7
Muons	SN	15
Small-R jet energy scale	SN	31
Small-R jet energy resolution	SN	9
Small-R jet mass scale	SN	8
Large-R jet energy scale	SN	24
Large-R jet energy resolution	SN	12
Large-R jet mass scale	SN	18
Large-R jet mass resolution	SN	11
Jet vertex tagger	SN	1
<i>b</i> -tagging		
Efficiency	SN	45
Mis-tag rate (c)	SN	20
Mis-tag rate (light)	SN	20
<i>t</i> <i>t</i> -tagging		
Signal efficiency	SN	9
p_T extrapolation signal efficiency	SN	1
background efficiency	SN	5
inefficiency	SN	3
Signal and background modeling		
<i>Signal</i>		
PDF variations	SN	30
Scales	SN	2
<i>t</i> <i>t</i> background		
PDF variations	SN	90
$t\bar{t} + \geq 1c$ and $t\bar{t} + \geq 1b$ normalization	N (free floating)	1
$t\bar{t}$ + light normalization	N (free floating)	1
$t\bar{t}$ + light modeling	S	6
$t\bar{t} + \geq 1c$ modeling	S	6
$t\bar{t} + \geq 1b$ modeling	S	6
<i>Other backgrounds</i>		
$t\bar{t}W$ cross-section	N	2
$t\bar{t}Z$ cross-section	N	2
$t\bar{t}W$ modeling	SN	1
$t\bar{t}Z$ modeling	SN	1
Single top cross-section	N	3
Single top modeling	SN	6
W+jets normalization	N	3
Z+jets normalization	N	1
Diboson normalization	N	1
$t\bar{t}\bar{t}\bar{t}$ cross-section	N	3

Table 12: List of systematic uncertainties included in the analysis.

507 Additional sources of uncertainty originate from the corrections applied to adjust the lepton momentum
 508 scale and resolution in the simulation to match those in data, measured using reconstructed distributions of
 509 the $Z \rightarrow l^+l^-$ and $J/\psi \rightarrow l^+l^-$ masses, as well as the E/p ratio measured in $W \rightarrow e\nu$ events, where E and p
 510 are the electron energy and momentum measured by the calorimeter and the tracker, respectively [73, 95].
 511 To evaluate the effect of momentum scale uncertainties, the event selection is redone with the lepton energy
 512 or momentum varied by $\pm 1\sigma$. For the momentum resolution uncertainties, the event selection is redone
 513 by smearing the lepton energy or momentum. In total, three independent components are considered for
 514 electrons and five for muons.

515 6.2.2 Small- R jets, Large- R jets

516 Uncertainties associated with jets arise from the efficiency of pile-up rejection by the JVT, from the jet
 517 energy scale (JES) and resolution (JER), from the jet mass scale (JMS) and resolution (JMR), and from b -
 518 and top-tagging.

519 Jet vertex tagging:

520 Scale factors are applied to correct for discrepancies between data and MC for JVT efficiencies.
 521 These SFs are estimated using $Z \rightarrow \mu^+\mu^-$ with tag-and-probe techniques similar to those in Ref.[78],
 522 and the effect of these SFs as well as of their uncertainties are propagated as corrections to the MC
 523 event weight.

524 Small- R jet:

525 The *R4_CategoryReduction_FullJER.config* jet uncertainties configuration is used. The JES and
 526 its uncertainty for small- R jets are derived by combining information from test-beam data, LHC
 527 collision data and simulation [96]. The uncertainties from these measurements are factorized into
 528 several independent sources. Additional uncertainties are considered, related to jet flavor (using the
 529 conservative default value of $50 \pm 50\%$ for the quark/gluon fraction for all MC samples), pile-up
 530 corrections, η dependence, high- p_T jets, and differences between full and fast simulation, yielding a
 531 total of 31 independence sources.

532 The JER was measured in Run-2 data and simulation as a function of jet p_T and rapidity using dijet
 533 events, using a similar method as that in Ref. [97]. The combined uncertainty is propagated by
 534 smearing the jet p_T in MC, yielding to nine independent sources.

535 The JMS uncertainties for small- R jets are derived using the RTrk uncertainties that compares the
 536 ratio of the jet mass for calorimeter jets to the jet mass of track-based jets in data and MC simulation
 537 [98]. The six NPs are provided related with baseline, modeling, tracking and total statistics. The
 538 technique takes advantage of two independent measures of the jets mass (in the calorimeter and
 539 using the ID), however this assumption breaks in the case of particle flow jets which uses both
 540 calorimeter and tracking information. For PFlow jets, the uncertainties derived for EMTopo jets are
 541 used and two additional uncertainties are provided. These uncertainties are derived by comparing
 542 the jet mass of EMTopo and PFlow jets in data and MC. Two NPs are provided similarly to the RTrk
 543 uncertainties related with baseline and modeling. The JMS uncertainties are intentionally derived
 544 after the application of the JES and JER smearing. This is different compared to large- R jets where
 545 no nominal JER smearing is applied. The JES corrects the overall energy scale, which impacts the
 546 mass as it is applied to the full four-vector. The JMS correction and uncertainties are then a residual
 547 correction accounting for the distribution of energy within the jet. For this reason, the JES and JMS
 548 uncertainties are to first order uncorrelated effects.

549 **Large- R jet:**

550 The *R10_CategoryJES_FullJER_FullJMS.config* jet uncertainties configuration is used for JES,
 551 JER and JMS variation. JES uncertainties for large- R jets are derived using a similar approach as
 552 for small- R jets [98]. Correlation between these two objects are taken into account in uncertainty
 553 evaluation. Additional uncertainties related with a topology of an event are included.

554 The JER uncertainties for large- R jets are derived in the same way as the small- R jets uncertainties.
 555 The dijet balance asymmetry is used to evaluate the JER, which is sufficient to cover the fully
 556 supported kinematic regime for large- R jet usage. The nominal data/MC difference is found to
 557 be consistent with 1 within uncertainty. For this reason, no nominal JES smearing is applied.
 558 Instead, the nominal data/MC difference from 1 is taken as an additional uncertainty on top of the
 559 uncertainties related with limited statistics, detector effects, or modeling. The FullJER model with
 560 12 NPs is used. Both data and MC events are smeared to cover properly the correlations between jets
 561 different regions of the detector.

562 The JMS uncertainties for large- R jets are derived from the forward folding technique (FF) in the
 563 limited region of $200 \text{ GeV} < p_T < 1000 \text{ GeV}$ around the W and top mass peaks [98, 99]. The
 564 Rtrk technique is used to extend this region to $200 \text{ GeV} < p_T < 3000 \text{ GeV}$, $m < 600 \text{ GeV}$ and
 565 $|\eta| < 2.0$. The forward folding method is used to fit the W and top mass peaks in $t\bar{t}$ semileptonic
 566 events. The Rtrk method uses the double ratio of data/MC for calorimeter only quantities and
 567 track-only quantities. This technique can cover wider range in p_T , η and mass. However, forward
 568 folding technique is more precise in the lower p_T region and the mass around the top and W masses.
 569 The uncertainties from the two approaches are combined and fitted as a function p_T in a given mass
 570 bin. Interpolation between mass bins is used to provide smooth uncertainties. The full set of JMS
 571 NPs is used in the analysis in order to allow possible combinations with other measurements. The
 572 NPs are related with limited statistics of measurements, detector effects, modeling and selections. In
 573 addition, uncertainties related with interpolation between mass bins and uncertainties related with a
 574 difference between QCD and hadronic decay jet mass response are included.

575 Measurements of the JMR in the $t\bar{t}$ semileptonic events are also used to constrain the JMR uncertainties
 576 by using the forward folding method [98, 99]. Measurements are performed in two mass regions
 577 to cover W boson and top quark mass peaks. The W boson mass peak is fitted in a region of
 578 $50 \text{ GeV} < m_{\text{jet}} < 120 \text{ GeV}$ and $200 \text{ GeV} < p_{T,\text{jet}} < 350 \text{ GeV}$. The top mass peak is fitted in a region
 579 of $120 \text{ GeV} < m_{\text{jet}} < 300 \text{ GeV}$ and $350 \text{ GeV} < p_{T,\text{jet}} < 1000 \text{ GeV}$. Relative JMR uncertainty of 20%
 580 is used outside these regions. FullJMR uncertainty model with 10 nuisance parameters is used to
 581 cover uncertainties related with measurement of JMR using FF method, interpolation between bins
 582 and comparison between different MC models for events outside the two gions. This measurement is
 583 within top mass interval. However, $p_{T,\text{jet}}$ exceeds the p_T range provided by the FF method.

584 **b -tagging:**

585 b -tagging efficiencies in simulated samples are corrected to match efficiencies in data. Scale factors
 586 are derived as a function of p_T for jets containing b -jets, c -jets and for jets containing neither b -
 587 nor c -hadrons (light-jets) separately, in dedicated calibration analysis. For b -jets efficiencies, $t\bar{t}$
 588 events in the dilepton topology are used, exploiting the very pure sample of b -jets arising from the
 589 decays of the top quarks [79]. For c -jet mistag rates, $t\bar{t}$ events in signle-lepton topology are used,
 590 exploiting the c -jets from the hadronically decaying W bosons, using techniques similar as those in
 591 Ref. [100]. For light-jets mistag rates, the so-called negative-tag method similar as that in Ref. [101]
 592 is used, but using $Z + \text{jets}$ events instead of di-jet events. In the three calibration analyses, a large

number of uncertainty components are considered, and a principal component analysis is performed, yielding in 45, 20 and 20 eigenvariations, respectively, for b -, c and light-jets, which are taken as uncorrelated sources of uncertainties. The number of these eigenvariations correspond to the number of p_T bins, (9, 4 and 4, respectively, for b -, c - and light-jets) multiplied by the number of the tag weight bins ($\varepsilon \in [0\%, 60\%], [60\%, 70\%], [70\%, 77\%], [77\%, 85\%], [85\%, 100\%]$). The calibration used in this analysis is stored in following "CDI file":
`/cvmfs/atlas.cern.ch/repo/sw/database/GroupData/xAODTaggingEfficiency/13TeV/2020-21-13TeV-MC16-CDI-2021-04-16_v1.root.`

Top-tagging:

Jets are called signal if they passed contained top criteria. Otherwise, they are called background jet. Uncertainties for back ground jets are measured in two phase-spaces containing QCD multijet and gamma+jet processes. The signal jets uncertainties are measured in the boosted $t\bar{t}$ lepton+jets channel. Additional uncertainties are assigned to cover signal modeling effects and extrapolation beyond phase-spaces. These uncertainties were released as part of the consolidated large- R jet uncertainties.

6.3 Signal modeling

6.3.1 H^+ signal

The H^+ signal uncertainty is modeled in two way: by using the PDF uncertainties and through the variation of μ_f and μ_r . The uncertainties from the modeling of the PDF, which is done with the NNPDF2.3 (3.0) PDF set for datasets simulated at ≤ 3.0 (≥ 4.0) TeV, is made using a symmetrized Hessian set, PDF4LHC15_nlo_30, following the PDF4LHC recommendations for LHC Run II [103]. The signal scale uncertainty is modeled by varying μ_f and μ_r up (and down) by a factor 2 (or 0.5).

6.4 Background modeling

6.4.1 $t\bar{t}$ +jets

$t\bar{t}$ + heavy flavor classification

The $t\bar{t}$ + jets background is categorized according to the flavor of additional jets in the event, using the same procedure as described in Ref. [23]. Generator-level particle jets are reconstructed from stable particles (mean lifetime $\tau > 3 \times 10^{-11}$ seconds) using the anti- k_t algorithm with a radius parameter $R = 0.4$, and are required to have $p_T > 15$ GeV and $|\eta| < 2.5$. The flavor of a jet is determined by counting the number of b - or c -hadrons within $\Delta R < 0.4$ of the jet axis. Jets matched to exactly one b -hadron, with p_T above 5 GeV, are labeled single- b -jets, while those matched to two or more b -hadrons are labeled b -jets (with no p_T requirement on the second hadron); single- c - and c -jets are defined analogously, only considering jets not already defined as single- b - or b -jets. Events that have at least one single- b - or b -jet, not counting heavy-flavor jets from top-quark or W -boson decays, are labeled as $t\bar{t} + \geq 1b$; those with no single- b - or b -jet but at least one single- c - or c -jet are labeled as $t\bar{t} + \geq 1c$. Finally, events not containing any heavy-flavor jets aside from those from top-quark or W -boson decays are labeled as $t\bar{t}$ + light. This classification is used to define the background categories in the likelihood fit.

632 **Systematic uncertainties**

633 The systematic uncertainties affecting the $t\bar{t}$ + jets background modeling are summarized in Table 13.

634 The normalization of $t\bar{t}$ + light, $t\bar{t}+ \geq 1c$ and $t\bar{t}+ \geq 1b$ are allowed to vary freely in the fit. The
635 normalization factors of $t\bar{t}+ \geq 1c$ and $t\bar{t}+ \geq 1b$ are estimated with a common parameter in the fit,
636 because these shape are similar for each other as shown in Figure 25. Besides normalization, the
637 $t\bar{t}$ + light, $t\bar{t}+ \geq 1c$ and $t\bar{t}+ \geq 1b$ processes are affected by different types of uncertainties: $t\bar{t}$ + light
638 has additional diagrams and profits from relatively precise measurements in data; $t\bar{t}+ \geq 1c$ and
639 $t\bar{t}+ \geq 1b$ can have similar or different diagrams depending on the flavor scheme used for the PDF,
640 and different mass of the c - and b -quark contribute to additional differences between these two
641 processes. For these reasons, all uncertainties in the $t\bar{t}$ + jets background modeling are assigned
642 independent nuisance parameters for the $t\bar{t}$ + light, $t\bar{t}+ \geq 1c$ and $t\bar{t}+ \geq 1b$ processes.

643 Systematic uncertainties on the acceptance and shapes are extracted from the comparison between
644 the nominal and different MC samples and settings. For ISR and FSR the settings of the nominal
645 Powheg+Pythia sample are varied, resulting in different event weight; the uncertainty due to ISR is
646 estimated by changing μ_r and μ_f in the ME and α_S^{ISR} in the PS, while the uncertainty due to FSR is
647 estimated by changing α_S^{FSR} in the PS. For the ISR, the amount of radiation is increased (decreased)
648 by scaling μ_r and μ_f by a factor 0.5 (2.0) and by using the Var3cUp (Var3cDown) variation from the
649 A14 tune [38], corresponding to $\alpha_S^{\text{ISR}} = 0.140(0.115)$ instead of the nominal $\alpha_S^{\text{ISR}} = 0.127$. For the
650 FSR, the amount of radiation is increased (decreased) varying μ_r for QCD emission in the FSR by a
651 factor of 0.5 (2.0), corresponding to $\alpha_S^{\text{FSR}} = 0.1423(0.1147)$ instead of the nominal $\alpha_S^{\text{FSR}} = 0.127$.
652 The nominal Powheg+Pythia sample is compared to the Powheg+Herwig sample to access the effect
653 of the PS and hadronisation models, and to the MG5_aMC sample to access the effect of the NLO
654 matching technique.

Uncertainty source	Description	Components
$t\bar{t}$ + light normalization	Free-floating	$t\bar{t}$ + light
$t\bar{t}+ \geq 1c/b$ normalization	Free-floating	$t\bar{t}+ \geq 1c$ and $t\bar{t}+ \geq 1b$
NLO matching	MG5_aMC+Pythia	vs. Powheg+Pythia
PS & hadronisation	Powheg+Herwig	vs. Powheg+Pythia
α_S^{ISR}	<i>Var3cUp (Var3cDown)</i>	in Powheg+Pythia
μ_f	scaling by 0.5 (2.0)	in Powheg+Pythia
μ_r	scaling by 0.5 (2.0)	in Powheg+Pythia
FSR	Varying α_S^{FSR} (PS)	in Powheg+Pythia
		All

Table 13: Summary of the sources of systematic uncertainty for $t\bar{t}$ + jets modeling. The systematic uncertainties listed in the second section of the table are evaluated in such a way to have no impact on the normalization of the three, $t\bar{t}$ + light, $t\bar{t}+ \geq 1c$ and $t\bar{t}+ \geq 1b$ components in the phase-space selected in the analysis. The last column of the table indicates the $t\bar{t}$ + jets components to which a systematic uncertainty is assigned. All systematic uncertainty sources are treated as uncorrelated across the three components.

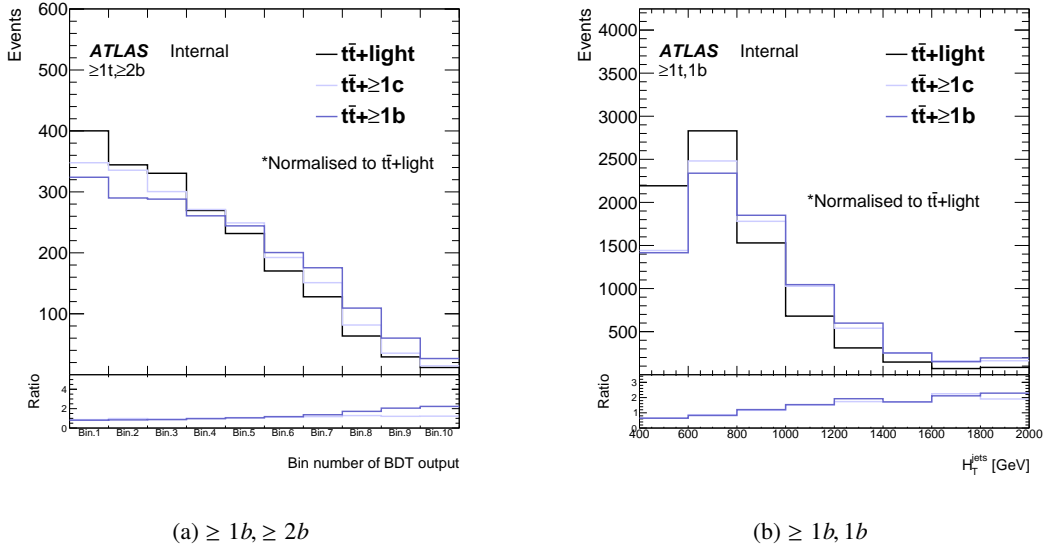


Figure 25: BDT output distribution in SR for the 1000 GeV H^+ mass hypothesis (left) and H_T^{jets} distribution in CR (right). Distributinos of $t\bar{t} + \geq 1b$ and $t\bar{t} + \geq 1b$ are normalised to $t\bar{t} + \text{light}$. And the ratio to $t\bar{t} + \text{light}$ are computed for $t\bar{t} + \geq 1b$ and $t\bar{t} + \geq 1b$.

655 6.4.2 Other backgrounds

656 The predicted $t\bar{t}H$ signal cross-section uncertainty is $^{+5.8\%}_{-9.2\%}$ (QCD scale) $\pm 3.6\%$ (QCD + α_S) [104–109].
 657 These two components are treated as uncorrelated in the fit. The effect of QCD scale and PDF variations
 658 on the shape of the distributions is found to be negligible. Uncertainties in the Higgs-boson branching
 659 fractions are also considered; these amount to 2.2% for the $b\bar{b}$ decay mode [104]. Uncertainties associated
 660 to the modeling of $t\bar{t}H$ by the Powheg+Phythia sample are also considered, for a total of four independent
 661 components. The uncertainty due to ISR is estimated by simultaneously changing μ_f and μ_r in the ME and
 662 α_S^{ISR} in the PS, while the uncertainty due to ISR is estimated by changing α_S^{FSR} in the PS. For the ISR and
 663 FSR, the amount of radiation is varied following the same procedure as for $t\bar{t}$. The nominal Powheg+Pythia
 664 sample is compared to the Powheg+Herwig sample to access the uncertainty due to PS and hadronization,
 665 and to the MG5_aMC+Phythia sample for the uncertainty due to the NLO matching.

666 A $\pm 5\%$ uncertainty is considered for the cross-sections of the three single-top production modes [110–114].
 667 Uncertainties associated with the PS and hadronisation model, and with the NLO matching scheme are
 668 evaluated by comparing, for each process, the nominal Powheg+Pythia sample to a sample produced using
 669 Powheg+Herwig and MG5_aMC+Pythia, respectively. The uncertainty associated to the interference
 670 between Wt and $t\bar{t}$ production at NLO [58] is assessed by comparing the nominal Powheg+Pythia sample
 671 produced using the "diagram removal" scheme to an alternative sample produced with the same generator
 672 but using the "diagram subtraction" scheme.

673 The uncertainty of the $t\bar{t}V$ NLO cross-section prediction is 15% [115, 116], split into PDF and scale
 674 uncertainties as for $t\bar{t}H$. An additional $t\bar{t}V$ modeling uncertainty, related to the choice of PS and
 675 hadronisation model and NLO matching scheme is assessed by comparing the nominal MG5_aMC+Pythia
 676 samples with alternative ones generated with Sherpa.

677 A total 50% normalization uncertainty is considered for the 4 tops background, covering effects from
678 varying μ_f and μ_r , PDFs and α_S [34, 117]. The small backgrounds from tZq and tWH are each assigned
679 cross-section uncertainties: $\pm 7.9\%$ and $\pm 0.9\%$ for tZq , accounting for μ_f and μ_r variations, and for PDFs,
680 respectively, and $\pm 50\%$ for tWZ [34].

681 An uncertainty of 40% is assumed for the $W +$ jets cross-section, with an additional 30% normalization
682 uncertainty used for $W +$ heavy-flavor jets, taken as uncorrelated between events with two and more than
683 two heavy-flavor jets. These uncertainties are based on variations of the μ_f and μ_r and of the matching
684 parameters in the Sherpa samples. An uncertainty of 35% is then applied to the $Z +$ jets normalization,
685 uncorrelated across jet bins, to account for both the variations of the scales and matching parameters in the
686 Sherpa samples and the uncertainty in the extraction from data of the correction factor for the heavy-flavor
687 component. Finally, a total 50% normalization uncertainty in the diboson background is assumed, which
688 includes uncertainties in the inclusive cross-section and additional jet production [118].

689 7 Profile Likelihood Fit (Without reweighting)

690 7.1 Method

691 In order to test for the presence of an $H^+ \rightarrow tb$ ($W' \rightarrow tb$) signal, a binned maximum-likelihood fit to the data
 692 is performed simultaneously in all analysis regions, and each mass hypothesis is tested separately. The input
 693 to the fit is the BDT distribution for the SR and H_T^{jets} distribution for the CR. Two initially unconstrained fit
 694 parameters are used to model the normalization of the $t\bar{t}$ + light and $t\bar{t} + \geq 1$ HF jets background. The
 695 procedures used to quantify the level of agreement with the background-only or background-plus-signal
 696 hypothesis, and to determine exclusion limits, are based on the profile likelihood ratio test and the CL_s
 697 method. The parameter of interest is the signal strength, μ .

698 To estimate the signal strength, a likelihood function, $\mathcal{L}(\mu, \theta)$, is constructed as the product of Poisson
 699 probability terms. One Poisson term is included for every bin of the BDT and H_T^{jets} distribution in the
 700 analysis regions. Binning of BDT output distribution is defined by an automatic binning algorithm,
 701 *TransfoD*, implemented in TRexFitter [119]. The expected number of events in the Poisson terms is a
 702 function of μ , and a set of nuisance parameters, θ . The nuisance parameters encode effects from the
 703 normalization of backgrounds, including two free normalization factors for the $t\bar{t}$ + light and $t\bar{t} + \geq 1$ HF
 704 jets backgrounds, the systematic uncertainties and one parameter per bin to model statistical uncertainties
 705 in the simulated samples. All nuisance parameters are constrained with Gaussian or log-normal terms.
 706 There are about 400 nuisance parameters considered in the fit, the number varying slightly across the range
 707 of mass hypotheses.

708 To extract the exclusion limit on μ , the following test statistic is used:

$$\tilde{t}_\mu = \begin{cases} -2 \ln \frac{\mathcal{L}(\mu, \hat{\theta}(\mu))}{\mathcal{L}(0, \hat{\theta}(0))} & \mu < 0 \\ -2 \ln \frac{\mathcal{L}(\mu, \hat{\theta}(\mu))}{\mathcal{L}(\hat{\mu}, \hat{\theta})} & \mu \geq 0 \end{cases} \quad (1)$$

709 The values of the signal strength and nuisance parameters that maximize the likelihood function are
 710 represented by $\hat{\mu}$ and $\hat{\theta}$, respectively. For a given value of μ , the values of the nuisance parameters that
 711 maximize the likelihood function are represented by $\hat{\theta}(\mu)$.

712 7.2 Pruning and smoothing of systematic uncertainties

713 In the fits, pruning is applied at the threshold of 1%, meaning that if the effect of a nuisance parameter is
 714 smaller than 1% before fitting (separately for shape and normalisation) it is excluded from the fit. This
 715 pruning procedure reduces the CPU time and helps the fit to converge. Appendix C shows the systematic
 716 uncertainties that are pruned in Asimov fits.

717 Smoothing is applied for systematics uncertainties on $t\bar{t}$ modeling by *MaxVariation* algorithm implemented
 718 in TRexFitter, because these uncertainties are typically computed by comparing two different MC samples,
 719 or by applying MC generator weights on a MC sample, which dilutes the MC statistics and increases the
 720 fluctuations. No smoothing is applied for modeling systematic uncertainties on small backgrounds — given
 721 their small impact on the final result — or for experimental systematics — which are obtained either by

722 applying SFs typically close to unity (e.g. b -tagging), or by using the same simulated events but with
723 different calibrations of the objects (e.g. JES).

724 **7.3 Asimov fit results**

725 In the following, the results of fits to Asimov datasets generated from simulated samples are presented.
726 Figures 26 to 41 show the nuisance parameters, normalization factors, correlation matrices, the effect of
727 the different nuisance parameters before and after the fit and post-fit plots from the fits under each H^+ mass
728 hypotheses.

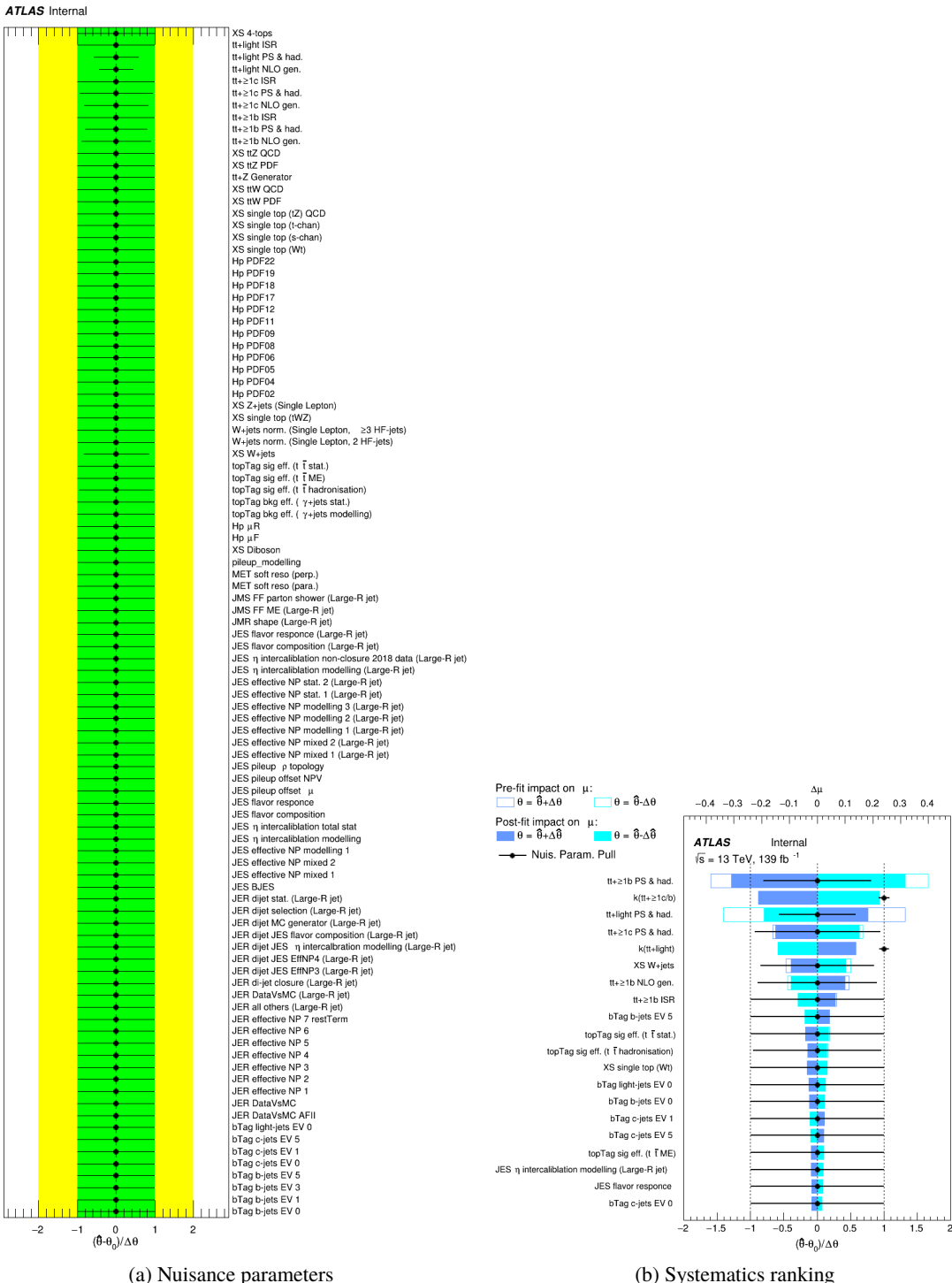
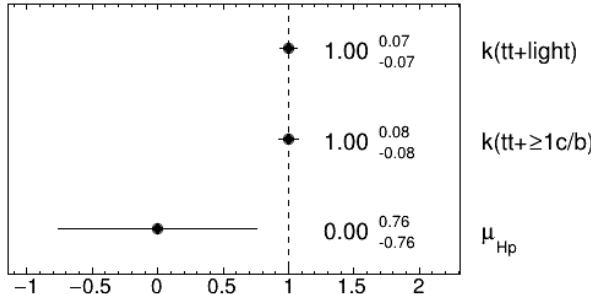
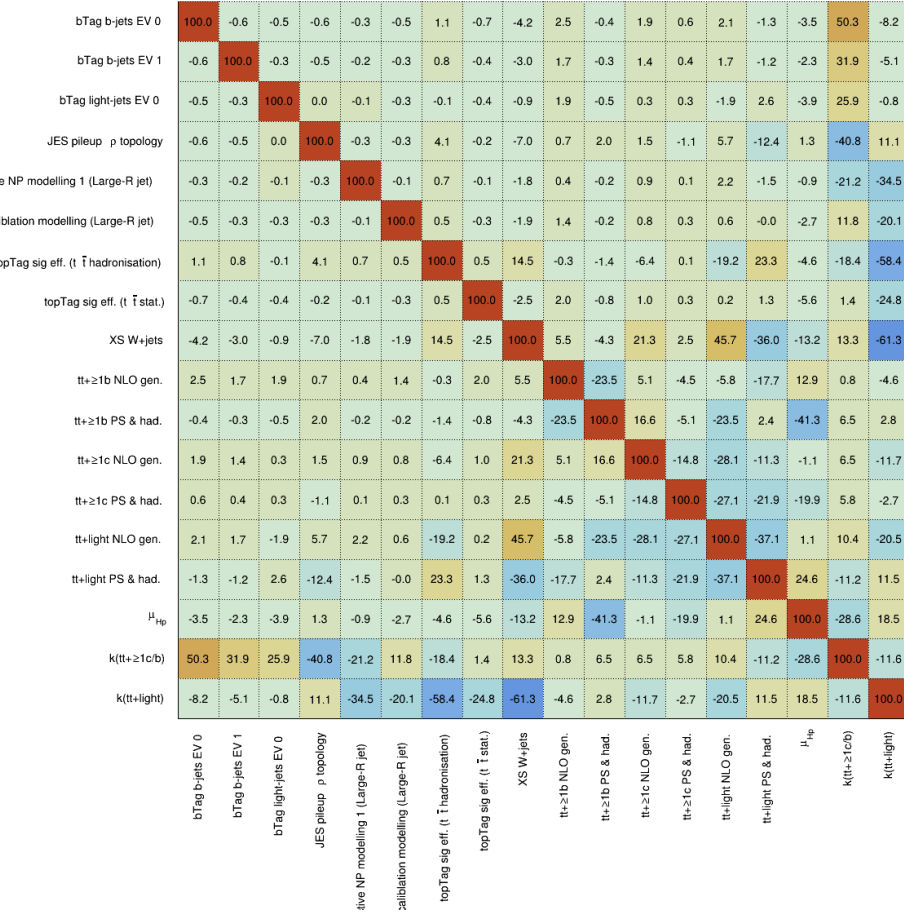


Figure 26: Nuisance parameters (left) and ranking plot (right) of the effect of various nuisance parameters before and after the fit for the 1000 GeV H^+ mass hypotheses.

ATLAS Internal

(a) Norm. factors

ATLAS Internal

(b) Correlation matrix

Figure 27: Signal strength and normalization factors (top) and correlation matrix (bottom) for the 1000 GeV H^+ mass hypotheses.

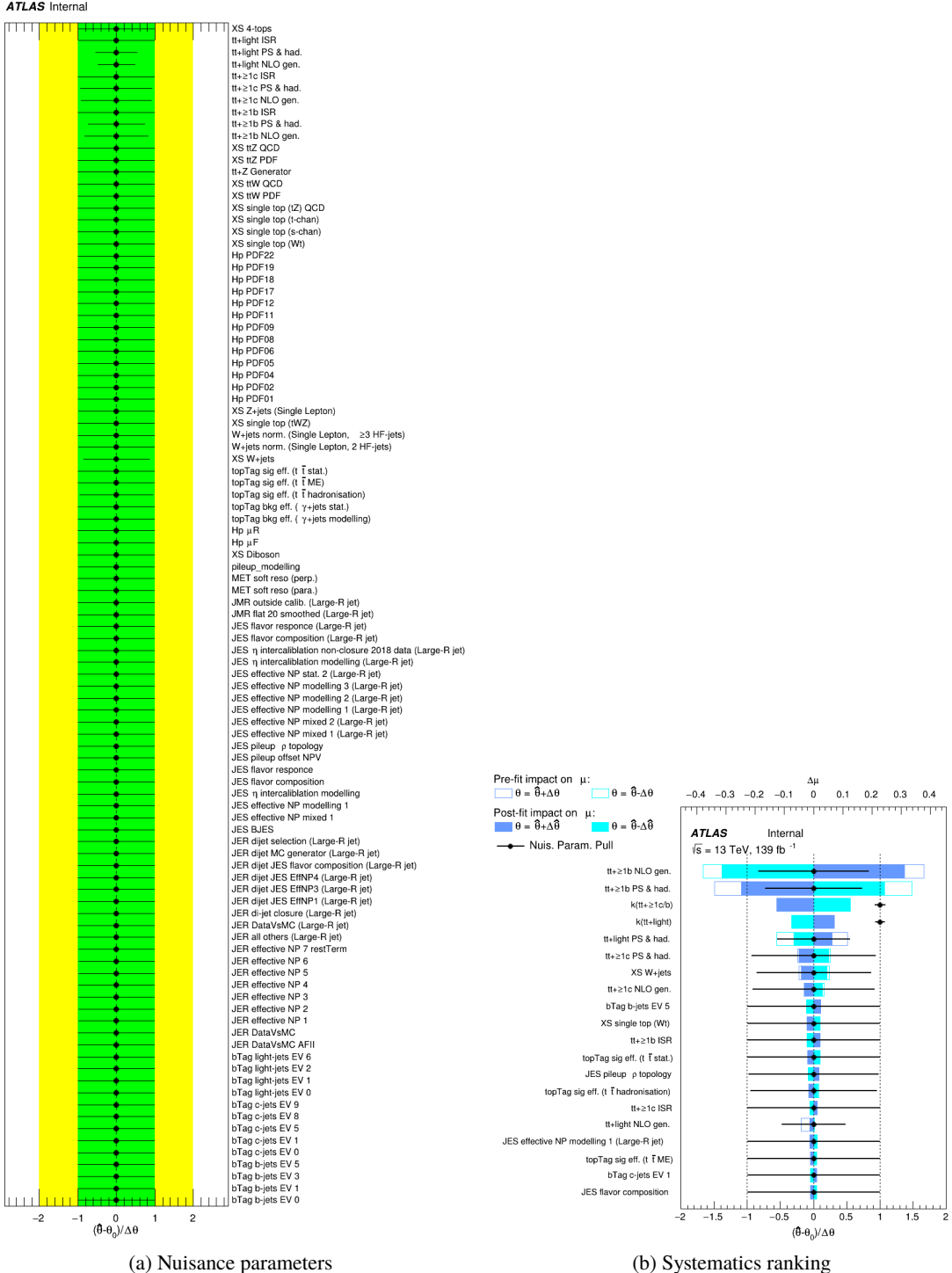
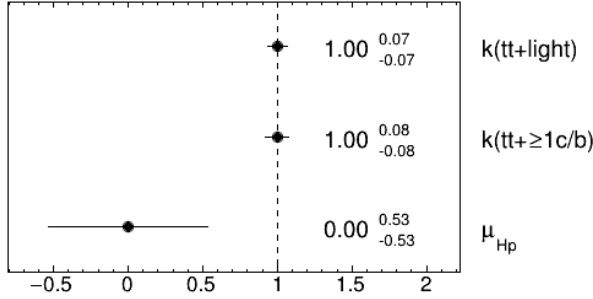


Figure 28: Nuisance parameters (left) and ranking plot (right) of the effect of various nuisance parameters before and after the fit for the 1200 GeV H^+ mass hypotheses.

ATLAS Internal

(a) Norm. factors

ATLAS Internal

	bTag b-jets EV 0	-0.4	0.0	-0.5	-0.3	-0.3	0.1	1.6	-0.4	-3.5	2.5	1.7	1.0	0.5	2.6	-2.6	-2.0	50.6	-9.0
bTag b-jets EV 1	-0.4	100.0	0.0	-0.4	-0.2	-0.2	0.0	1.1	-0.2	-2.5	1.6	1.0	0.7	0.4	2.2	-2.2	-1.1	32.1	-5.6
bTag light-jets EV 0	0.0	0.0	100.0	0.0	0.0	0.0	0.0	-0.1	0.0	0.5	0.3	1.6	0.6	0.0	-0.6	-1.2	1.6	25.7	-2.0
JES pileup p topology	-0.5	-0.4	0.0	100.0	-0.3	-0.2	-0.2	4.4	-0.1	-6.8	-0.3	0.6	1.6	-0.1	4.9	-12.3	3.3	-41.2	10.7
active NP modelling 1 (Large-R jet)	-0.3	-0.2	0.0	-0.3	100.0	-0.1	0.0	0.9	-0.1	-1.8	0.8	0.3	0.3	0.2	2.1	-1.2	-2.2	-21.0	-34.3
calibration modelling (Large-R jet)	-0.3	-0.2	0.0	-0.2	-0.1	100.0	0.0	0.8	-0.2	-1.5	1.4	1.0	0.4	0.2	0.9	-0.8	-1.9	11.9	-20.4
topTag bkg eff. (γ+jets modelling)	0.1	0.0	0.0	-0.2	0.0	0.0	100.0	0.2	0.1	-0.3	-0.3	-0.0	-0.4	-0.3	-1.8	-2.2	1.8	-20.1	-1.4
topTag sig eff. (t̄hadronisation)	1.6	1.1	-0.1	4.4	0.9	0.8	0.2	100.0	0.9	14.1	-8.0	-10.0	-4.9	-1.5	-15.5	16.4	-3.1	-18.5	-57.7
topTag sig eff. (t̄stat.)	-0.4	-0.2	0.0	-0.1	-0.1	-0.2	0.1	0.9	100.0	-1.7	2.0	1.3	0.3	0.2	0.9	-0.0	-4.1	1.4	-25.4
XS W+jets	-3.5	-2.5	0.5	-6.8	-1.8	-1.5	-0.3	14.1	-1.7	100.0	3.1	-2.9	7.5	2.7	51.1	-38.0	-8.5	13.9	-62.2
tt+≥1b NLO gen.	2.5	1.6	0.3	-0.3	0.8	1.4	-0.3	-8.0	2.0	3.1	100.0	-53.6	-8.7	-4.0	4.9	-24.3	59.0	-7.0	1.8
tt+≥1b PS & had.	1.7	1.0	1.6	0.6	0.3	1.0	-0.0	-10.0	1.3	-2.9	-53.6	100.0	-17.0	-0.4	2.4	-10.7	-46.3	12.6	4.0
tt+≥1c NLO gen.	1.0	0.7	0.6	1.6	0.3	0.4	-0.4	-4.9	0.3	7.5	-8.7	-17.0	100.0	-9.0	-41.8	-11.2	-5.9	4.1	-3.0
tt+≥1c PS & had.	0.5	0.4	0.0	-0.1	0.2	0.2	-0.3	-1.5	0.2	2.7	-4.0	-0.4	-9.0	100.0	-27.0	-28.9	-9.8	3.2	-1.6
tt+light NLO gen.	2.6	2.2	-0.6	4.9	2.1	0.9	-1.8	-15.5	0.9	51.1	4.9	2.4	-41.8	-27.0	100.0	-29.0	-1.7	12.7	-26.8
tt+light PS & had.	-2.6	-2.2	-1.2	-12.3	-1.2	-0.8	-2.2	16.4	-0.0	-38.0	-24.3	-10.7	-11.2	-28.9	-29.0	100.0	12.5	-10.5	17.1
μ_{H_p}	-2.0	-1.1	1.6	3.3	-2.2	-1.9	1.8	-3.1	-4.1	-8.5	59.0	-46.3	-5.9	-9.8	-1.7	12.5	100.0	-23.8	14.0
$k(t t+ \geq 1 c/b)$	50.6	32.1	25.7	-41.2	-21.0	11.9	-20.1	-18.5	1.4	13.9	-7.0	12.6	4.1	3.2	12.7	-10.5	-23.8	100.0	-12.0
$k(t t+ light)$	-9.0	-5.6	-2.0	10.7	-34.3	-20.4	-1.4	-57.7	-25.4	-62.2	1.8	4.0	-3.0	-1.6	-26.8	17.1	14.0	-12.0	100.0

(b) Correlation matrix

Figure 29: Signal strength and normalization factors (top) and correlation matrix (bottom) for the 1200 GeV H^+ mass hypotheses.

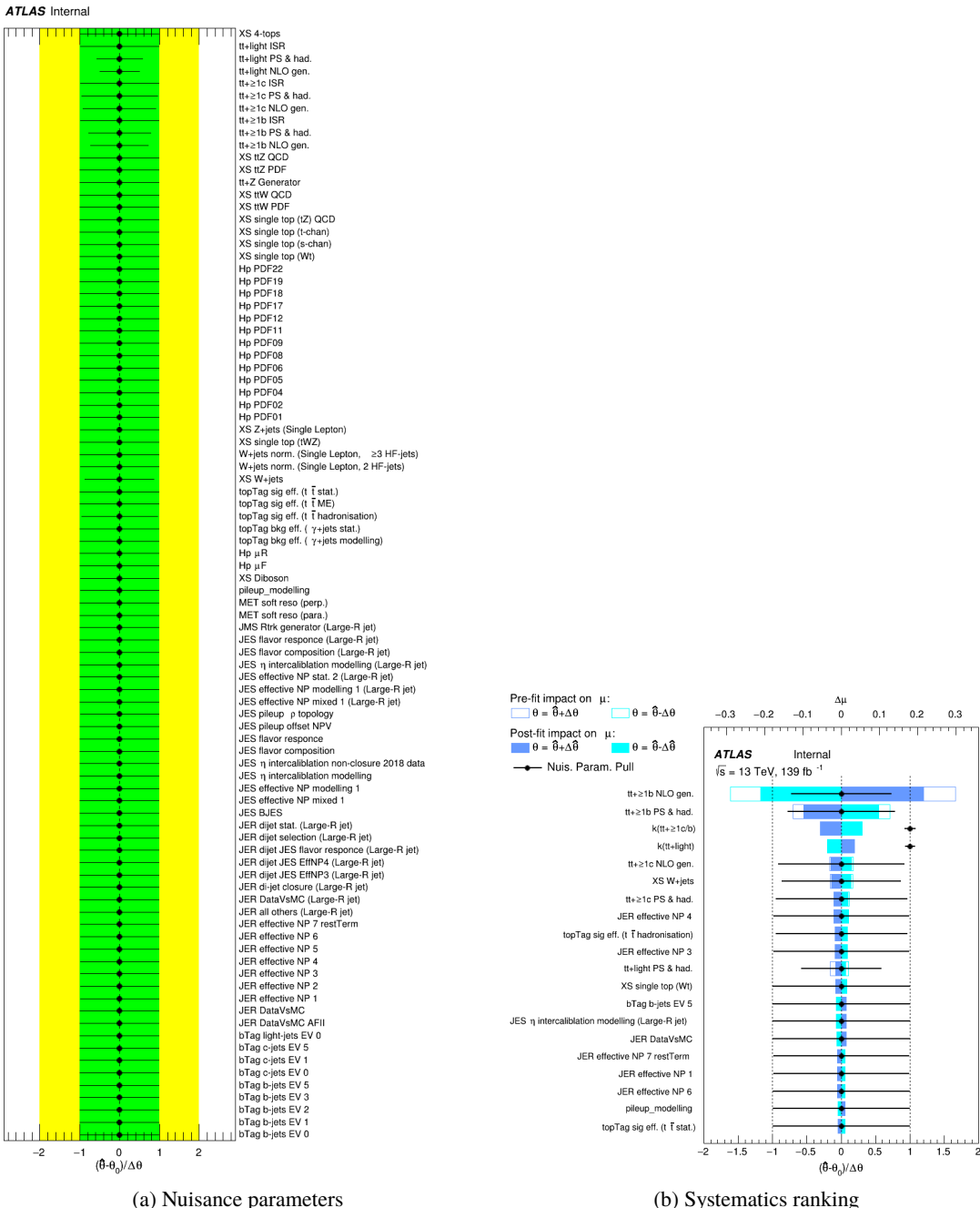
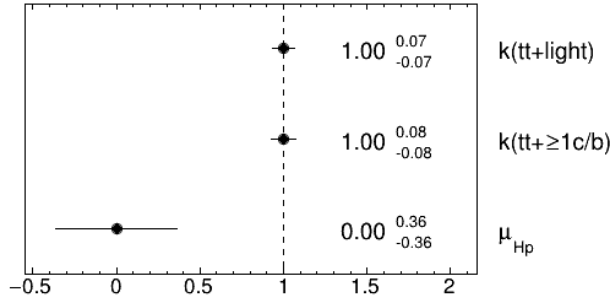
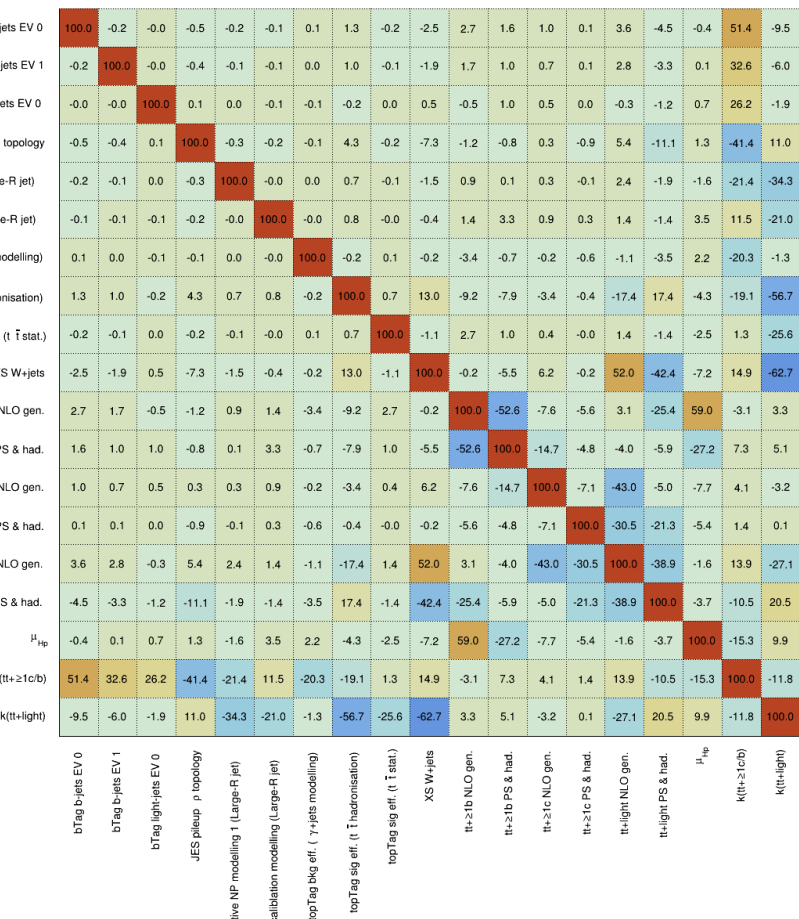


Figure 30: Nuisance parameters (left) and ranking plot (right) of the effect of various nuisance parameters before and after the fit for the 1400 GeV H^+ mass hypotheses.

ATLAS Internal**ATLAS Internal**

(b) Correlation matrix

Figure 31: Signal strength and normalization factors (top) and correlation matrix (bottom) for the 1400 GeV H^+ mass hypotheses.

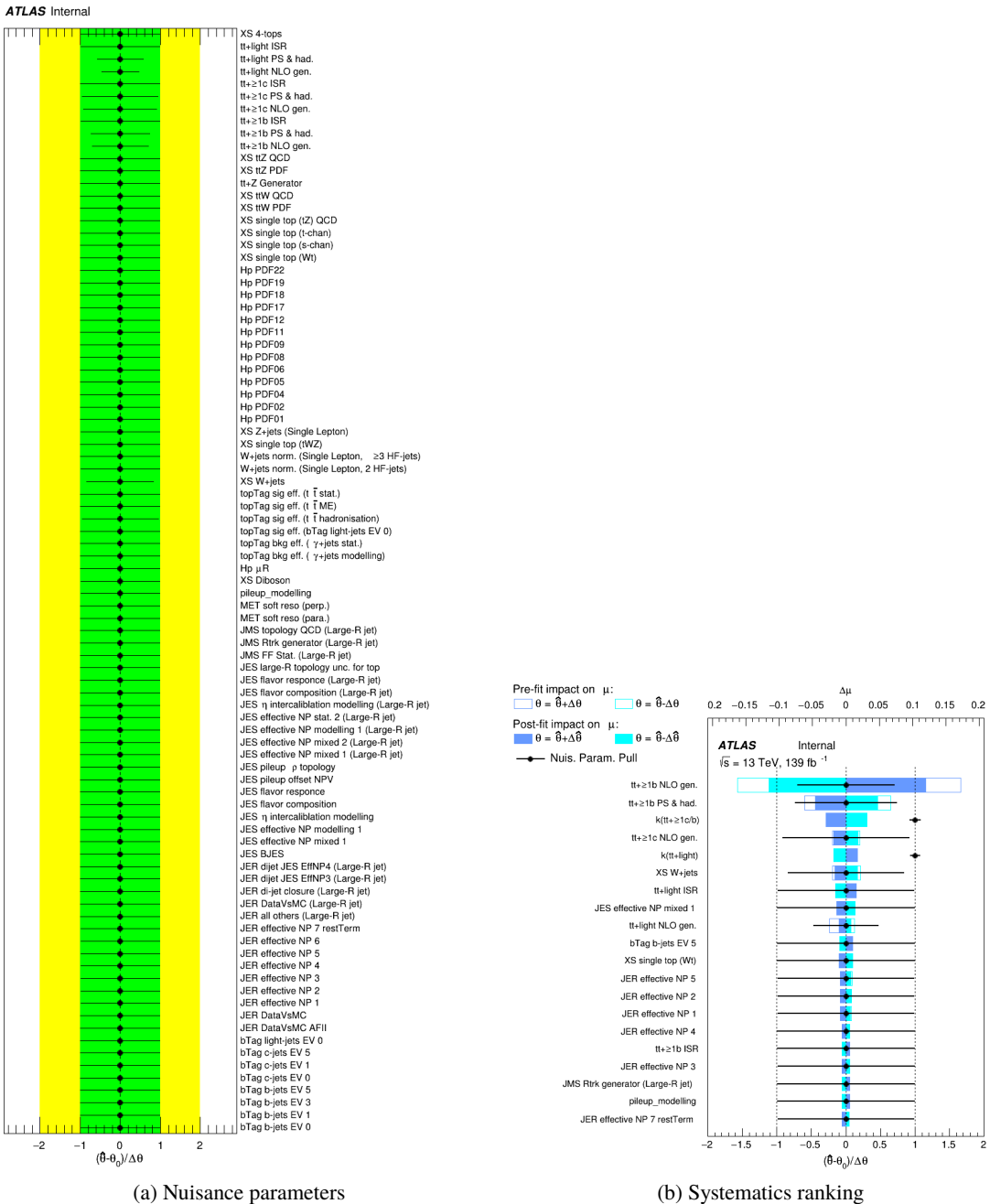
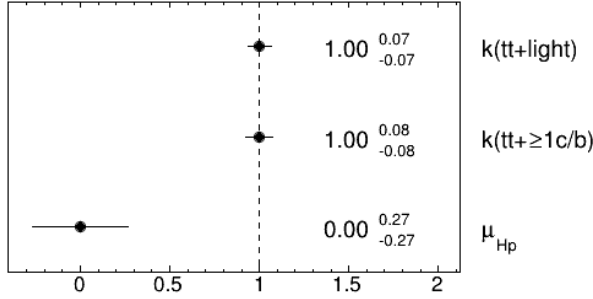


Figure 32: Nuisance parameters (left) and ranking plot (right) of the effect of various nuisance parameters before and after the fit for the 1600 GeV H^+ mass hypotheses.

ATLAS Internal

(a) Norm. factors

ATLAS Internal

	bTag b-jets EV 0	-0.2	0.0	-0.5	-0.1	-0.2	0.1	1.3	-0.2	-2.9	2.2	1.1	0.8	0.4	3.7	-4.5	0.3	51.6	-9.4
bTag b-jets EV 1	-0.2	100.0	0.0	-0.4	-0.1	-0.1	0.0	1.0	-0.1	-2.1	1.3	0.6	0.6	0.3	2.8	-3.3	0.5	32.8	-5.9
bTag light-jets EV 0	0.0	0.0	100.0	0.1	-0.0	-0.0	-0.0	-0.2	0.0	0.5	-0.8	0.4	0.0	-0.1	0.1	-0.9	1.9	26.4	-1.9
JES pileup p topology	-0.5	-0.4	0.1	100.0	-0.3	-0.2	-0.2	4.6	-0.1	-8.3	-2.0	-2.3	1.9	-0.7	4.1	-10.9	0.9	41.8	11.4
active NP modelling 1 (Large-R jet)	-0.1	-0.1	-0.0	-0.3	100.0	-0.0	-0.1	0.5	0.0	-1.5	-1.8	-1.0	0.2	-0.3	3.2	-2.8	0.1	-21.6	-34.5
calibration modelling (Large-R jet)	-0.2	-0.1	-0.0	-0.2	-0.0	100.0	0.0	0.6	-0.1	-1.1	1.5	0.9	0.4	0.2	1.5	-1.9	-0.5	12.0	-20.8
topTag bkg eff. ($\gamma + \text{jets}$ modelling)	0.1	0.0	-0.0	-0.2	-0.1	0.0	100.0	-0.2	0.1	0.1	-3.3	-0.7	-0.3	-1.0	-0.7	-3.3	1.4	-20.3	-1.4
topTag sig eff. ($t\bar{t}$ hadronisation)	1.3	1.0	-0.2	4.6	0.5	0.6	-0.2	100.0	0.6	16.1	-9.7	-3.4	-5.2	-1.7	-14.5	16.1	-0.3	-19.5	-58.5
topTag sig eff. ($t\bar{t}$ stat.)	-0.2	-0.1	0.0	-0.1	0.0	-0.1	0.1	0.6	100.0	-1.1	2.2	1.3	0.3	0.1	1.7	-1.8	-2.0	1.2	-25.8
XS W+jets	-2.9	-2.1	0.5	-8.3	-1.5	-1.1	0.1	16.1	-1.1	100.0	4.7	-16.5	6.7	4.1	47.5	-36.3	-6.6	13.5	-62.1
$t\bar{t}+\geq 1\text{b}$ NLO gen.	2.2	1.3	-0.8	-2.0	-1.8	1.5	-3.3	-9.7	2.2	4.7	100.0	-54.8	-8.5	-12.5	11.6	-27.9	44.2	1.6	1.3
$t\bar{t}+\geq 1\text{b}$ PS & had.	1.1	0.6	0.4	-2.3	-1.0	0.9	-0.7	-3.4	1.3	-16.5	-54.8	100.0	-14.6	0.6	-18.9	5.4	-17.7	2.7	10.8
$t\bar{t}+\geq 1\text{c}$ NLO gen.	0.8	0.6	0.0	1.9	0.2	0.4	-0.3	-5.2	0.3	6.7	-8.5	-14.6	100.0	-7.6	-44.8	-15.0	-6.9	3.1	-2.1
$t\bar{t}+\geq 1\text{c}$ PS & had.	0.4	0.3	-0.1	-0.7	-0.3	0.2	-1.0	-1.7	0.1	4.1	-12.5	0.6	-7.6	100.0	-27.2	-26.6	-0.5	1.9	-1.9
$t\bar{t}+\text{light}$ NLO gen.	3.7	2.8	0.1	4.1	3.2	1.5	-0.7	-14.5	1.7	47.5	11.6	-18.9	-44.8	-27.2	100.0	-25.8	-3.6	13.3	-25.4
$t\bar{t}+\text{light}$ PS & had.	-4.5	-3.3	-0.9	-10.9	-2.8	-1.9	-3.3	16.1	-1.8	-36.3	-27.9	5.4	-15.0	-26.6	-25.8	100.0	1.8	-9.7	17.4
μ_{H_p}	0.3	0.5	1.9	0.9	0.1	-0.5	1.4	-0.3	-2.0	-6.6	44.2	-17.7	-6.9	-0.5	-3.6	1.8	100.0	-11.6	6.8
$k(t\bar{t}+\geq 1\text{c}/b)$	51.6	32.8	26.4	-41.8	-21.6	12.0	-20.3	-19.5	1.2	13.5	1.6	2.7	3.1	1.9	13.3	-9.7	-11.6	100.0	-10.4
$k(t\bar{t}+\text{light})$	-9.4	-5.9	-1.9	11.4	-34.5	-20.8	-1.4	-68.5	-25.8	-62.1	1.3	10.8	-2.1	-1.9	-25.4	17.4	6.8	-10.4	100.0

(b) Correlation matrix

Figure 33: Signal strength and normalization factors (top) and correlation matrix (bottom) for the 1600 GeV H^+ mass hypotheses.

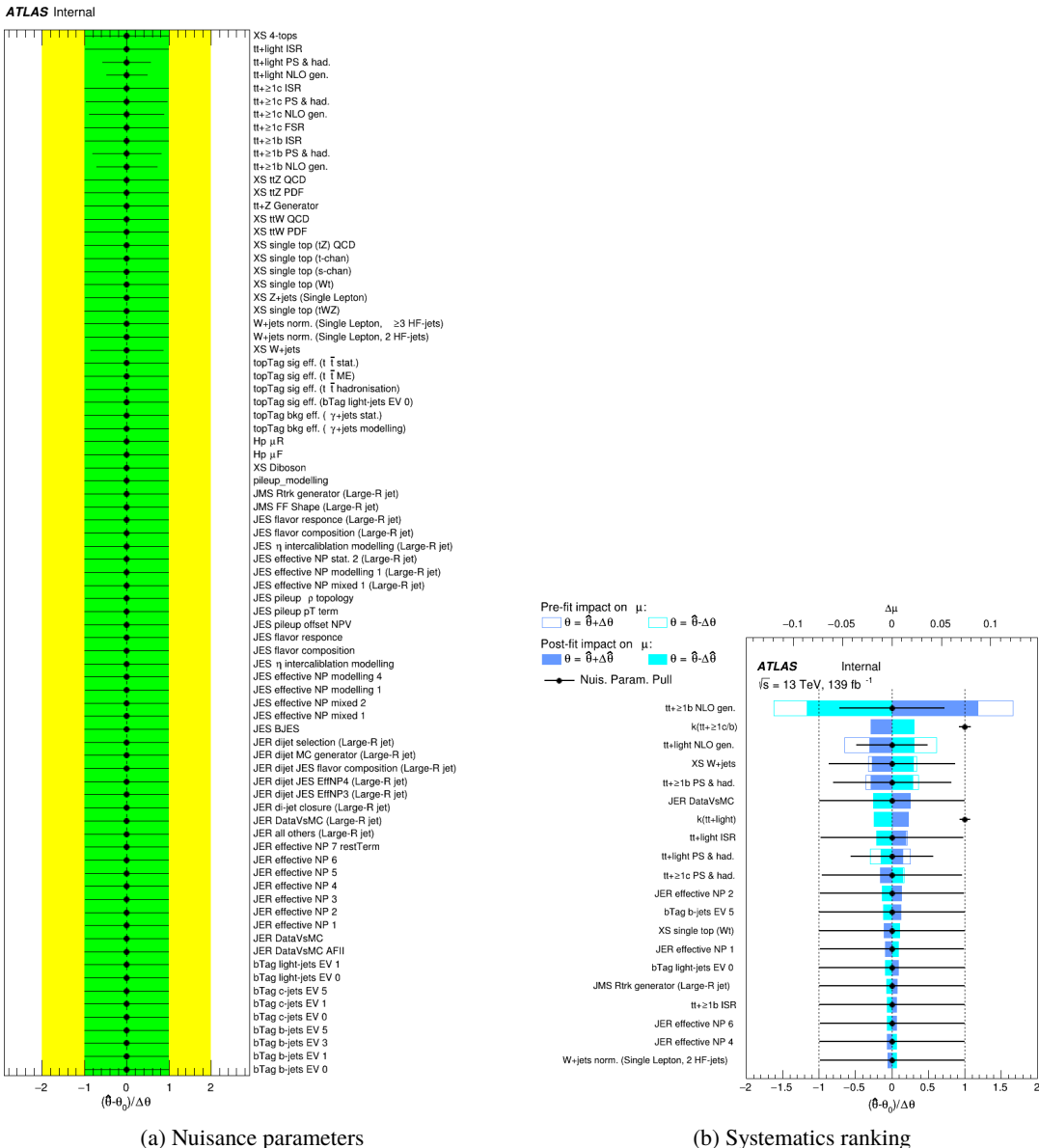
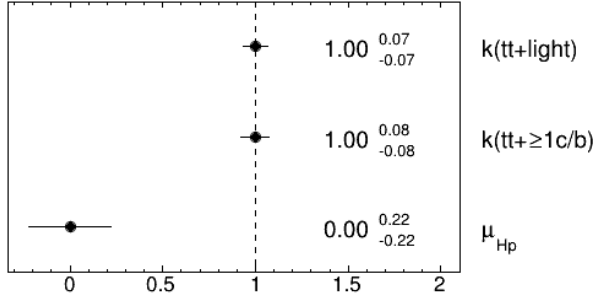


Figure 34: Nuisance parameters (left) and ranking plot (right) of the effect of various nuisance parameters before and after the fit for the 1800 GeV H^+ mass hypotheses.

ATLAS Internal

(a) Norm. factors

ATLAS Internal

	bTag b-jets EV 0	-0.2	-0.0	-0.4	-0.2	-0.2	0.1	1.1	-0.2	-2.4	1.6	1.1	1.3	0.3	3.2	-5.0	1.0	51.6	-9.5
bTag b-jets EV 1	-0.2	100.0	-0.0	-0.3	-0.1	-0.1	0.1	0.8	-0.1	-1.8	1.1	0.7	0.9	0.2	2.5	-3.7	0.7	32.8	-6.0
bTag light-jets EV 0	-0.0	-0.0	100.0	0.1	0.0	-0.0	-0.0	-0.1	-0.0	0.4	-0.6	0.1	0.1	0.0	-0.4	-0.3	2.9	26.3	-1.8
JES pileup p topology	-0.4	-0.3	0.1	100.0	-0.3	-0.1	0.2	3.1	-0.1	-6.4	1.6	-0.8	0.4	0.3	1.9	-13.8	1.2	-41.3	11.0
active NP modelling 1 (Large-R jet)	-0.2	-0.1	0.0	-0.3	100.0	-0.1	0.1	0.7	-0.1	-1.5	1.2	0.4	0.5	0.2	2.1	-2.2	-2.0	-21.6	-34.4
calibration modelling (Large-R jet)	-0.2	-0.1	-0.0	-0.1	-0.1	100.0	0.0	0.6	-0.1	-0.9	1.2	0.9	0.7	0.2	1.2	-2.0	-0.1	12.0	-20.7
topTag bkg eff. (γ+jets modelling)	0.1	0.1	-0.0	0.2	0.1	0.0	100.0	-0.5	0.1	0.5	-3.1	-0.4	-0.7	-1.0	-1.7	-2.9	1.7	-20.2	-1.6
topTag sig eff. (t̄t hadronisation)	1.1	0.8	-0.1	3.1	0.7	0.6	-0.5	100.0	0.6	12.3	-10.7	-5.9	-5.4	-1.7	-13.9	23.9	1.4	-20.0	-56.7
topTag sig eff. (t̄t stat.)	-0.2	-0.1	-0.0	-0.1	-0.1	-0.1	0.1	0.6	100.0	-0.9	1.7	1.1	0.8	0.2	1.4	-1.8	-1.6	1.1	-25.8
XS W+jets	-2.4	-1.8	0.4	-6.4	-1.5	-0.9	0.5	12.3	-0.9	100.0	2.2	-5.4	6.0	2.0	48.0	-51.3	-9.8	14.5	-62.2
tt+≥1b NLO gen.	1.6	1.1	-0.6	1.6	1.2	1.2	-3.1	-10.7	1.7	2.2	100.0	-51.2	-12.9	-12.2	0.2	-24.8	39.5	-0.2	2.8
tt+≥1b PS & had.	1.1	0.7	0.1	-0.8	0.4	0.9	-0.4	-5.9	1.1	-5.4	-51.2	100.0	-18.2	-5.2	-8.3	-1.5	-9.8	2.6	5.0
tt+≥1c NLO gen.	1.3	0.9	0.1	0.4	0.5	0.7	-0.7	-5.4	0.8	6.0	-12.9	-18.2	100.0	-6.8	-39.7	-2.5	-0.9	3.5	-2.2
tt+≥1c PS & had.	0.3	0.2	0.0	0.3	0.2	0.2	-1.0	-1.7	0.2	2.0	-12.2	-5.2	-6.8	100.0	-27.3	-18.2	-5.2	1.4	-0.8
tt+light NLO gen.	3.2	2.5	-0.4	1.9	2.1	1.2	-1.7	-13.9	1.4	48.0	0.2	-8.3	-39.7	-27.3	100.0	-31.9	-10.4	14.4	-26.2
tt+light PS & had.	-5.0	-3.7	-0.3	-13.8	-2.2	-2.0	-2.9	23.9	-1.8	-51.3	-24.8	-1.5	-2.5	-18.2	-31.9	100.0	5.2	-13.5	23.1
μ_{H_p}	1.0	0.7	2.9	1.2	-2.0	-0.1	1.7	1.4	-1.6	-9.8	39.5	-9.8	-0.9	-5.2	-10.4	5.2	100.0	-10.0	8.1
$k(\text{tt+} \geq 1\text{c/b})$	51.6	32.8	26.3	-41.3	-21.6	12.0	-20.2	-20.0	1.1	14.5	-0.2	2.6	3.5	1.4	14.4	-13.5	-10.0	100.0	-10.8
$k(\text{tt+light})$	-9.5	-6.0	-1.8	11.0	-34.4	-20.7	-1.6	-66.7	-25.8	-62.2	2.8	5.0	-2.2	-0.8	-26.2	23.1	8.1	-10.8	100.0

(b) Correlation matrix

Figure 35: Signal strength and normalization factors (top) and correlation matrix (bottom) for the 1800 GeV H^+ mass hypotheses.

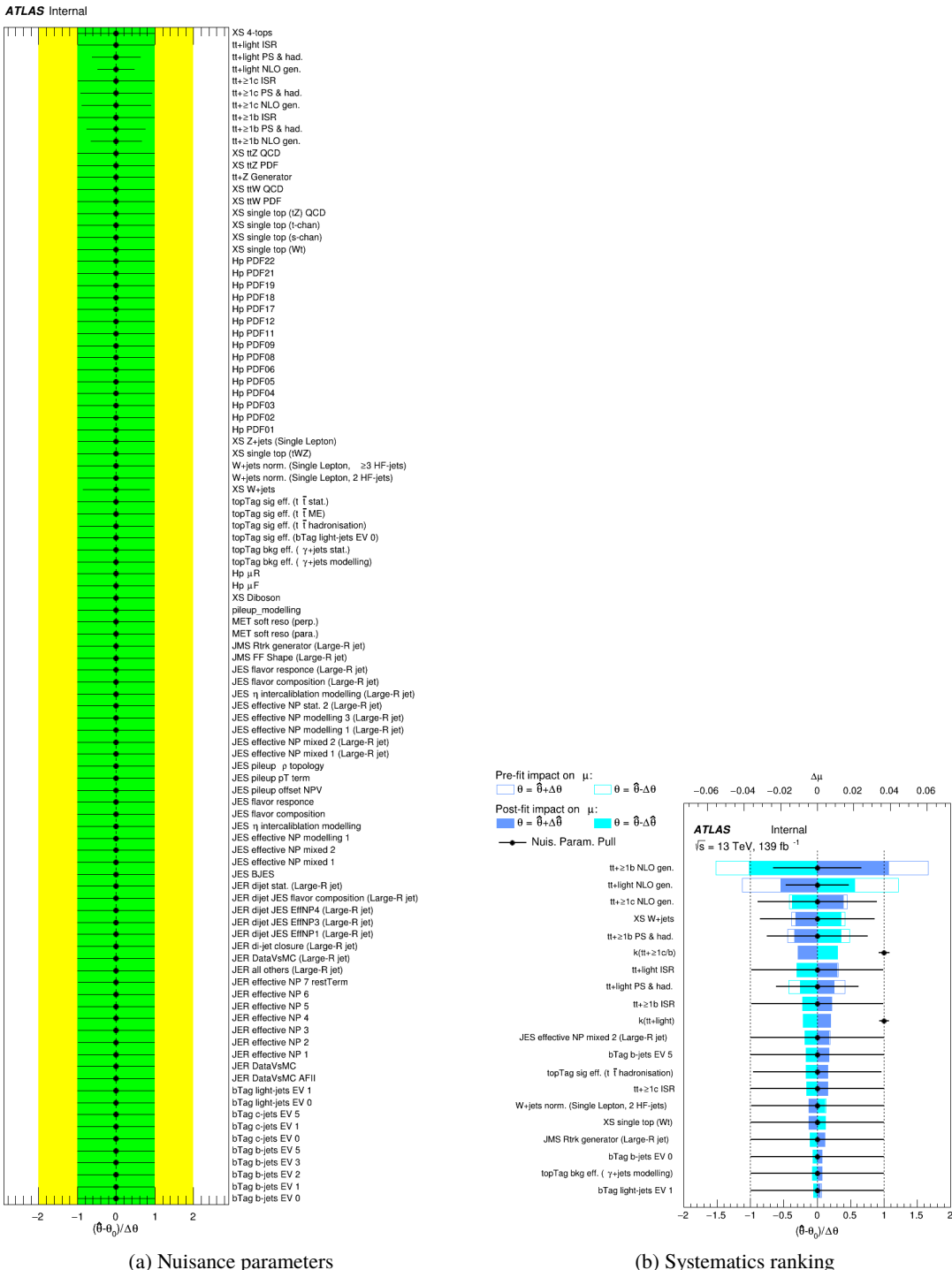
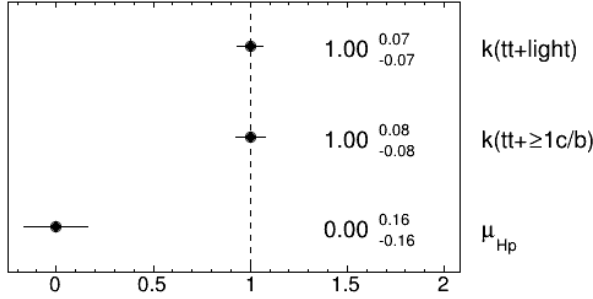


Figure 36: Nuisance parameters (left) and ranking plot (right) of the effect of various nuisance parameters before and after the fit for the 2000 GeV H^+ mass hypotheses.

ATLAS Internal**ATLAS Internal**

	bTag b-jets EV 0	-0.2	-0.1	-0.5	-0.1	-0.1	-0.0	1.2	-0.2	-2.5	0.7	1.3	1.0	0.1	4.2	-4.6	1.5	51.8	-9.5
bTag b-jets EV 1	-0.2	100.0	-0.0	-0.4	-0.1	-0.1	-0.0	0.9	-0.1	-1.9	0.5	0.7	0.7	0.1	3.2	-3.3	0.9	32.9	-6.0
bTag light-jets EV 0	-0.1	-0.0	100.0	0.2	0.0	-0.0	0.0	-0.1	-0.1	0.6	1.3	2.1	-0.1	-0.1	-0.1	-0.3	0.8	26.5	-2.0
JES pileup p topology	-0.5	-0.4	0.2	100.0	-0.3	-0.2	-0.0	4.3	-0.2	-8.0	-0.0	-2.1	1.7	-0.8	4.3	-11.0	-1.0	-41.7	11.5
active NP modelling 1 (Large-R jet)	-0.1	-0.1	0.0	-0.3	100.0	-0.0	0.0	0.7	-0.0	-1.6	0.6	-0.1	0.7	0.1	2.3	-2.0	-1.1	-21.7	-34.4
calibration modelling (Large-R jet)	-0.1	-0.1	-0.0	-0.2	-0.0	100.0	0.0	0.5	-0.1	-1.0	0.9	0.9	0.5	0.1	1.6	-1.9	0.0	12.0	-20.7
topTag bkg eff. (γ+jets modelling)	-0.0	-0.0	0.0	-0.0	0.0	0.0	100.0	0.0	0.0	-0.2	-3.1	-0.2	-1.4	-1.2	-0.4	-2.6	1.6	-20.5	-1.4
topTag sig eff. (t̄t hadronisation)	1.2	0.9	-0.1	4.3	0.7	0.5	0.0	100.0	0.6	13.8	-6.4	-3.8	-3.6	1.0	-19.1	19.4	3.6	-20.3	-57.3
topTag sig eff. (t̄t stat.)	-0.2	-0.1	-0.1	-0.2	-0.0	-0.1	0.0	0.6	100.0	-0.9	1.4	1.2	0.5	-0.0	1.8	-1.8	-1.1	1.1	-25.8
XS W+jets	-2.5	-1.9	0.6	-8.0	-1.6	-1.0	-0.2	13.8	-0.9	100.0	-3.4	-11.7	11.4	2.0	50.1	-40.6	-7.8	14.4	-62.3
tt+≥1b NLO gen.	0.7	0.5	1.3	-0.0	0.6	0.9	-3.1	-6.4	1.4	-3.4	100.0	-63.3	-18.3	-7.0	7.2	-20.1	23.4	0.5	4.4
tt+≥1b PS & had.	1.3	0.7	2.1	-2.1	-0.1	0.9	-0.2	-3.8	1.2	-11.7	-63.3	100.0	-0.4	4.6	-22.9	-1.6	-7.9	2.0	8.1
tt+≥1c NLO gen.	1.0	0.7	-0.1	1.7	0.7	0.5	-1.4	-3.6	0.5	11.4	-18.3	-0.4	100.0	-15.4	-36.3	-8.9	8.6	2.5	-6.1
tt+≥1c PS & had.	0.1	0.1	-0.1	-0.8	0.1	0.1	-1.2	1.0	-0.0	2.0	-7.0	4.6	-15.4	100.0	-26.3	-17.2	-0.5	0.6	-1.9
tt+light NLO gen.	4.2	3.2	-0.1	4.3	2.3	1.6	-0.4	-19.1	1.8	50.1	7.2	-22.9	-36.3	-26.3	100.0	-39.6	-12.4	15.7	-25.2
tt+light PS & had.	-4.6	-3.3	-0.3	-11.0	-2.0	-1.9	-2.6	19.4	-1.8	-40.6	-20.1	-1.6	-8.9	-17.2	-39.6	100.0	5.8	-11.4	18.5
μ_{H_p}	1.5	0.9	0.8	-1.0	-1.1	0.0	1.6	3.6	-1.1	-7.8	23.4	-7.9	8.6	-0.5	-12.4	5.8	100.0	-6.7	4.7
$k(t t+ \geq 1 c/b)$	51.8	32.9	26.5	-41.7	-21.7	12.0	-20.5	-20.3	1.1	14.4	0.5	2.0	2.5	0.6	15.7	-11.4	-6.7	100.0	-10.5
$k(t t+ light)$	-9.5	-6.0	-2.0	11.5	-34.4	-20.7	-1.4	-57.3	-25.8	-62.3	4.4	8.1	-6.1	-1.9	-25.2	18.5	4.7	-10.5	100.0

(b) Correlation matrix

Figure 37: Signal strength and normalization factors (top) and correlation matrix (bottom) for the 2000 GeV H^+ mass hypotheses.

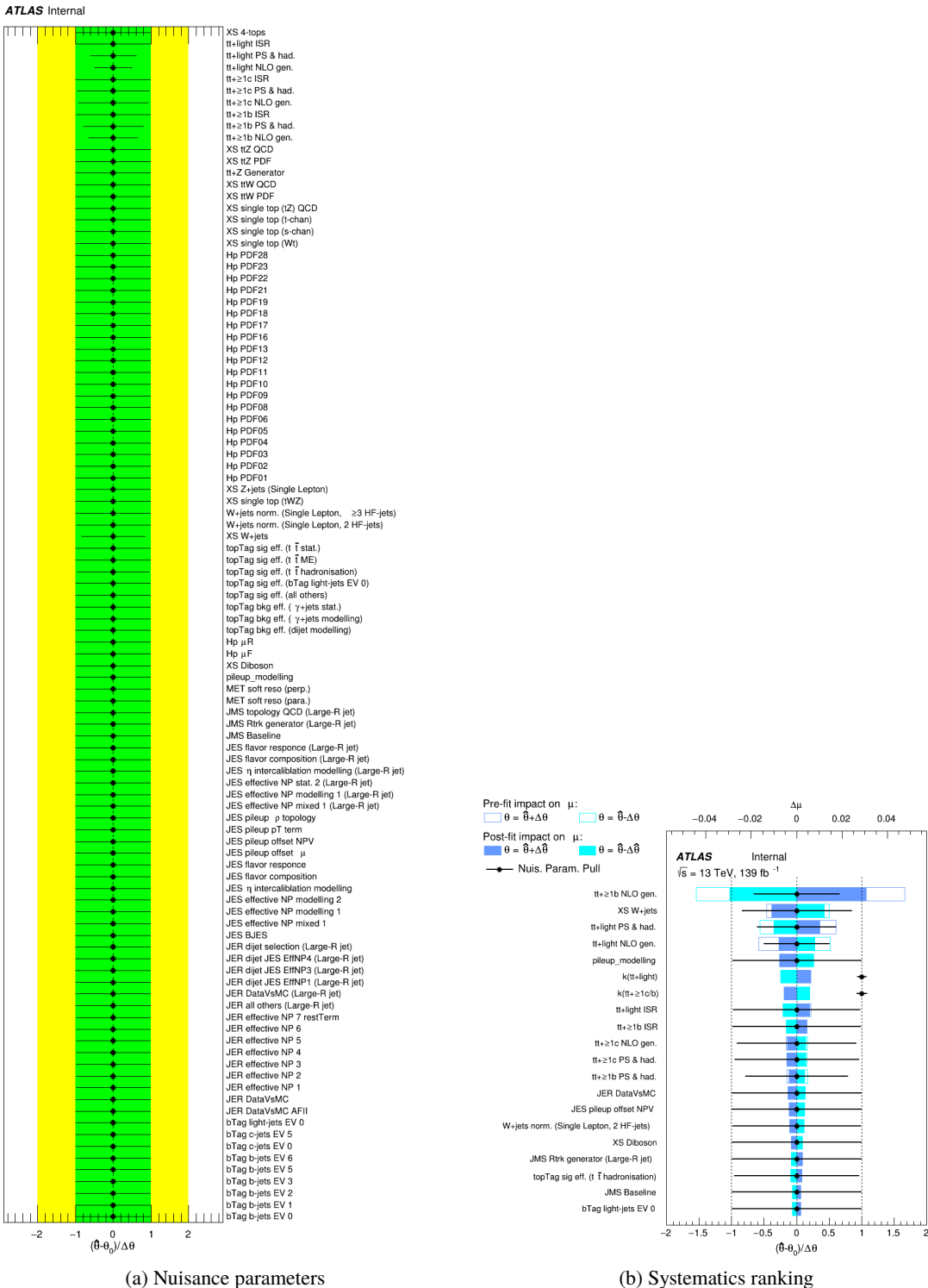
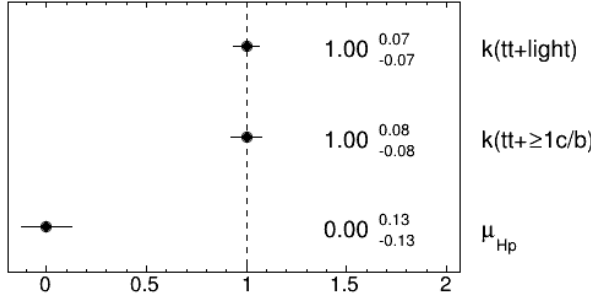


Figure 38: Nuisance parameters (left) and ranking plot (right) of the effect of various nuisance parameters before and after the fit for the 2500 GeV H^+ mass hypotheses.

ATLAS Internal

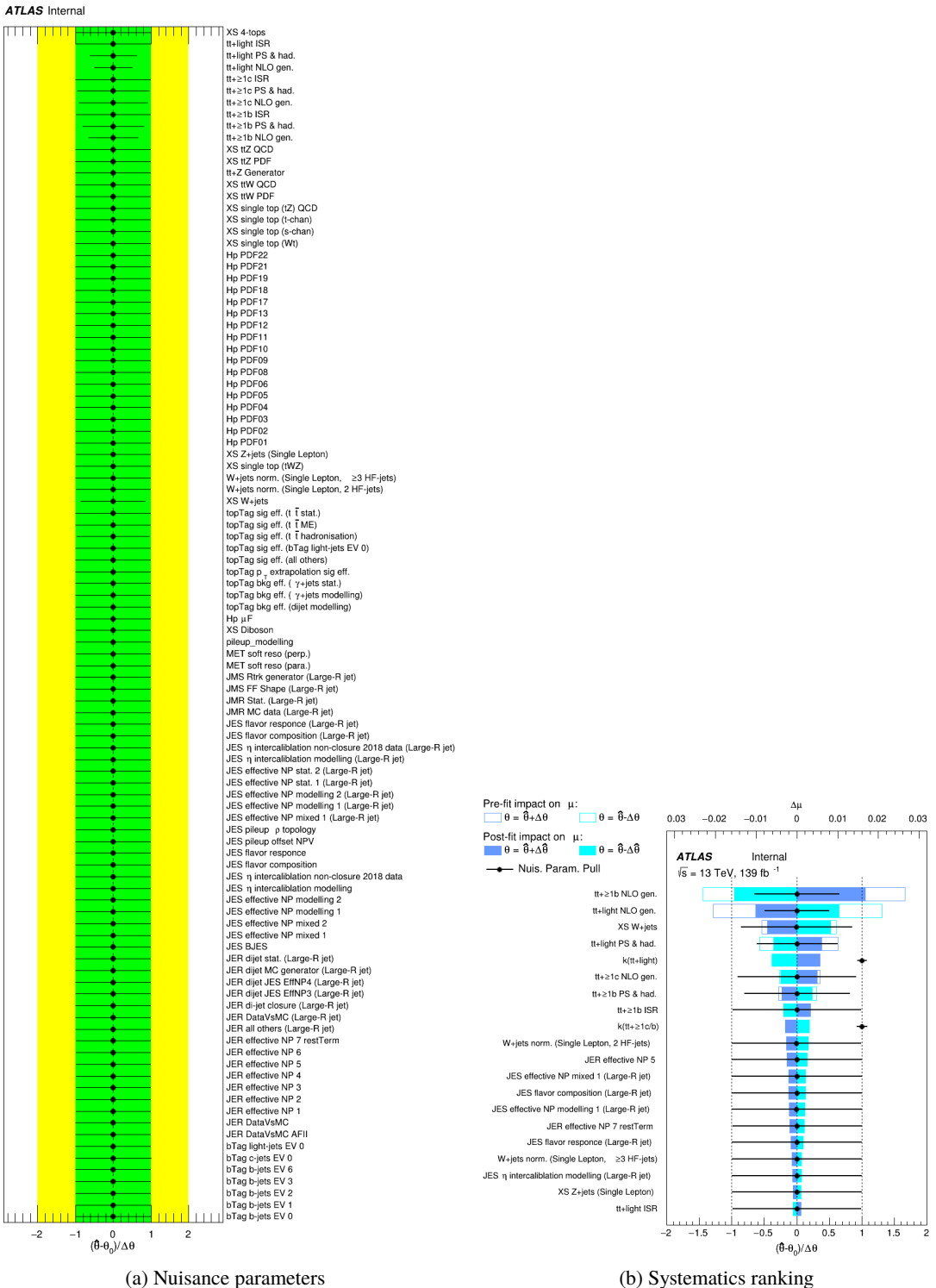
(a) Norm. factors

ATLAS Internal

	bTag b-jets EV 0	-0.2	-0.1	-0.6	-0.2	-0.1	-0.0	1.2	-0.1	-2.7	0.2	0.4	0.9	0.2	4.0	-4.5	1.1	51.9	-9.5
bTag b-jets EV 1	-0.2	100.0	-0.0	-0.5	-0.1	-0.1	-0.0	0.9	-0.1	-2.0	0.1	0.2	0.6	0.1	3.0	-3.2	0.6	33.0	-6.0
bTag light-jets EV 0	-0.1	-0.0	100.0	0.0	-0.0	-0.0	0.0	-0.1	-0.0	0.1	-0.9	-0.4	0.0	0.2	-0.4	-0.5	1.4	26.5	-1.7
JES pileup p topology	-0.6	-0.5	0.0	100.0	-0.4	-0.2	-0.0	4.2	-0.2	-8.5	-0.3	-2.1	0.7	-1.5	4.6	-10.5	-1.4	-41.9	11.9
active NP modelling 1 (Large-R jet)	-0.2	-0.1	-0.0	-0.4	100.0	-0.0	0.0	0.7	-0.0	-2.1	-0.7	-1.4	0.0	-0.0	2.3	-1.6	-0.0	-21.9	-34.2
calibration modelling (Large-R jet)	-0.1	-0.1	-0.0	-0.2	-0.0	100.0	0.0	0.5	-0.1	-1.0	0.6	0.6	0.5	0.1	1.6	-1.9	0.2	12.1	-20.8
topTag bkg eff. ($\gamma + \text{jets}$ modelling)	-0.0	-0.0	0.0	-0.0	0.0	0.0	100.0	0.1	0.0	-0.1	-2.5	-0.1	-0.5	-0.6	-1.1	-2.6	1.0	-20.4	-1.5
topTag sig eff. ($t\bar{t}$ hadronisation)	1.2	0.9	-0.1	4.2	0.7	0.5	0.1	100.0	0.5	13.9	-3.7	-2.6	-3.7	0.9	-18.3	20.4	1.9	-20.2	-57.8
topTag sig eff. ($t\bar{t}$ stat.)	-0.1	-0.1	-0.0	-0.2	-0.0	-0.1	0.0	0.5	100.0	-1.0	1.1	0.9	0.5	0.0	1.8	-1.8	-0.3	1.1	-25.9
XS W+jets	-2.7	-2.0	0.1	-8.5	-2.1	-1.0	-0.1	13.9	-1.0	100.0	-4.8	-13.2	4.5	-0.8	50.2	-37.6	-9.2	14.0	-61.6
$t\bar{t}+\geq 1\text{b}$ NLO gen.	0.2	0.1	-0.9	-0.3	-0.7	0.6	-2.5	-3.7	1.1	-4.8	100.0	-61.7	-18.6	-1.0	2.1	-15.6	23.7	-0.6	4.5
$t\bar{t}+\geq 1\text{b}$ PS & had.	0.4	0.2	-0.4	-2.1	-1.4	0.6	-0.1	-2.6	0.9	-13.2	-61.7	100.0	-16.9	-1.8	-12.7	9.2	-2.9	-0.1	9.2
$t\bar{t}+\geq 1\text{c}$ NLO gen.	0.9	0.6	0.0	0.7	0.0	0.5	-0.5	-3.7	0.5	4.5	-18.6	-16.9	100.0	-7.7	-43.9	-8.5	-3.3	2.5	-1.6
$t\bar{t}+\geq 1\text{c}$ PS & had.	0.2	0.1	0.2	-1.5	-0.0	0.1	-0.6	0.9	0.0	-0.8	-1.0	-1.8	-7.7	100.0	-32.3	-15.7	-3.3	0.8	-0.1
$t\bar{t}+\text{light}$ NLO gen.	4.0	3.0	-0.4	4.6	2.3	1.6	-1.1	-18.3	1.8	50.2	2.1	-12.7	-43.9	-32.3	100.0	-36.6	-6.3	14.6	-25.2
$t\bar{t}+\text{light}$ PS & had.	-4.5	-3.2	-0.5	-10.5	-1.6	-1.9	-2.6	20.4	-1.8	-37.6	-15.6	9.2	-8.5	-15.7	-36.6	100.0	8.0	-11.1	15.7
μ_{H_p}	1.1	0.6	1.4	-1.4	-0.0	0.2	1.0	1.9	-0.3	-9.2	23.7	-2.9	-3.3	-3.3	-6.3	8.0	100.0	-4.5	5.3
$k(t\bar{t}+\geq 1\text{c}/b)$	51.9	33.0	26.5	-41.9	-21.9	12.1	-20.4	-20.2	1.1	14.0	-0.6	-0.1	2.5	0.8	14.6	-11.1	-4.5	100.0	-10.2
$k(t\bar{t}+\text{light})$	-9.5	-6.0	-1.7	11.9	-34.2	-20.8	-1.5	-57.8	-25.9	-61.6	4.5	9.2	-1.6	-0.1	-25.2	15.7	5.3	-10.2	100.0

(b) Correlation matrix

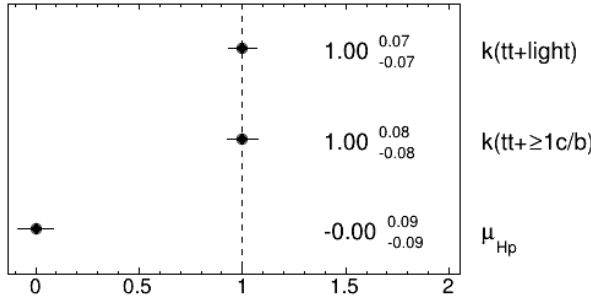
Figure 39: Signal strength and normalization factors (top) and correlation matrix (bottom) for the 2500 GeV H^+ mass hypotheses.



(a) Nuisance parameters

(b) Systematics ranking

Figure 40: Nuisance parameters (left) and ranking plot (right) of the effect of various nuisance parameters before and after the fit for the 3000 GeV H^+ mass hypotheses.

ATLAS Internal

(a) Norm. factors

ATLAS Internal

	bTag b-jets EV 0	-0.2	-0.1	-0.5	-0.1	-0.1	-0.0	1.1	-0.1	-2.5	-0.8	0.6	0.8	0.3	4.1	-5.0	52.0	-9.5
bTag b-jets EV 1	-0.2	100.0	-0.0	-0.4	-0.1	-0.1	-0.0	0.9	-0.1	-2.0	-0.6	0.3	0.6	0.2	3.1	-3.5	33.0	-6.0
bTag light-jets EV 0	-0.1	-0.0	100.0	-0.0	0.0	0.0	-0.0	-0.0	-0.5	-3.5	-1.6	-0.6	0.2	-0.4	-0.6	26.5	-1.4	
JES pileup p topology	-0.5	-0.4	-0.0	100.0	-0.4	-0.2	-0.2	4.4	-0.2	-8.8	-2.7	-3.3	1.2	-1.4	4.2	-10.2	-42.0	11.9
active NP modelling 1 (Large-R jet)	-0.1	-0.1	0.0	-0.4	100.0	-0.1	-0.0	0.7	-0.1	-1.7	0.6	-0.1	0.3	-0.1	2.3	-1.8	-21.8	-34.3
calibration modelling (Large-R jet)	-0.1	-0.1	0.0	-0.2	-0.1	100.0	0.0	0.5	-0.1	-0.9	1.7	1.3	0.5	0.1	1.6	-2.0	12.2	-20.7
topTag bkg eff. ($t\bar{t}$ +jets modelling)	-0.0	-0.0	-0.0	-0.2	-0.0	0.0	100.0	0.2	0.0	-0.6	-2.0	-1.1	-0.6	-0.7	-1.5	-2.1	-20.5	-1.2
topTag sig eff. ($t\bar{t}$ hadronisation)	1.1	0.9	-0.0	4.4	0.7	0.5	0.2	100.0	0.5	14.7	-1.1	0.4	-4.1	0.8	-17.9	19.5	-20.1	-57.8
topTag sig eff. ($t\bar{t}$ stat.)	-0.1	-0.1	-0.0	-0.2	-0.1	-0.1	0.0	0.5	100.0	-1.0	0.8	0.8	0.4	0.1	1.8	-2.0	1.1	-25.7
XS W+jets	-2.5	-2.0	-0.5	-8.8	-1.7	-0.9	-0.6	14.7	-1.0	100.0	-12.0	12.4	6.9	-0.1	50.1	-36.9	14.0	-62.4
$t\bar{t}+\geq 1b$ NLO gen.	-0.8	-0.6	-3.5	-2.7	0.6	1.7	-2.0	-1.1	0.8	-12.0	100.0	-60.4	-23.6	-3.2	-3.2	-5.6	-2.8	7.1
$t\bar{t}+\geq 1b$ PS & had.	0.6	0.3	-1.6	-3.3	-0.1	1.3	-1.1	0.4	0.8	-12.4	-60.4	100.0	-10.6	-2.3	-17.4	15.0	-0.2	6.6
$t\bar{t}+\geq 1c$ NLO gen.	0.8	0.6	-0.6	1.2	0.3	0.5	-0.6	-4.1	0.4	6.9	-23.6	-10.6	100.0	-8.0	-41.5	-11.7	2.1	-2.8
$t\bar{t}+\geq 1c$ PS & had.	0.3	0.2	0.2	-1.4	-0.1	0.1	-0.7	0.8	0.1	-0.1	-3.2	-2.3	-8.0	100.0	-31.3	-16.8	1.0	-0.6
tt+light NLO gen.	4.1	3.1	-0.4	4.2	2.3	1.6	-1.5	-17.9	1.8	50.1	-3.2	-17.4	-41.5	-31.3	100.0	-35.3	15.0	-25.5
tt+light PS & had.	-5.0	-3.5	-0.6	-10.2	-1.8	-2.0	-2.1	19.5	-2.0	-36.9	-5.6	15.0	-11.7	-16.8	-35.3	100.0	-11.5	16.0
$k_{(t\bar{t}+\geq 1c/b)}$	52.0	33.0	26.5	-42.0	-21.8	12.2	-20.5	-20.1	1.1	14.0	-2.8	-0.2	2.1	1.0	15.0	-11.5	100.0	-10.3
$k_{(t\bar{t}+\text{light})}$	-9.5	-6.0	-1.4	11.9	-34.3	-20.7	-1.2	-57.8	-25.7	-62.4	7.1	6.6	-2.8	-0.6	-25.5	16.0	-10.3	100.0

(b) Correlation matrix

Figure 41: Signal strength and normalization factors (top) and correlation matrix (bottom) for the 3000 GeV H^+ mass hypotheses.

729 **7.4 Post-fit plots for Asimov fit**

730 Figures 42 to 49 show the post-fit distributions of the BDT output and H_T^{jets} for the fits using Asimov
 731 dataset under all H^+ mass hypotheses.

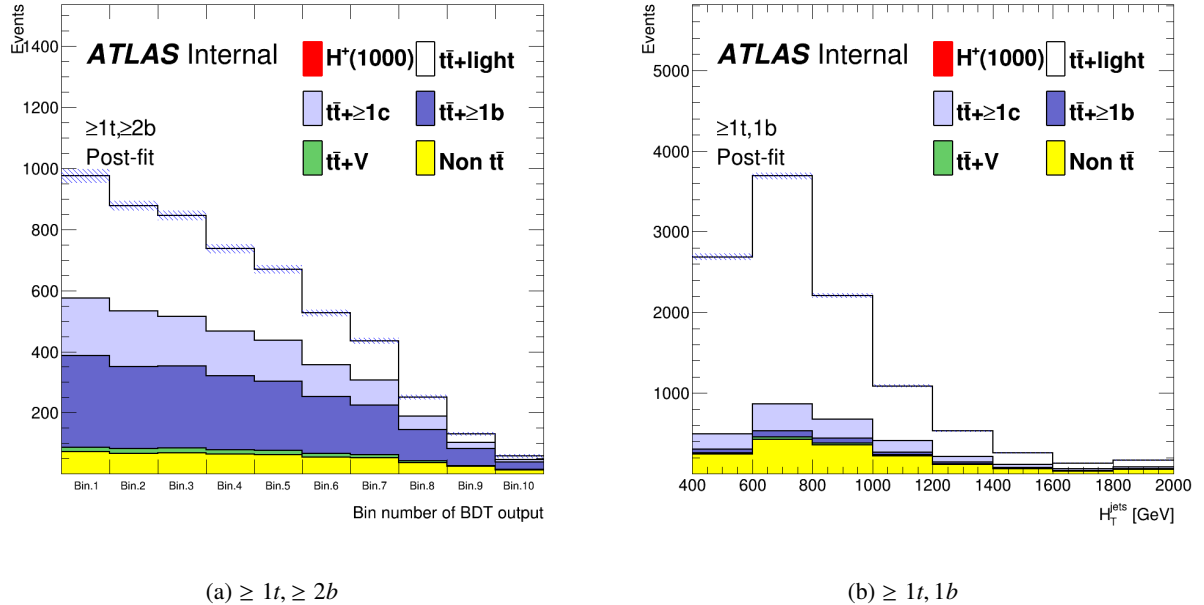


Figure 42: Post-fit distribution of BDT output and H_T^{jets} for the fits using Asimov dataset under the 1000 GeV H^+ mass hypotheses.

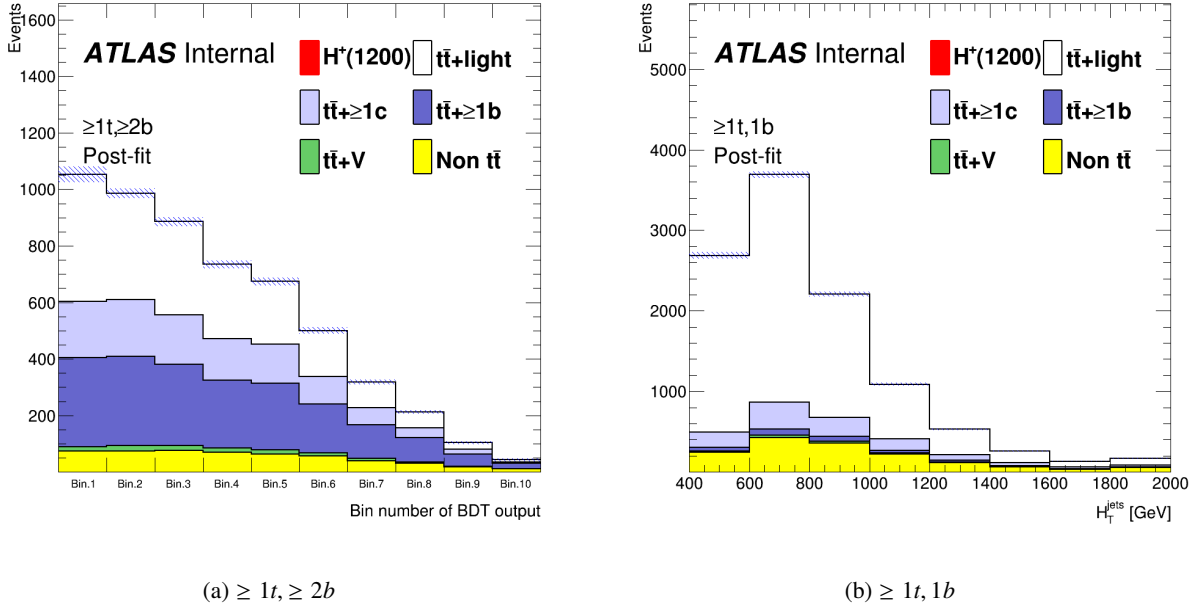


Figure 43: Post-fit distribution of BDT output and H_T^{jets} for the fits using Asimov dataset under the 1200 GeV H^+ mass hypotheses.

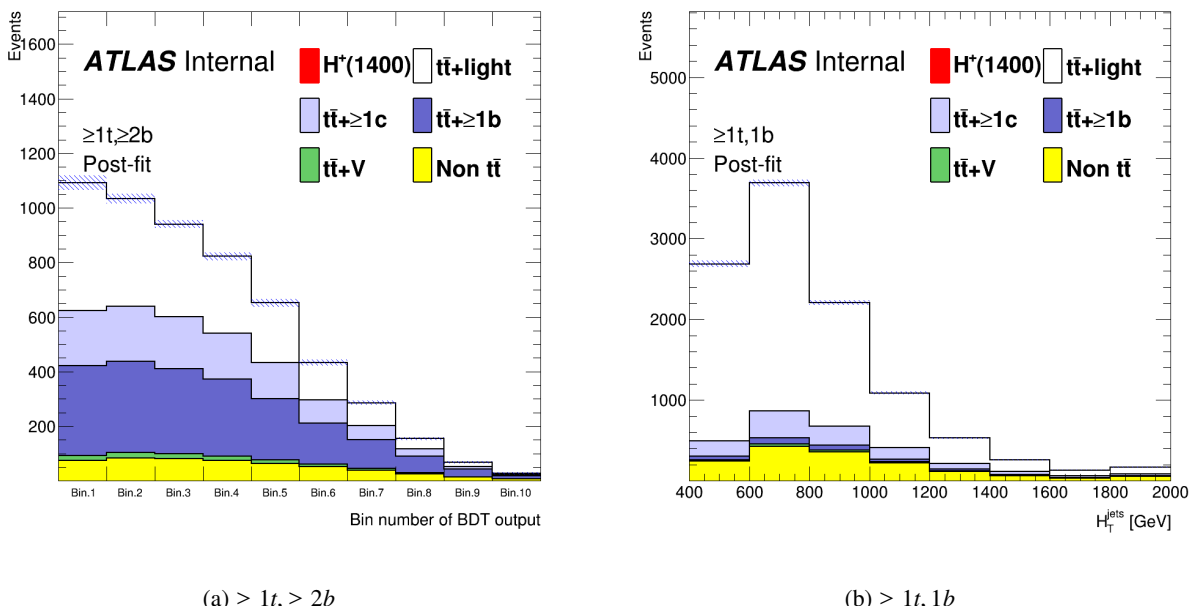


Figure 44: Post-fit distribution of BDT output and H_T^{jets} for the fits using Asimov dataset under the 1400 GeV H^+ mass hypotheses.

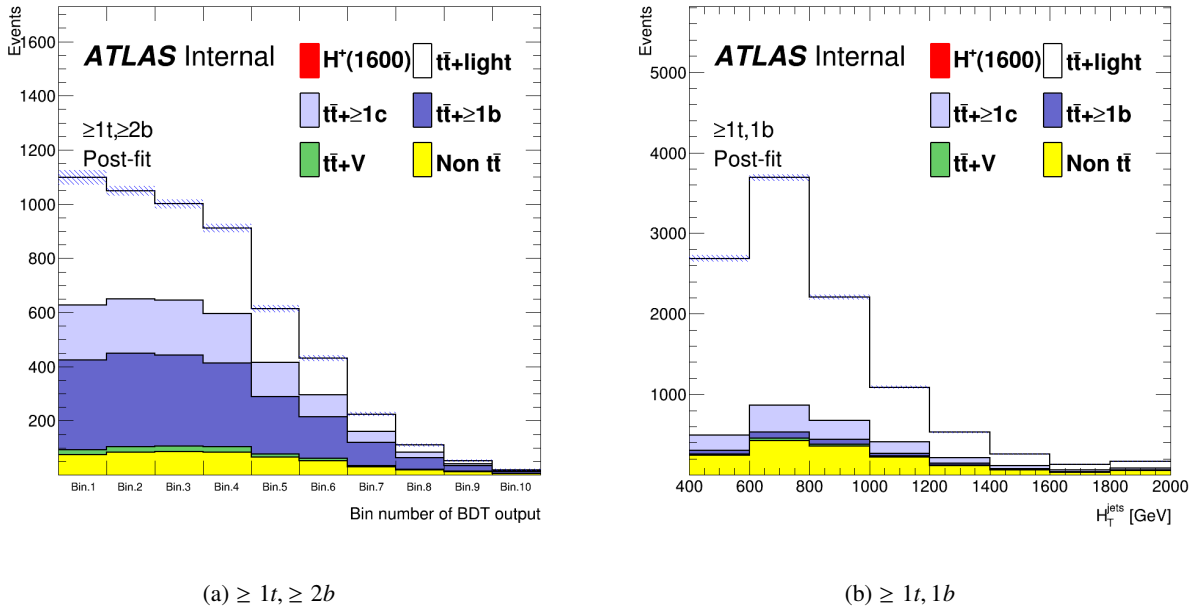


Figure 45: Post-fit distribution of BDT output and H_T^{jets} for the fits using Asimov dataset under the 1600 GeV H^+ mass hypotheses.

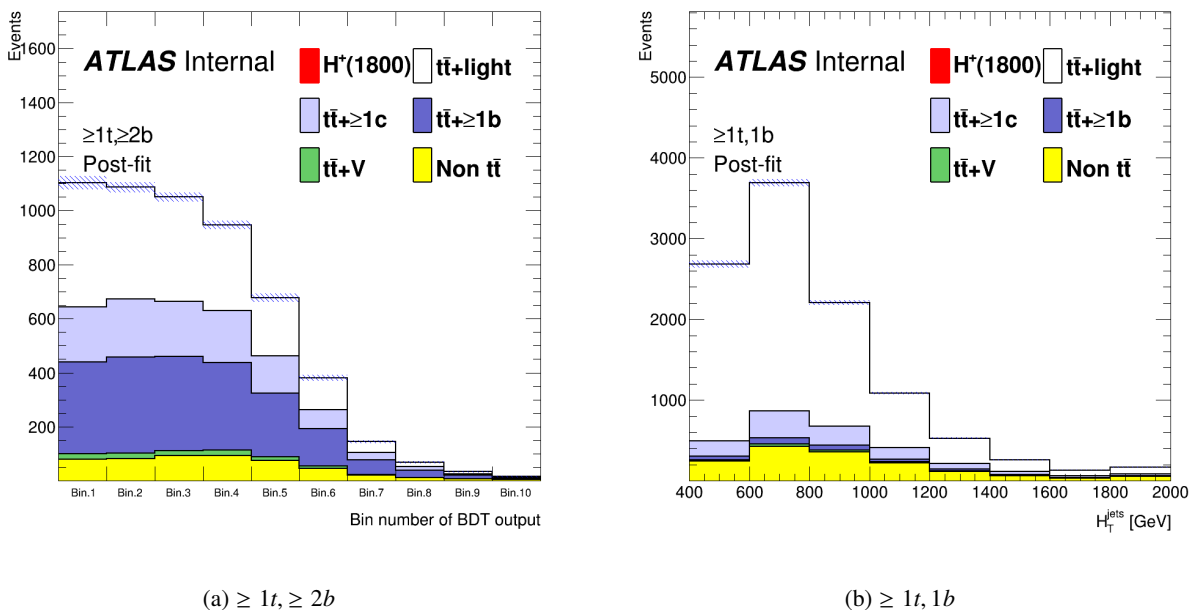


Figure 46: Post-fit distribution of BDT output and H_T^{jets} for the fits using Asimov dataset under the 1800 GeV H^+ mass hypotheses.

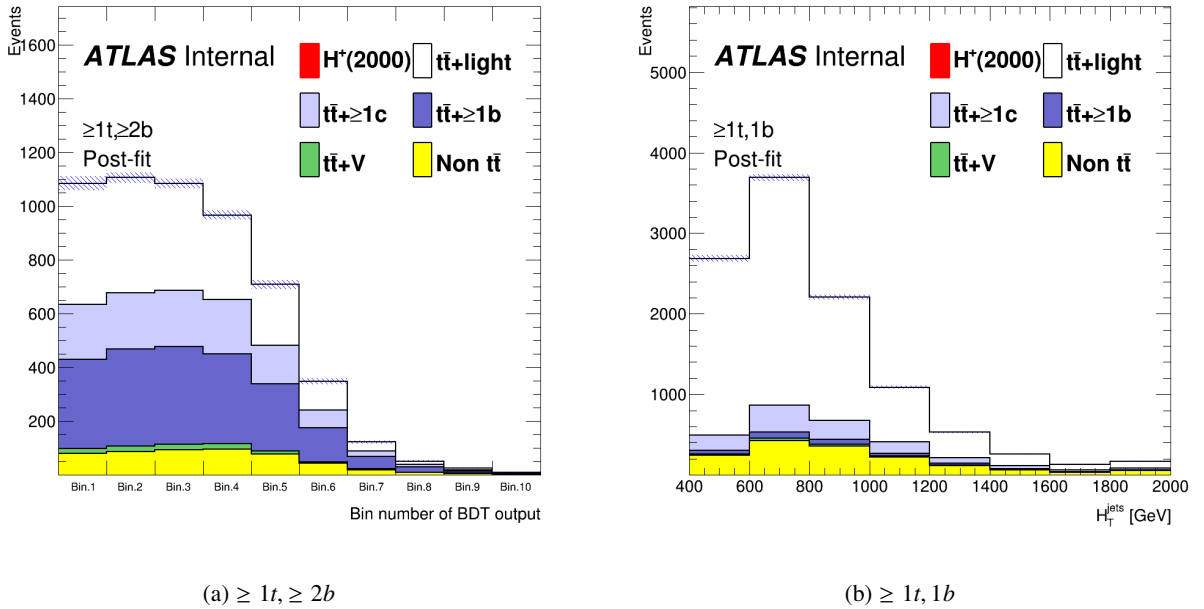


Figure 47: Post-fit distribution of BDT output and H_T^{jets} for the fits using Asimov dataset under the 2000 GeV H^+ mass hypotheses.

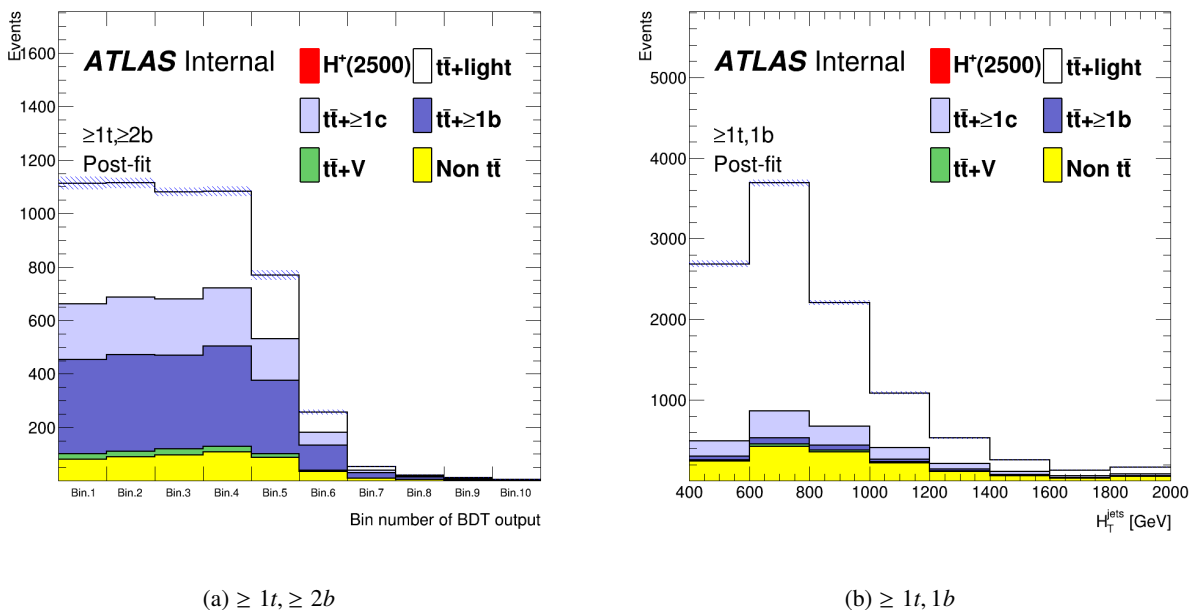


Figure 48: Post-fit distribution of BDT output and H_T^{jets} for the fits using Asimov dataset under the 2500 GeV H^+ mass hypotheses.

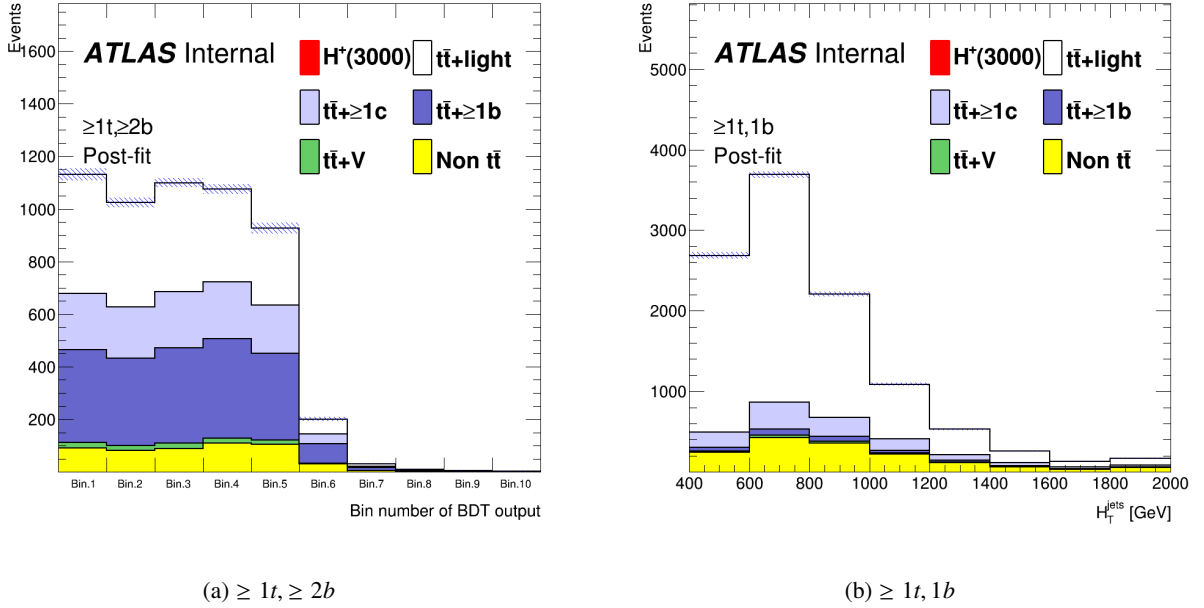


Figure 49: Post-fit distribution of BDT output and H_T^{jets} for the fits using Asimov dataset under the 3000 GeV H^+ mass hypotheses.

7.5 Asimov fit results summary

Figure 50 shows the fitted signal strength and $t\bar{t} + \text{light}$ and $t\bar{t} + \geq 1c/b$ normalisation factors as a function of the H^+ mass hypothesis of the Asimov fit.

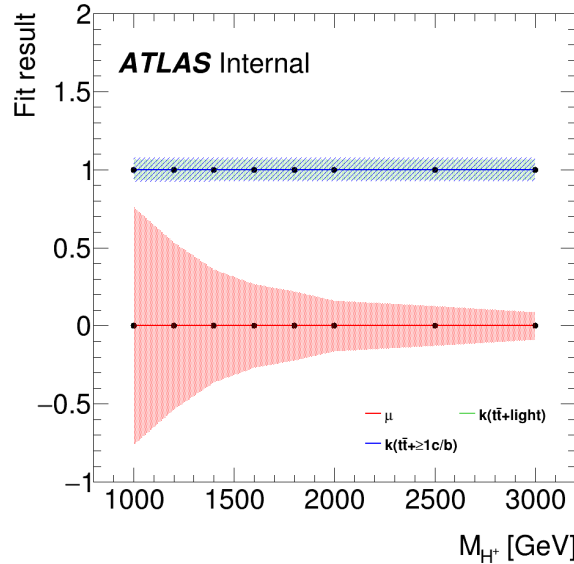


Figure 50: Fitted signal strength and $t\bar{t} + \text{light}$ and $t\bar{t} + \geq 1c/b$ normalisation factors as a function of the H^+ mass hypothesis of the Asimov fit

735 **7.6 Upper cross-section limits as a function of the H^+ mass**

736 The 95% confidence level (CL) upper limit for the production of $H^+ \rightarrow tb$ in association with a top quark
737 and a bottom quark using the CL_S method is shown in Figure 51.

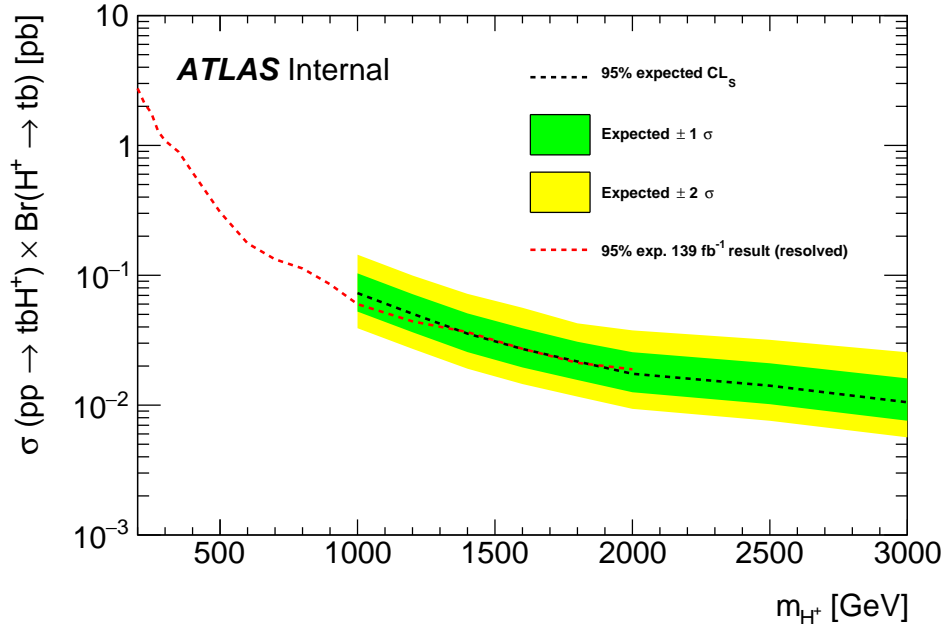


Figure 51: Expected limit for the production of $H^+ \rightarrow tb$ in association with a top quark and a bottom quark. The bands surrounding the expected limit show the 68% and 95% confidence intervals. The expected limit from ATLAS search using Run2 full data with resolved channel is also shown[24].

738 8 Test of tbW' generation

739 Motivation of this section is to check that we can apply same analysis framework to the tbW' search as tbH^+
 740 search. For that reason, we compared the kinematics of tbW' production with ones of tbH^+ production in
 741 the following sections. As result, there were no significant differences between these productions (Section
 742 8.2.3). Therefore, we continue to search tbW' production with same analysis framework as tbH^+ search.

743 8.1 tbW' MC generation in private

744 We also search for $W' \rightarrow tb$ decay with the search of $H^+ \rightarrow tb$ decay, where W' is produced in association with
 745 tb same as H^+ production. Before the official MC generation, the private MC samples for both left-handed
 746 (LH) and right-handed (RH) W' were generated using MadGraph5_aMC@NLO. These generated test
 747 samples are summarized in Table 14.

W' mass [GeV]	Type (LH or RH)	Size (events)
1000	LH	0.1M
1000	RH	0.1M
2000	LH	0.1M
2000	RH	0.1M
3000	LH	0.1M
3000	RH	0.1M
4000	LH	0.1M
4000	RH	0.1M
5000	LH	0.1M
5000	RH	0.1M

Table 14

748 8.2 Kinematics study in truth level

749 8.2.1 Reconstructed truth objects

750 To study the kinematics properties of $W' \rightarrow tb$ events in truth level, TruthDAOD samples were produced
 751 with *TRUTH1* format [120]. The following truth objects are reconstructed according to the official ATLAS
 752 truth object definition [121]. Moreover, overlapping objects are removed as shown in Table 16.

Truth object	Collection name
Truth electron	TruthElectrons
Truth muon	TruthMuons
Truth small-R jet (j^{truth})	AntiKt4TruthDressedWZJets
Truth large-R jet (J^{truth})	AntiKt10TruthTrimmedPtFrac5SmallR20Jets

Table 15: List of reconstructed truth objects in this study. Each object is selected from the indicated collection of with their corresponding aux containers.

Reject	Against	Criteria
Truth large- R jet	Truth electron	$\Delta R < 1.0$
Truth small- R jet	Truth large- R jet	$\Delta R < 1.0$

Table 16: Summary of overlap removal procedures among truth objects

753 8.2.2 Event selection

754 To study in the same phase space as the "SR" in Section 4.1.1, events are selected according to the number
 755 of truth leptons, small- R jets and large- R jets as shown in Table 17.

Cut	Criteria	
Truth leptons (ℓ^{truth})	Exactly 1 truth lepton in event	
	Truth electron	Truth muon
	$p_T > 27 \text{ GeV}$	$p_T > 27 \text{ GeV}$
	$ \eta < 1.37$ or $1.52 < \eta < 2.47$	$ \eta < 2.5$
≥ 1 truth large-R jets		
Truth large- R jets originated from top-quark ($J_{\text{top}}^{\text{truth}}$)	$350 \text{ GeV} < p_T < 2500 \text{ GeV}$	
	$ \eta < 2.0$	
	$\Delta R(t, J_{\text{top}}^{\text{truth}}) < 1.0$ or $\Delta R(\bar{t}, J_{\text{top}}^{\text{truth}}) < 1.0$	
	(t, \bar{t}) : truth particle labelled as PDG ID=6 (-6)	
≥ 2 truth small-R jets		
Truth small- R jets originated from b -quark ($b\text{-jet}^{\text{truth}}$)	$p_T > 25 \text{ GeV}$	
	$ \eta < 2.5$	
	PDG ID of the highest-E ghost parton is 5	

Table 17: Summary of event selections in truth level.

756 8.2.3 Kinematics comparison with $t b H^+$ events

757 Variables input to BDT training in Section 4.2.3 were defined in truth level as shown in Table 18. These
 758 distributions are compared between $t b W'$ and $t b H^+$ in Figure 52 to 55. These were no significant
 759 differences.

Symbol	Description
Truth_HT_jets	Scalar sum of the transverse energy of leading $J_{\text{top}}^{\text{truth}}$ and all j^{truth}
Truth_LeadingJet_pt	Leading j^{truth} p_T
Truth_Mjjj_MaxPt	Invariant mass of the j^{truth} triplet with maximum p_T
Truth_Mbb_MaxPt	Invariant mass of the b -jet $^{\text{truth}}$ pair with maximum p_T
Truth_Muu_MinDR	Invariant mass of the j^{truth} -pair with minimum ΔR except for b -jet $^{\text{truth}}$
Truth_dRlepb_MindR	ΔR between ℓ^{truth} and the pair of b -jet $^{\text{truth}}$ with smallest ΔR
Truth_dRbb_avg	Average ΔR between all b -jet $^{\text{truth}}$ pairs in the event
Truth_Centrality_all	Centrality calculated using leading $J_{\text{top}}^{\text{truth}}$, all j^{truth} and ℓ^{truth}
Truth_H1_all	Second Fox-Wolfram moment calculated using all j^{truth} and ℓ^{truth}
Truth_LeadingTop_pt	Leading $J_{\text{top}}^{\text{truth}}$ p_T
Truth_LeadingTop_m	Invariant mass of leading $J_{\text{top}}^{\text{truth}}$
Truth_Pt_tb	p_T of the pair of leading $J_{\text{top}}^{\text{truth}}$ and leading b -jet $^{\text{truth}}$
Truth_M_tb	Invariant mass of the pair of leading $J_{\text{top}}^{\text{truth}}$ and leading b -jet $^{\text{truth}}$
Truth_PtAsymm_tb	p_T asymmetry between leading $J_{\text{top}}^{\text{truth}}$ and leading b -jet $^{\text{truth}}$

Table 18: Definition of variables input to BDT training in truth level.

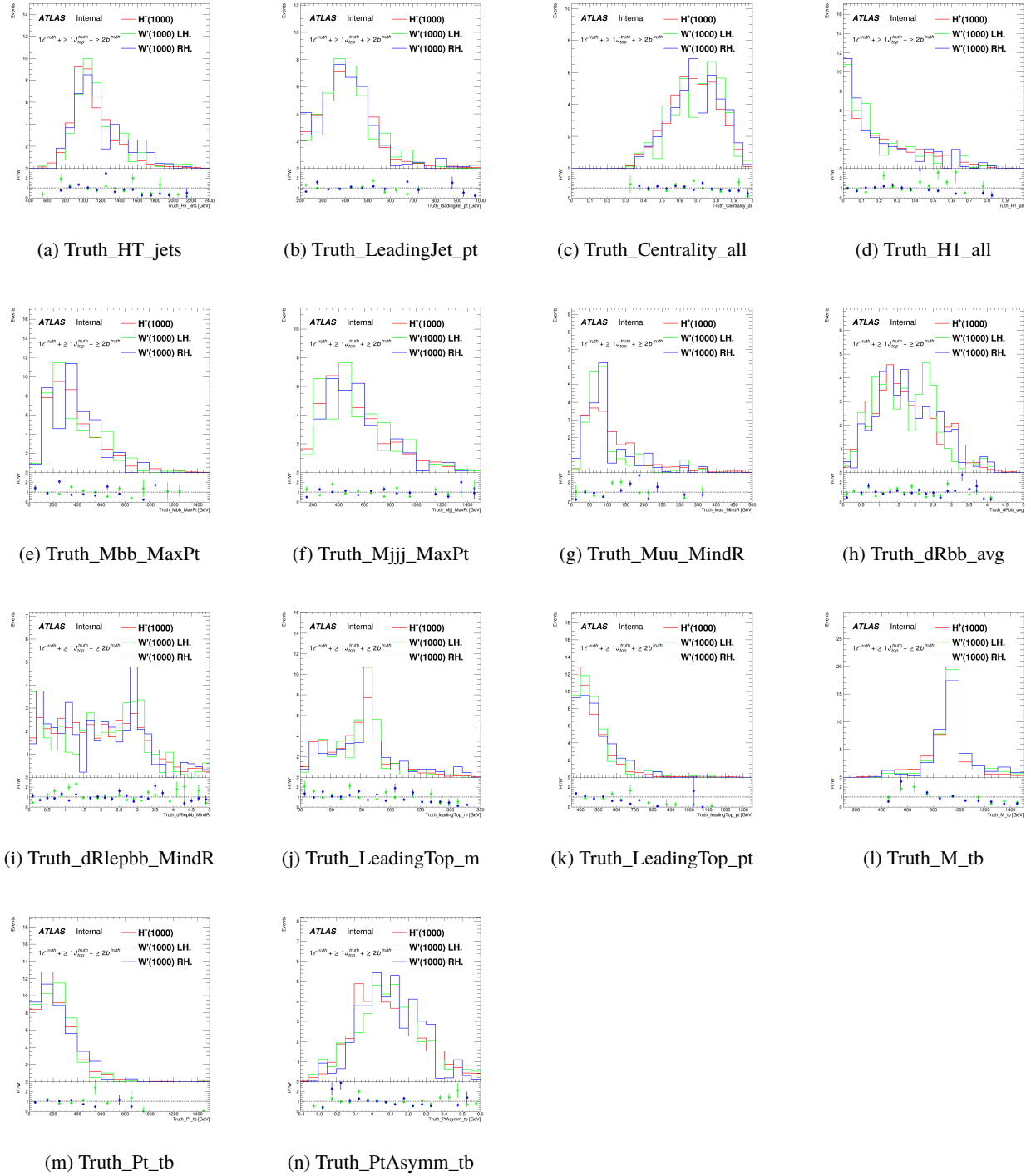


Figure 52: Comparison of the kinematic variables between tbW' and tbH^+ in truth level on 1000 GeV mass hypothesis.

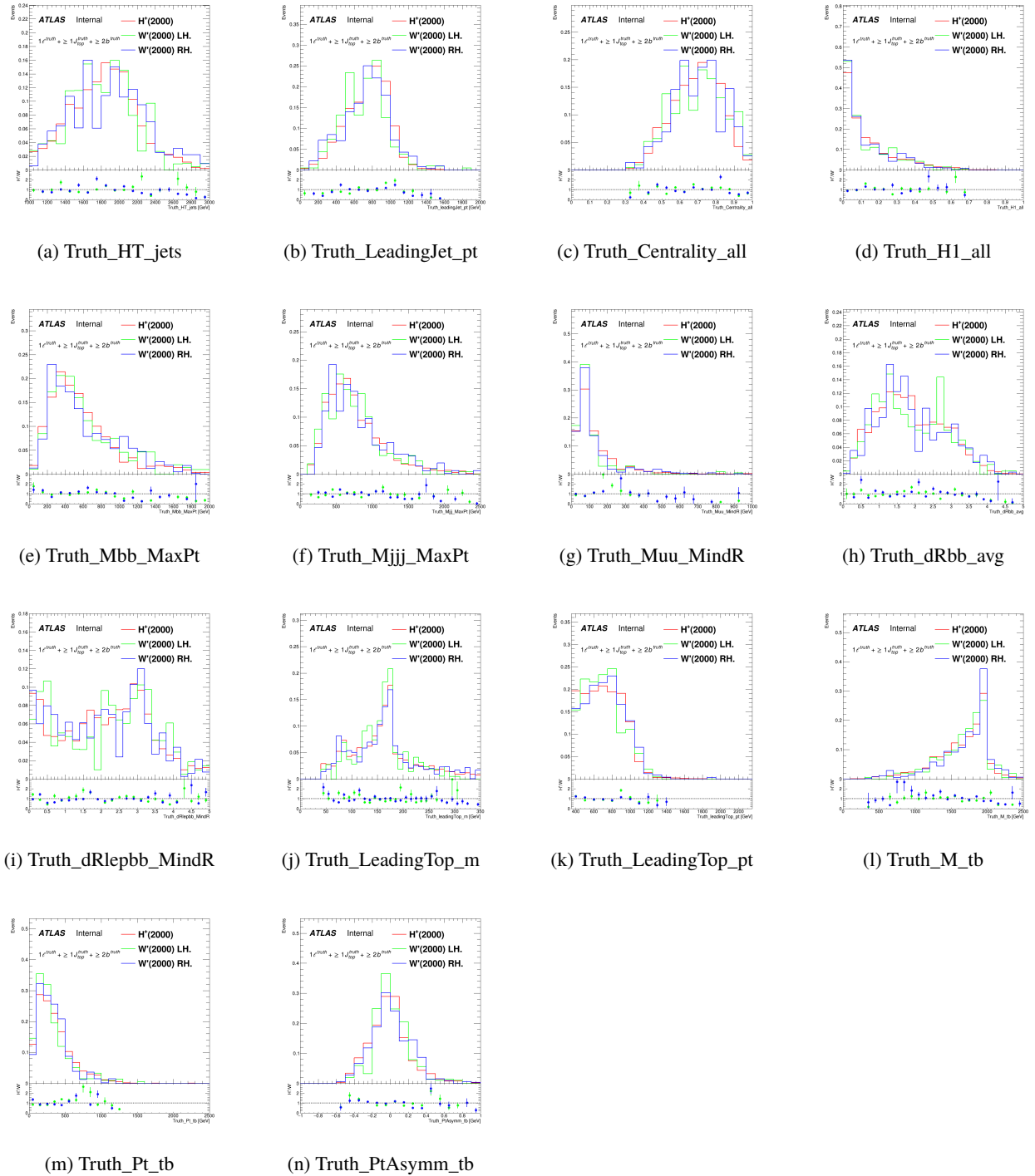


Figure 53: Comparison of the kinematic variables between tbW' and tbH^+ in truth level on 2000 GeV mass hypothesis.

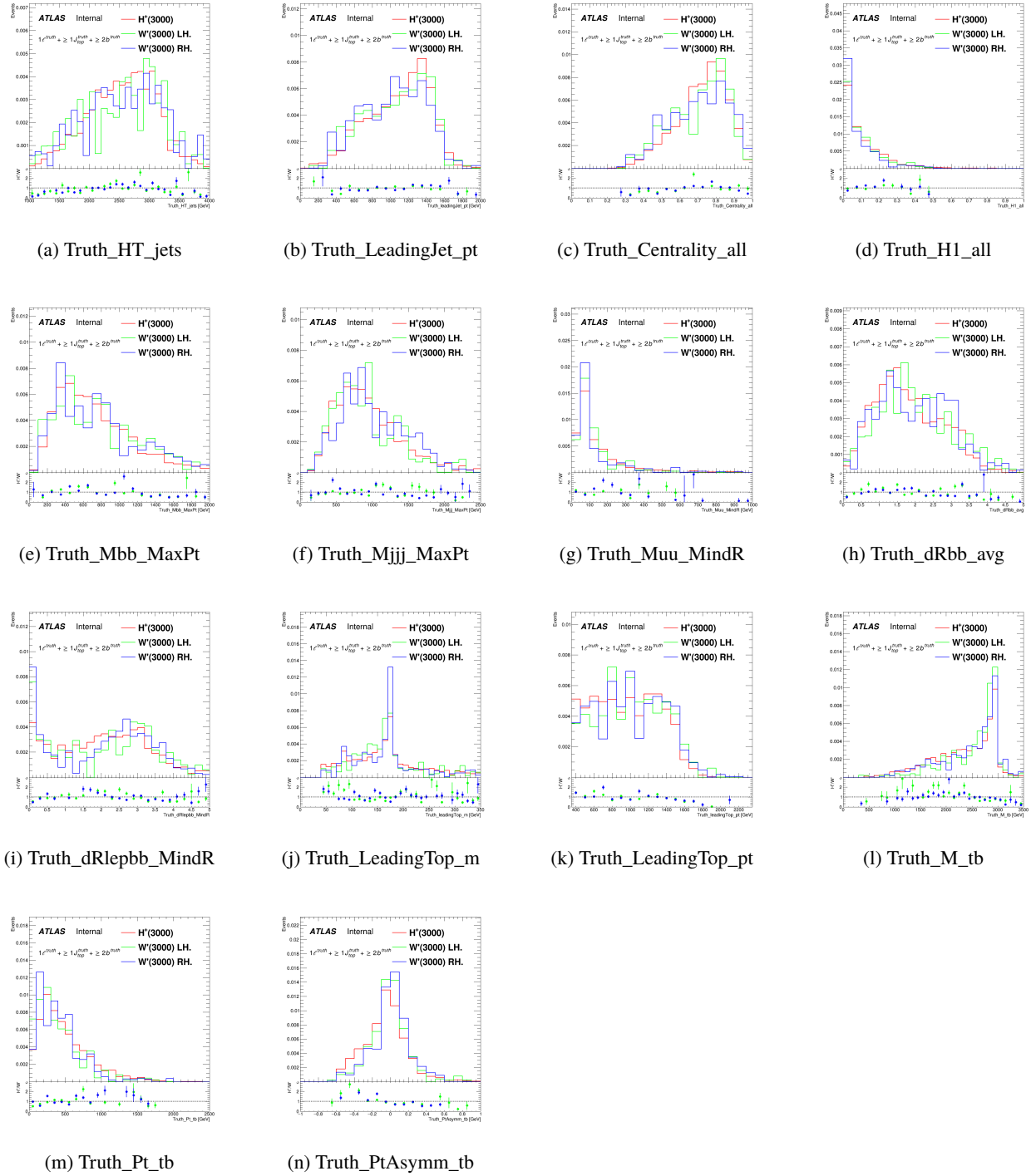


Figure 54: Comparison of the kinematic variables between tbW' and tbH^+ in truth level on 3000 GeV mass hypothesis.

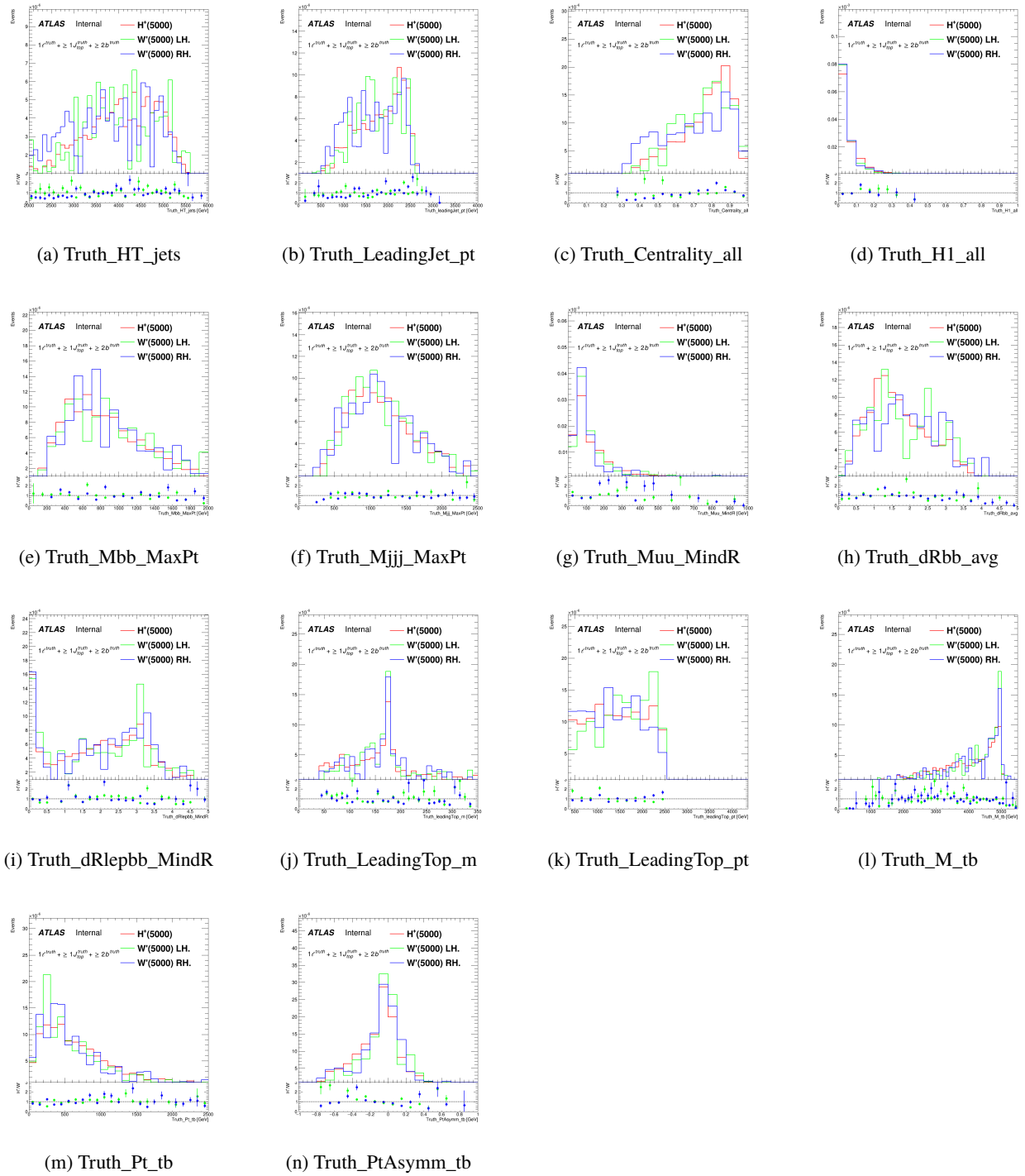


Figure 55: Comparison of the kinematic variables between tbW' and tbH^+ in truth level on 5000 GeV mass hypothesis.

760 **9 Summary and Conclusions**

761 We have performed a search for charged Higgs boson H^+ as well as W' bosons produced in association with
762 a top quark and a bottom quark, and decaying into a top quark and a bottom quark, in the lepton-plus-jets
763 final state, in the regime where the top quark from the parent boson is highly boosted to be reconstructed as
764 a top-tagged large- R jet. The mass range $1000 < m_{H^+} < 3000$ GeV is investigated. Expected upper cross
765 section limits between 0.073 pb and 0.011 pb were set.

766 **Limits for W' is to be finalized.**

767 References

- 768 [1] ATLAS Collaboration, *Observation of a new particle in the search for the Standard Model Higgs*
 769 *boson with the ATLAS detector at the LHC*, *Phys. Lett. B* **716** (2012) 1, arXiv: [1207.7214](#)
 770 [[hep-ex](#)] (cit. on p. 7).
- 771 [2] CMS Collaboration, *Observation of a new boson at a mass of 125 GeV with the CMS experiment*
 772 *at the LHC*, *Phys. Lett. B* **716** (2012) 30, arXiv: [1207.7235](#) [[hep-ex](#)] (cit. on p. 7).
- 773 [3] ATLAS and CMS Collaborations, *Combined Measurement of the Higgs Boson Mass in pp*
 774 *Collisions at $\sqrt{s} = 7$ and 8 TeV with the ATLAS and CMS Experiments*, *Phys. Rev. Lett.* **114**
 775 (2015) 191803, arXiv: [1503.07589](#) [[hep-ex](#)] (cit. on p. 7).
- 776 [4] T. D. Lee, *A Theory of Spontaneous T Violation*, *Phys. Rev. D* **8** (1973) (cit. on p. 7).
- 777 [5] G. Branco, P. Ferreira, L. Lavoura, M. Rebelo and M. Sher et al., *Theory and phenomenology of*
 778 *two-Higgs-doublet models*, *Phys. Rept.* **516** (2012), arXiv: [1106.0034](#) [[hep-ph](#)] (cit. on p. 7).
- 779 [6] K. Inoue, A. Kakuto, H. Komatsu and S. Takeshita, *Aspects of Grand Unified Models with Softly*
 780 *Broken Supersymmetry*, *Prog.Theor.Phys.* **68** (1982) (cit. on p. 7).
- 781 [7] T. Cheng and L.-F. Li, *Neutrino Masses, Mixings and Oscillations in $SU(2) \times U(1)$ Models of*
 782 *Electroweak Interactions*, *Phys. Rev. D* **22** (1980) (cit. on p. 7).
- 783 [8] J. Schechter and J. Valle, *Neutrino Masses in $SU(2) \times U(1)$ Theories*, *Phys. Rev. D* **22** (1980) (cit. on
 784 p. 7).
- 785 [9] G. Lazarides, Q. Shafi and C. Wetterich, *Proton Lifetime and Fermion Masses in an $SO(10)$ Model*,
 786 *Nucl. Phys. B* **181** (1981) (cit. on p. 7).
- 787 [10] R. Mohapatra and G. Senjanovic, *Neutrino Masses and Mixings in Gauge Models with Spontaneous*
 788 *Parity Violation*, *Phys. Rev. D* **23** (1981) (cit. on p. 7).
- 789 [11] M. Magg and C. Wetterich, *Neutrino Mass Problem and Gauge Hierarchy*, *Phys. Lett. B* **94** (1980)
 790 (cit. on p. 7).
- 791 [12] ATLAS Collaboration, *Search for charged Higgs bosons decaying via $H^\pm \rightarrow \tau\nu$ in $t\bar{t}$ events using*
 792 *pp collision data at $\sqrt{s} = 7$ TeV with the ATLAS detector*, *JHEP* **06** (2012) 039, arXiv: [1204.2760](#)
 793 [[hep-ex](#)] (cit. on p. 7).
- 794 [13] ATLAS Collaboration, *Search for charged Higgs bosons through the violation of lepton universality*
 795 *in $t\bar{t}$ events using pp collision data at $\sqrt{s} = 7$ TeV with the ATLAS experiment*, *JHEP* **03** (2013) 076,
 796 arXiv: [1212.3572](#) [[hep-ex](#)] (cit. on p. 7).
- 797 [14] ATLAS Collaboration, *Search for charged Higgs bosons decaying via $H^\pm \rightarrow \tau^\pm\nu$ in fully hadronic*
 798 *final states using pp collision data at $\sqrt{s} = 8$ TeV with the ATLAS detector*, *JHEP* **03** (2015) 088,
 799 arXiv: [1412.6663](#) [[hep-ex](#)] (cit. on p. 7).
- 800 [15] CMS Collaboration, *Search for a light charged Higgs boson in top quark decays in pp collisions at*
 801 *$\sqrt{s} = 7$ TeV*, *JHEP* **07** (2012) 143, arXiv: [1205.5736](#) [[hep-ex](#)] (cit. on p. 7).
- 802 [16] CMS Collaboration, *Search for a charged Higgs boson in pp collisions at $\sqrt{s} = 8$ TeV*, *JHEP* **11**
 803 (2015) 018, arXiv: [1508.07774](#) [[hep-ex](#)] (cit. on p. 7).
- 804 [17] ATLAS Collaboration, *Search for charged Higgs bosons decaying via $H^\pm \rightarrow \tau^\pm\nu_\tau$ in the $\tau+jets$*
 805 *and $\tau+lepton$ final states with 36fb^{-1} of pp collision data recorded at $\sqrt{s} = 13$ TeV with the ATLAS*
 806 *experiment*, *JHEP* **09** (2018) 139, arXiv: [1807.07915](#) [[hep-ex](#)] (cit. on p. 7).

- 807 [18] ATLAS Collaboration, *Search for a light charged Higgs boson in the decay channel $H^+ \rightarrow c\bar{s}$ in $t\bar{t}$*
 808 *events using pp collisions at $\sqrt{s} = 7\text{ TeV}$ with the ATLAS detector*, *Eur. Phys. J. C* **73** (2013) 2465,
 809 arXiv: [1302.3694 \[hep-ex\]](#) (cit. on p. 7).
- 810 [19] CMS Collaboration, *Search for a light charged Higgs boson decaying to $c\bar{s}$ in pp collisions at*
 811 *$\sqrt{s} = 8\text{ TeV}$* , *JHEP* **12** (2015) 178, arXiv: [1510.04252 \[hep-ex\]](#) (cit. on p. 7).
- 812 [20] CMS Collaboration, *Search for a charged Higgs boson decaying to charm and bottom quarks*
 813 *in proton–proton collisions at $\sqrt{s} = 8\text{ TeV}$* , *JHEP* **11** (2018) 115, arXiv: [1808.06575 \[hep-ex\]](#)
 814 (cit. on p. 7).
- 815 [21] ATLAS Collaboration, *Search for charged Higgs bosons in the $H^\pm \rightarrow tb$ decay channel in pp*
 816 *collisions at $\sqrt{s} = 8\text{ TeV}$ using the ATLAS detector*, *JHEP* **03** (2016) 127, arXiv: [1512.03704 \[hep-ex\]](#)
 817 (cit. on p. 7).
- 818 [22] ATLAS Collaboration, *Search for charged Higgs bosons produced in association with a top quark*
 819 *and decaying via $H^\pm \rightarrow \tau\nu$ using pp collision data recorded at $\sqrt{s} = 13\text{ TeV}$ by the ATLAS detector*,
 820 *Phys. Lett. B* **759** (2016) 555, arXiv: [1603.09203 \[hep-ex\]](#) (cit. on p. 7).
- 821 [23] ATLAS Collaboration, *Search for charged Higgs bosons decaying into top and bottom quarks*
 822 *at $\sqrt{s} = 13\text{ TeV}$ with the ATLAS detector*, *JHEP* **11** (2018) 085, arXiv: [1808.03599 \[hep-ex\]](#)
 823 (cit. on pp. 7, 41).
- 824 [24] ATLAS Collaboration, *Search for a charged Higgs bosons decaying into a top-quark and a*
 825 *bottom-quark at $\sqrt{s} = 13\text{ TeV}$ with the ATLAS detector*, *JHEP* **16** (2021) 145, arXiv: [2102.10076 \[hep-ex\]](#)
 826 (cit. on pp. 7, 30, 68).
- 827 [25] CMS Collaboration, *Search for a charged Higgs boson decaying into top and bottom quarks in*
 828 *events with electrons or muons in proton–proton collisions at $\sqrt{s} = 13\text{ TeV}$* , *JHEP* **01** (2020) 096,
 829 arXiv: [1908.09206 \[hep-ex\]](#) (cit. on p. 7).
- 830 [26] CMS Collaboration, *Search for charged Higgs bosons decaying into a top and a bottom quark*
 831 *in the all-jet final state of pp collisions at $\sqrt{s} = 13\text{ TeV}$* , (2020), arXiv: [2001.07763 \[hep-ex\]](#)
 832 (cit. on p. 7).
- 833 [27] ATLAS Collaboration, *Search for dijet resonances in events with an isolated charged lepton using*
 834 *$\sqrt{s} = 13\text{ TeV}$ proton–proton collision data collected by the ATLAS detector*, *JHEP* **06** (2020) 151,
 835 arXiv: [2002.11325 \[hep-ex\]](#) (cit. on p. 7).
- 836 [28] ATLAS Collaboration, *Search for a Charged Higgs Boson Produced in the Vector-Boson Fusion*
 837 *Mode with Decay $H^\pm \rightarrow W^\pm Z$ using pp Collisions at $\sqrt{s} = 8\text{ TeV}$ with the ATLAS Experiment*,
 838 *Phys. Rev. Lett.* **114** (2015) 231801, arXiv: [1503.04233 \[hep-ex\]](#) (cit. on p. 7).
- 839 [29] CMS Collaboration, *Search for charged Higgs bosons produced via vector boson fusion and*
 840 *decaying into a pair of W and Z bosons using pp collisions at $\sqrt{s} = 13\text{ TeV}$* , *Phys. Rev. Lett.* **119**
 841 (2017) 141802, arXiv: [1705.02942 \[hep-ex\]](#) (cit. on p. 7).
- 842 [30] ATLAS Collaboration, *Luminosity determination in pp collisions at $\sqrt{s} = 13\text{ TeV}$ using the ATLAS*
 843 *detector at the LHC*, ATLAS-CONF-2019-021, 2019, URL: <https://cds.cern.ch/record/2677054> (cit. on pp. 8, 37).
- 845 [31] *LuminosityForPhysics* twiki page, URL: <https://twiki.cern.ch/twiki/bin/viewauth/Atlas/LuminosityForPhysics> (cit. on p. 8).
- 846 [32] *Web directory for GoodRunsLists in atlas-groupdata area*, URL: <https://atlas-groupdata.web.cern.ch/atlas-groupdata/GoodRunsLists> (cit. on p. 8).

- 849 [33] C. Degrande, M. Ubiali, M. Wiesemann and M. Zaro, *Heavy charged Higgs boson production at*
 850 *the LHC*, JHEP **10** (2015) 145, arXiv: [1507.02549 \[hep-ph\]](#) (cit. on pp. 8, 9).
- 851 [34] J. Alwall et al., *The automated computation of tree-level and next-to-leading order differential*
 852 *cross sections, and their matching to parton shower simulations*, JHEP **07** (2014) 079, arXiv:
 853 [1405.0301 \[hep-ph\]](#) (cit. on pp. 8, 44).
- 854 [35] R. D. Ball et al., *Parton distributions with LHC data*, Nucl. Phys. B **867** (2013) 244, arXiv:
 855 [1207.1303 \[hep-ph\]](#) (cit. on p. 8).
- 856 [36] R. D. Ball et al., *Parton distributions for the LHC run II*, JHEP **04** (2015) 040, arXiv: [1410.8849](#)
 857 [\[hep-ph\]](#) (cit. on pp. 8, 9).
- 858 [37] T. Sjöstrand, S. Mrenna and P. Skands, *A brief introduction to PYTHIA 8.1*, Comput. Phys. Commun.
 859 **178** (2008) 852, arXiv: [0710.3820 \[hep-ph\]](#) (cit. on p. 8).
- 860 [38] ATLAS Collaboration, *ATLAS Pythia 8 tunes to 7 TeV data*, ATL-PHYS-PUB-2014-021, 2014,
 861 URL: <https://cds.cern.ch/record/1966419> (cit. on pp. 8, 42).
- 862 [39] M. Flechl, M. Klees, M. Krämer, M. Spira and M. Ubiali, *Improved cross-section predictions*
 863 *for heavy charged Higgs boson production at the LHC*, Physical Review D **91** (2015), URL:
 864 <http://dx.doi.org/10.1103/PhysRevD.91.075015>, ISSN:1550-2368 (cit. on p. 9).
- 865 [40] S. Dittmaier, M. Krämer, M. Spira and M. Walser, *Charged-Higgs-boson production at the*
 866 *LHC:Next-to-leading-order supersymmetric QCD corrections*, Physical Review D **83** (2011), URL:
 867 <http://dx.doi.org/10.1103/PhysRevD.83.055005>, ISSN:1550-2368 (cit. on p. 9).
- 868 [41] E. Berger, T. Han, J. Jiang and T. Plehn, *Associated production of a top quark and a charged*
 869 *Higgs boson*, Physical Review D **71** (2005), URL: <http://dx.doi.org/10.1103/PhysRevD.71.115012>, ISSN:1550-2368 (cit. on p. 9).
- 871 [42] P. Nason, *A new method for combining NLO QCD with shower Monte Carlo algorithms*, JHEP **11**
 872 (2004) 040, arXiv: [hep-ph/0409146](#) (cit. on p. 9).
- 873 [43] S. Frixione, P. Nason and C. Oleari, *Matching NLO QCD computations with parton shower*
 874 *simulations: the POWHEG method*, JHEP **11** (2007) 070, arXiv: [0709.2092 \[hep-ph\]](#) (cit. on
 875 p. 9).
- 876 [44] S. Alioli, P. Nason, C. Oleari and E. Re, *A general framework for implementing NLO calculations*
 877 *in shower Monte Carlo programs: the POWHEG BOX*, JHEP **06** (2010) 043, arXiv: [1002.2581](#)
 878 [\[hep-ph\]](#) (cit. on p. 9).
- 879 [45] J. Campbell, R. Ellis, P. Nason and E. Re, *Top-pair production and decay at NLO matched with*
 880 *parton showers*, JHEP **04** (2015), arXiv: [1412.1828 \[hep-ph\]](#) (cit. on p. 9).
- 881 [46] ATLAS Collaboration, *Studies on top-quark Monte Carlo modelling for Top2016*, ATL-PHYS-
 882 PUB-2016-020, 2016, URL: <https://cds.cern.ch/record/2216168> (cit. on pp. 9, 11).
- 883 [47] T. Sjöstrand et al., *An introduction to PYTHIA 8.2*, Comput. Phys. Commun. **191** (2015) 159, arXiv:
 884 [1410.3012 \[hep-ph\]](#) (cit. on p. 9).
- 885 [48] M. Bahr et al., *Herwig++ physics and manual*, Eur. Phys. J. C **58** (2008) 639, arXiv: [0803.0883](#)
 886 [\[hep-ph\]](#) (cit. on p. 9).
- 887 [49] J. Bellm et al., *Herwig 7.0/Herwig++ 3.0 release note*, Eur. Phys. J. C **76** (2016) 196, arXiv:
 888 [1512.01178 \[hep-ph\]](#) (cit. on p. 9).

- [50] ATLAS Collaboration, *Studies on top-quark Monte Carlo modelling with Sherpa and MG5_aMC@NLO*, ATL-PHYS-PUB-2017-007, 2017, URL: <https://cds.cern.ch/record/2261938> (cit. on p. 10).
- [51] H. B. Hartanto, B. Jäger, L. Reina and D. Wackerlo, *Higgs boson production in association with top quarks in the POWHEG BOX*, Phys. Rev. D **91** (2015) 094003, arXiv: [1501.04498 \[hep-ph\]](https://arxiv.org/abs/1501.04498) (cit. on p. 10).
- [52] E. Bothmann et al., *Event Generation with Sherpa 2.2*, SciPost Phys. **7** (2019) 034, arXiv: [1905.09127 \[hep-ph\]](https://arxiv.org/abs/1905.09127) (cit. on p. 10).
- [53] S. Catani, F. Krauss, R. Kuhn and B. R. Webber, *QCD Matrix Elements + Parton Showers*, JHEP **11** (2001) 063, arXiv: [hep-ph/0109231](https://arxiv.org/abs/hep-ph/0109231) (cit. on pp. 10, 13).
- [54] S. Höche, F. Krauss, S. Schumann and F. Siegert, *QCD matrix elements and truncated showers*, JHEP **05** (2009) 053, arXiv: [0903.1219 \[hep-ph\]](https://arxiv.org/abs/0903.1219) (cit. on pp. 10, 13).
- [55] R. Frederix, E. Re and P. Torrielli, *Single-top t-channel hadroproduction in the four-flavour scheme with POWHEG and aMC@NLO*, JHEP **09** (2012) 130, arXiv: [1207.5391 \[hep-ph\]](https://arxiv.org/abs/1207.5391) (cit. on pp. 11, 12).
- [56] S. Frixione, E. Laenen, P. Motylinski and B. R. Webber, *Angular correlations of lepton pairs from vector boson and top quark decays in Monte Carlo simulations*, JHEP **04** (2007) 081, arXiv: [hep-ph/0702198](https://arxiv.org/abs/hep-ph/0702198) (cit. on p. 11).
- [57] P. Artoisenet, R. Frederix, O. Mattelaer and R. Rietkerk, *Automatic spin-entangled decays of heavy resonances in Monte Carlo simulations*, JHEP **03** (2013) 015, arXiv: [1212.3460 \[hep-ph\]](https://arxiv.org/abs/1212.3460) (cit. on p. 11).
- [58] S. Frixione, E. Laenen, P. Motylinski, C. D. White and B. R. Webber, *Single-top hadroproduction in association with a W boson*, JHEP **07** (2008) 029, arXiv: [0805.3067 \[hep-ph\]](https://arxiv.org/abs/0805.3067) (cit. on pp. 11, 12, 43).
- [59] ATLAS Collaboration, *Measurement of the production cross-section of a single top quark in association with a Z boson in proton–proton collisions at 13 TeV with the ATLAS detector*, Phys. Lett. B **780** (2018) 557, arXiv: [1710.03659 \[hep-ex\]](https://arxiv.org/abs/1710.03659) (cit. on p. 12).
- [60] J. Pumplin et al., *New Generation of Parton Distributions with Uncertainties from Global QCD Analysis*, JHEP **07** (2002) 012, arXiv: [hep-ph/0201195](https://arxiv.org/abs/hep-ph/0201195) (cit. on p. 12).
- [61] R. Frederix, D. Pagani and M. Zaro, *Large NLO corrections in $t\bar{t}W^\pm$ and $t\bar{t}t\bar{t}$ hadroproduction from supposedly subleading EW contributions*, JHEP **02** (2018) 031, arXiv: [1711.02116 \[hep-ph\]](https://arxiv.org/abs/1711.02116) (cit. on p. 12).
- [62] T. Gleisberg and S. Höche, *Comix, a new matrix element generator*, JHEP **12** (2008) 039, arXiv: [0808.3674 \[hep-ph\]](https://arxiv.org/abs/0808.3674) (cit. on p. 13).
- [63] F. Cascioli, P. Maierhöfer and S. Pozzorini, *Scattering Amplitudes with Open Loops*, Phys. Rev. Lett. **108** (2012) 111601, arXiv: [1111.5206 \[hep-ph\]](https://arxiv.org/abs/1111.5206) (cit. on p. 13).
- [64] A. Denner, S. Dittmaier and L. Hofer, *Collier: A fortran-based complex one-loop library in extended regularizations*, Comput. Phys. Commun. **212** (2017) 220, arXiv: [1604.06792 \[hep-ph\]](https://arxiv.org/abs/1604.06792) (cit. on p. 13).
- [65] S. Schumann and F. Krauss, *A parton shower algorithm based on Catani–Seymour dipole factorisation*, JHEP **03** (2008) 038, arXiv: [0709.1027 \[hep-ph\]](https://arxiv.org/abs/0709.1027) (cit. on p. 13).

- [66] J.-C. Winter, F. Krauss and G. Soff, *A modified cluster-hadronization model*, *Eur. Phys. J. C* **36** (2004) 381, arXiv: [hep-ph/0311085](#) (cit. on p. 13).
- [67] S. Höche, F. Krauss, M. Schönherr and F. Siegert, *A critical appraisal of NLO+PS matching methods*, *JHEP* **09** (2012) 049, arXiv: [1111.1220 \[hep-ph\]](#) (cit. on p. 13).
- [68] S. Höche, F. Krauss, M. Schönherr and F. Siegert, *QCD matrix elements + parton showers. The NLO case*, *JHEP* **04** (2013) 027, arXiv: [1207.5030 \[hep-ph\]](#) (cit. on p. 13).
- [69] E. Bothmann, M. Schönherr and S. Schumann, *Reweighting QCD matrix-element and parton-shower calculations*, *Eur. Phys. J. C* **76** (2016) 590, arXiv: [1606.08753 \[hep-ph\]](#) (cit. on p. 13).
- [70] ATLAS Collaboration, *Electron reconstruction and identification efficiency measurements with the ATLAS detector using the 2011 LHC proton–proton collision data*, *Eur. Phys. J. C* **74** (2014) 2941, arXiv: [1404.2240 \[hep-ex\]](#) (cit. on p. 15).
- [71] ATLAS Collaboration, *Electron efficiency measurements with the ATLAS detector using the 2015 LHC proton–proton collision data*, ATLAS-CONF-2016-024, 2016, URL: <https://cds.cern.ch/record/2157687> (cit. on p. 15).
- [72] *Lepton isolation recommendations*, URL: <https://twiki.cern.ch/twiki/bin/viewauth/AtlasProtected/IsolationSelectionTool> (cit. on p. 15).
- [73] ATLAS Collaboration, *Muon reconstruction performance of the ATLAS detector in proton–proton collision data at $\sqrt{s} = 13\text{ TeV}$* , *Eur. Phys. J. C* **76** (2016) 292, arXiv: [1603.05598 \[hep-ex\]](#) (cit. on pp. 15, 37, 39).
- [74] ATLAS Collaboration, *Reconstruction, Energy Calibration, and Identification of Hadronically Decaying Tau Leptons in the ATLAS Experiment for Run-2 of the LHC*, ATL-PHYS-PUB-2015-045, 2015, URL: <https://cds.cern.ch/record/2064383> (cit. on p. 15).
- [75] M. Cacciari, G. P. Salam and G. Soyez, *The anti- k_t jet clustering algorithm*, *JHEP* **04** (2008) 063, arXiv: [0802.1189 \[hep-ph\]](#) (cit. on p. 15).
- [76] ATLAS Collaboration, *Jet reconstruction and performance using particle flow with the ATLAS Detector*, *Eur. Phys. J. C* **77** (2017) 466, arXiv: [1703.10485 \[hep-ex\]](#) (cit. on p. 15).
- [77] ATLAS Collaboration, *Jet energy scale and resolution measured in proton–proton collisions at $\sqrt{s} = 13\text{ TeV}$ with the ATLAS detector*, (2020), arXiv: [2007.02645 \[hep-ex\]](#) (cit. on p. 15).
- [78] ATLAS Collaboration, *Performance of pile-up mitigation techniques for jets in pp collisions at $\sqrt{s} = 8\text{ TeV}$ using the ATLAS detector*, *Eur. Phys. J. C* **76** (2016) 581, arXiv: [1510.03823 \[hep-ex\]](#) (cit. on pp. 15, 39).
- [79] ATLAS Collaboration, *ATLAS b-jet identification performance and efficiency measurement with $t\bar{t}$ events in pp collisions at $\sqrt{s} = 13\text{ TeV}$* , *Eur. Phys. J. C* **79** (2019) 970, arXiv: [1907.05120 \[hep-ex\]](#) (cit. on pp. 15, 40).
- [80] ATLAS Collaboration, *Topological cell clustering in the ATLAS calorimeters and its performance in LHC Run 1*, *Eur. Phys. J. C* **77** (2017) 490, arXiv: [1603.02934 \[hep-ex\]](#) (cit. on p. 16).
- [81] D. Krohn, J. Thaler and L.-T. Wang, *Jet trimming*, *Journal of High Energy Physics* **2010** (2010) 84, URL: [https://link.springer.com/article/10.1007/JHEP02\(2010\)084](https://link.springer.com/article/10.1007/JHEP02(2010)084), ISSN:1029-8479 (cit. on p. 16).

- [82] S. Catani, Y. Dokshitzer, M. Seymour and B. Webber, *Longitudinally invariant K(t) clustering algorithms for hadron-hadron collisions*, Nuclear Physics B **406** (1993) 187, URL: <https://www.sciencedirect.com/science/article/pii/055032139390166M>, ISSN:0550-3213 (cit. on p. 16).
- [83] ATLAS Collaboration, *Identification of boosted, hadronically decaying W bosons and comparisons with ATLAS data taken at $\sqrt{s} = 8$ TeV*, Eur. Phys. J. C **76** (2016) 154, arXiv: [1510.05821 \[hep-ex\]](https://arxiv.org/abs/1510.05821) (cit. on p. 16).
- [84] ATLAS Collaboration, *Jet mass reconstruction with the ATLAS Detector in early Run 2 data*, ATLAS-CONF-2016-035, 2016, URL: <https://cds.cern.ch/record/2200211> (cit. on p. 16).
- [85] ATLAS Collaboration, *Boosted hadronic vector boson and top quark tagging with ATLAS using Run 2 data*, ATL-PHYS-PUB-2020-017, 2020, URL: <https://cds.cern.ch/record/2724149> (cit. on pp. 16, 41).
- [86] J. Thaler and K. Van Tilburg, *Identifying Boosted Objects with N-subjettiness*, JHEP **03** (2011) 015, arXiv: [1011.2268 \[hep-ph\]](https://arxiv.org/abs/1011.2268) (cit. on p. 16).
- [87] J. Thaler and L.-T. Wang, *Strategies to Identify Boosted Tops*, JHEP **07** (2008) 092, arXiv: [0806.0023 \[hep-ph\]](https://arxiv.org/abs/0806.0023) (cit. on p. 16).
- [88] A. Larkoski, G. Salam and J. Thaler, *Energy Correlation Functions for Jet Substructure*, JHEP **06** (2013) 108, arXiv: [1305.0007 \[hep-ph\]](https://arxiv.org/abs/1305.0007) (cit. on p. 16).
- [89] D. Adams and et al., *Recommendations of the Physics Objects and Analysis Harmonisation Study Groups 2014*, ATL-PHYS-INT-2014-018, 2014, URL: <https://cds.cern.ch/record/1743654> (cit. on p. 16).
- [90] *Documentation of the ATLAS AssociationUtils package*, URL: <https://gitlab.cern.ch/atlas/athena/blob/release/21.2.86/PhysicsAnalysis/AnalysisCommon/AssociationUtils/README.rst> (cit. on p. 16).
- [91] J. Gallicchio and Y.-T. Chien, *Quit Using Pseudorapidity, Transverse Energy, and Massless Constituents*, 2018, arXiv: [1802.05356 \[hep-ph\]](https://arxiv.org/abs/1802.05356) (cit. on p. 16).
- [92] G. Avoni and et al., *The new LUCID-2 detector for luminosity measurement and monitoring in ATLAS*, JINST **13** (2018) P07017 (cit. on p. 37).
- [93] ATLAS Collaboration, *Measurement of the Inelastic Proton–Proton Cross Section at $\sqrt{s} = 13$ TeV with the ATLAS Detector at the LHC*, Phys. Rev. Lett. **117** (2016) 182002, arXiv: [1606.02625 \[hep-ex\]](https://arxiv.org/abs/1606.02625) (cit. on p. 37).
- [94] ATLAS Collaboration, *Electron reconstruction and identification in the ATLAS experiment using the 2015 and 2016 LHC proton–proton collision data at $\sqrt{s} = 13$ TeV*, Eur. Phys. J. C **79** (2019) 639, arXiv: [1902.04655 \[hep-ex\]](https://arxiv.org/abs/1902.04655) (cit. on p. 37).
- [95] ATLAS Collaboration, *Electron and photon performance measurements with the ATLAS detector using the 2015–2017 LHC proton–proton collision data*, JINST **14** (2019) P12006, arXiv: [1908.00005 \[hep-ex\]](https://arxiv.org/abs/1908.00005) (cit. on p. 39).
- [96] ATLAS Collaboration, *Jet energy scale measurements and their systematic uncertainties in proton–proton collisions at $\sqrt{s} = 13$ TeV with the ATLAS detector*, Phys. Rev. D **96** (2017) 072002, arXiv: [1703.09665 \[hep-ex\]](https://arxiv.org/abs/1703.09665) (cit. on p. 39).
- [97] ATLAS Collaboration, *Determination of jet calibration and energy resolution in proton–proton collisions at $\sqrt{s} = 8$ TeV using the ATLAS detector*, (2019), arXiv: [1910.04482 \[hep-ex\]](https://arxiv.org/abs/1910.04482) (cit. on p. 39).

- 1013 [98] ATLAS Collaboration, *In situ calibration of large-radius jet energy and mass in 13 TeV proton–
1014 proton collisions with the ATLAS detector*, *Eur. Phys. J. C* **79** (2019) 135, arXiv: [1807.09477](#)
1015 [[hep-ex](#)] (cit. on pp. 39, 40).
- 1016 [99] ATLAS Collaboration, *Measurement of the ATLAS Detector Jet Mass Response using Forward
1017 Folding with 80fb^{-1} of $\sqrt{s} = 13\text{ TeV}$ pp data*, ATLAS-CONF-2020-022, 2020, URL: <https://cds.cern.ch/record/2724442> (cit. on p. 40).
- 1019 [100] ATLAS Collaboration, *Measurement of b-tagging efficiency of c-jets in $t\bar{t}$ events using a likelihood
1020 approach with the ATLAS detector*, ATLAS-CONF-2018-001, 2018, URL: <https://cds.cern.ch/record/2306649> (cit. on p. 40).
- 1022 [101] ATLAS Collaboration, *Calibration of light-flavour b-jet mistagging rates using ATLAS proton–
1023 proton collision data at $\sqrt{s} = 13\text{ TeV}$* , ATLAS-CONF-2018-006, 2018, URL: <https://cds.cern.ch/record/2314418> (cit. on p. 40).
- 1025 [102] ATLAS Collaboration, *Performance of top-quark and W-boson tagging with ATLAS in Run 2 of
1026 the LHC*, *Eur. Phys. J. C* **79** (2019) 375, arXiv: [1808.07858](#) [[hep-ex](#)] (cit. on p. 41).
- 1027 [103] J. Butterworth et al., *PDF4LHC recommendations for LHC Run II*, *J. Phys. G* **43** (2016) 023001,
1028 arXiv: [1510.03865](#) [[hep-ph](#)] (cit. on p. 41).
- 1029 [104] D. de Florian et al., *Handbook of LHC Higgs Cross Sections: 4. Deciphering the Nature of the
1030 Higgs Sector*, (2016), arXiv: [1610.07922](#) [[hep-ph](#)] (cit. on p. 43).
- 1031 [105] R. Raitio and W. W. Wada, *Higgs Boson Production at Large Transverse Momentum in QCD*, *Phys.
1032 Rev. D* **19** (1979) (cit. on p. 43).
- 1033 [106] W. Beenakker and et al., *NLO QCD corrections to t anti-t H production in hadron collisions*, *Nucl.
1034 Phys. B* **653** (2003), arXiv: [hep-ph/0211352](#) [[hep-ph](#)] (cit. on p. 43).
- 1035 [107] S. Dawson, C. Jackson, L. H. Orr, L. Reina and D. Wackerlo, *Associated Higgs production with
1036 top quarks at the large hadron collider: NLO QCD corrections*, *Phys. Rev. D* **68** (2003), arXiv:
1037 [hep-ph/0305087](#) [[hep-ph](#)] (cit. on p. 43).
- 1038 [108] Y. Zhang, W.-G. Ma, R.-Y. Zhang, C. Chen and L. Guo, *QCD NLO and EW NLO corrections to $t\bar{t}H$
1039 production with top quark decays at hadron collider*, *Phys. Lett. B* **738** (2014), arXiv: [1407.1110](#)
1040 [[hep-ph](#)] (cit. on p. 43).
- 1041 [109] S. Frixione, V. Hirschi, D. Pagani, H.-S. Shao and M. Zaro, *Electroweak and QCD corrections to
1042 top-pair hadroproduction in association with heavy bosons*, *JHEP* **06** (2015), arXiv: [1504.03446](#)
1043 [[hep-ph](#)] (cit. on p. 43).
- 1044 [110] LHCTopWG, *NLO single-top channel cross sections*, 2017, URL: <https://twiki.cern.ch/twiki/bin/view/LHCPhysics/SingleTopRefXsec> (cit. on p. 43).
- 1046 [111] A. D. Martin, W. J. Stirling, R. S. Thorne and G. Watt, *Parton distributions for the LHC*, *Eur. Phys.
1047 J. C* **63** (2009) 189, arXiv: [0901.0002](#) [[hep-ph](#)] (cit. on p. 43).
- 1048 [112] A. D. Martin, W. Stirling, R. Thorne and G. Watt, *Uncertainties on α_S in global PDF analyses
1049 and implications for predicted hadronic cross sections*, *Eur. Phys. J. C* **64** (2009) 653, arXiv:
1050 [0905.3531](#) [[hep-ph](#)] (cit. on p. 43).
- 1051 [113] M. Aliev et al., *HATHOR – HArdonic Top and Heavy quarks crOss section calculatoR*, *Comput.
1052 Phys. Commun.* **182** (2011) 1034, arXiv: [1007.1327](#) [[hep-ph](#)] (cit. on p. 43).

- 1053 [114] P. Kant et al., *HatHor for single top-quark production: Updated predictions and uncertainty*
1054 *estimates for single top-quark production in hadronic collisions*, Comput. Phys. Commun. **191**
1055 (2015) 74, arXiv: [1406.4403 \[hep-ph\]](https://arxiv.org/abs/1406.4403) (cit. on p. 43).
- 1056 [115] LHCHXSWG1, *Recommended predictions for $t\bar{t}V$ cross sections*, URL: https://twiki.cern.ch/twiki/bin/view/LHCPhysics/LHCHXSWGTT#Plans_for_YR4 (cit. on p. 43).
- 1058 [116] J. M. Campbell and R. K. Ellis, *$t\bar{t}W^{+-}$ production and decay at NLO*, JHEP **07** (2012), arXiv:
1059 [1204.5678 \[hep-ph\]](https://arxiv.org/abs/1204.5678) (cit. on p. 43).
- 1060 [117] ATLAS PMG Top processes twiki page, URL: <https://twiki.cern.ch/twiki/bin/view/AtlasProtected/PmgTopProcesses> (cit. on p. 44).
- 1062 [118] ATLAS Collaboration, *Multi-boson simulation for 13 TeV ATLAS analyses*, ATL-PHYS-PUB-
1063 2016-002, 2016, URL: <https://cds.cern.ch/record/2119986> (cit. on p. 44).
- 1064 [119] *Automatic binning implematation in TTHFitter*. URL: https://indico.cern.ch/event/455289/contributions/1953694/attachments/1209081/1762963/Calvet_binning_Htop_160108.pdf (cit. on p. 45).
- 1067 [120] PhysicsModellingGroup, *TruthDAOD*, URL: <https://twiki.cern.ch/twiki/bin/view/AtlasProtected/TruthDAOD> (cit. on p. 69).
- 1069 [121] W. Bell et al., *Proposal for truth particle observable definitions*, (), URL: <https://cds.cern.ch/record/1700541> (cit. on p. 69).

1071 Appendices

1072 A TOPQ1 DAOD list

1073 A.1 Data

1074 Table 19 is the TOPQ1 DAOD list for data sample in this analysis.

data15_13TeV.AllYear.physics_Main.PhysCont.DAOD_TOPQ1.grp15_v01_p4513
data16_13TeV.AllYear.physics_Main.PhysCont.DAOD_TOPQ1.grp16_v01_p4513
data17_13TeV.AllYear.physics_Main.PhysCont.DAOD_TOPQ1.grp17_v01_p4513
data18_13TeV.AllYear.physics_Main.PhysCont.DAOD_TOPQ1.grp18_v01_p4513

1075 Table 19: TOPQ1 DAOD list for data sample in this analysis.

1075 A.2 $t\bar{t}H^+$

1076 Table 20 is the TOPQ1 DAOD list for H^+ sample in this analysis.

Nominal
mc16_13TeV.450004.aMcAtNloPythia8EvtGen_A14NNPDF23LO_Hplus4FS_H1000_tb.deriv.DAOD_TOPQ1.e7137_s3126_r9364_p4514
mc16_13TeV.450598.aMcAtNloPythia8EvtGen_A14NNPDF23LO_Hplus4FS_H1200_tb.deriv.DAOD_TOPQ1.e7429_s3126_r9364_p4514
mc16_13TeV.450599.aMcAtNloPythia8EvtGen_A14NNPDF23LO_Hplus4FS_H1400_tb.deriv.DAOD_TOPQ1.e7429_s3126_r9364_p4514
mc16_13TeV.450600.aMcAtNloPythia8EvtGen_A14NNPDF23LO_Hplus4FS_H1600_tb.deriv.DAOD_TOPQ1.e7429_s3126_r9364_p4514
mc16_13TeV.450601.aMcAtNloPythia8EvtGen_A14NNPDF23LO_Hplus4FS_H1800_tb.deriv.DAOD_TOPQ1.e7429_s3126_r9364_p4514
mc16_13TeV.450602.aMcAtNloPythia8EvtGen_A14NNPDF23LO_Hplus4FS_H2000_tb.deriv.DAOD_TOPQ1.e7429_s3126_r9364_p4514
mc16_13TeV.451490.aMcAtNloPythia8EvtGen_A14NNPDF23LO_Hplus4FS_H2500_tb.deriv.DAOD_TOPQ1.e7970_s3126_r9364_p4514
mc16_13TeV.451491.aMcAtNloPythia8EvtGen_A14NNPDF23LO_Hplus4FS_H3000_tb.deriv.DAOD_TOPQ1.e7970_s3126_r9364_p4514
mc16_13TeV.508710.MGPy8EG_A14NNPDF30_Hplus4FS_H4000_tb.deriv.DAOD_TOPQ1.e8276_s3126_r9364_p4514
mc16_13TeV.508711.MGPy8EG_A14NNPDF30_Hplus4FS_H5000_tb.deriv.DAOD_TOPQ1.e8276_s3126_r9364_p4514

1077 Table 20: TOPQ1 DAOD list for H^+ sample in this analysis.

1077 A.3 $t\bar{t} + \text{jets}$

1078 Table 21 is the TOPQ1 DAOD list for $t\bar{t} + \text{jets}$ sample in this analysis.

Nominal
mc16_13TeV.410470.PhPy8EG_A14_ttbar_hdamp258p75_nonallhad.deriv.DAOD_TOPQ1.e6337_s3126_r9364_p4514
mc16_13TeV.410471.PhPy8EG_A14_ttbar_hdamp258p75_allhad.deriv.DAOD_TOPQ1.e6337_s3126_r9364_p4514
mc16_13TeV.411073.PhPy8EG_A14_ttbar_hdamp258p75_ljets_BBFilt.deriv.DAOD_TOPQ1.e6798_s3126_r9364_p4514
mc16_13TeV.411074.PhPy8EG_A14_ttbar_hdamp258p75_ljets_BFiltBBVeto.deriv.DAOD_TOPQ1.e6798_s3126_r9364_p4514
mc16_13TeV.411075.PhPy8EG_A14_ttbar_hdamp258p75_ljets_CFiltBVeto.deriv.DAOD_TOPQ1.e6798_s3126_r9364_p4514
mc16_13TeV.411076.PhPy8EG_A14_ttbar_hdamp258p75_dil_BBFilt.deriv.DAOD_TOPQ1.e6798_s3126_r9364_p4514
mc16_13TeV.411077.PhPy8EG_A14_ttbar_hdamp258p75_dil_BFiltBBVeto.deriv.DAOD_TOPQ1.e6798_s3126_r9364_p4514
mc16_13TeV.411078.PhPy8EG_A14_ttbar_hdamp258p75_dil_CFiltBVeto.deriv.DAOD_TOPQ1.e6798_s3126_r9364_p4514
Reference
mc16_13TeV.410470.PhPy8EG_A14_ttbar_hdamp258p75_nonallhad.deriv.DAOD_TOPQ1.e6337_a875_r9364_p4514
mc16_13TeV.410471.PhPy8EG_A14_ttbar_hdamp258p75_allhad.deriv.DAOD_TOPQ1.e6337_a875_r9364_p4514
mc16_13TeV.411073.PhPy8EG_A14_ttbar_hdamp258p75_ljets_BBFilt.deriv.DAOD_TOPQ1.e6798_a875_r9364_p4514
mc16_13TeV.411074.PhPy8EG_A14_ttbar_hdamp258p75_ljets_BFiltBBVeto.deriv.DAOD_TOPQ1.e6798_a875_r9364_p4514
mc16_13TeV.411075.PhPy8EG_A14_ttbar_hdamp258p75_ljets_CFiltBVeto.deriv.DAOD_TOPQ1.e6798_a875_r9364_p4514
mc16_13TeV.411076.PhPy8EG_A14_ttbar_hdamp258p75_dil_BBFilt.deriv.DAOD_TOPQ1.e6798_a875_r9364_p4514
mc16_13TeV.411077.PhPy8EG_A14_ttbar_hdamp258p75_dil_BFiltBBVeto.deriv.DAOD_TOPQ1.e6798_a875_r9364_p4514
mc16_13TeV.411078.PhPy8EG_A14_ttbar_hdamp258p75_dil_CFiltBVeto.deriv.DAOD_TOPQ1.e6798_a875_r9364_p4514
Alternative
mc16_13TeV.410557.PowhegHerwig7EvtGen_H7UE_tt_hdamp258p75_704_SingleLep.deriv.DAOD_TOPQ1.e6366_a875_r9364_p4514
mc16_13TeV.410558.PowhegHerwig7EvtGen_H7UE_tt_hdamp258p75_704_dil.deriv.DAOD_TOPQ1.e6366_a875_r9364_p4514
mc16_13TeV.411082.PhHerwig7EG_H7UE_ttbar_hdamp258p75_ljets_BBFilt.deriv.DAOD_TOPQ1.e6799_a875_r9364_p4514
mc16_13TeV.411083.PhHerwig7EG_H7UE_ttbar_hdamp258p75_ljets_BFiltBBVeto.deriv.DAOD_TOPQ1.e6799_a875_r9364_p4514
mc16_13TeV.411084.PhHerwig7EG_H7UE_ttbar_hdamp258p75_ljets_CFiltBVeto.deriv.DAOD_TOPQ1.e6799_a875_r9364_p4514
mc16_13TeV.411085.PhHerwig7EG_H7UE_ttbar_hdamp258p75_dil_BBFilt.deriv.DAOD_TOPQ1.e6799_a875_r9364_p4514
mc16_13TeV.411086.PhHerwig7EG_H7UE_ttbar_hdamp258p75_dil_BFiltBBVeto.deriv.DAOD_TOPQ1.e6799_a875_r9364_p4514
mc16_13TeV.411087.PhHerwig7EG_H7UE_ttbar_hdamp258p75_dil_CFiltBVeto.deriv.DAOD_TOPQ1.e6799_a875_r9364_p4514
mc16_13TeV.411088.PhHerwig7EG_H7UE_ttbar_hdamp258p75_allhad_BBFilt.deriv.DAOD_TOPQ1.e6799_a875_r9364_p4514
mc16_13TeV.411089.PhHerwig7EG_H7UE_ttbar_hdamp258p75_allhad_BFiltBBVeto.deriv.DAOD_TOPQ1.e6799_a875_r9364_p4514
mc16_13TeV.411090.PhHerwig7EG_H7UE_ttbar_hdamp258p75_allhad_CFiltBVeto.deriv.DAOD_TOPQ1.e6799_a875_r9364_p4514
mc16_13TeV.410464.aMcAtNloPy8EvtGen_MEN30NLO_A14N23LO_ttbar_noShWe_SingleLep.deriv.DAOD_TOPQ1.e6762_a875_r9364_p4514
mc16_13TeV.410465.aMcAtNloPy8EvtGen_MEN30NLO_A14N23LO_ttbar_noShWe_dil.deriv.DAOD_TOPQ1.e6762_a875_r9364_p4514
mc16_13TeV.410466.aMcAtNloPy8EvtGen_MEN30NLO_A14N23LO_ttbar_noShWe_AllHadronic.deriv.DAOD_TOPQ1.e6762_a875_r9364_p4514
mc16_13TeV.412066.aMcAtNloPy8EG_A14_ttbar_hdamp258p75_ljets_BBFilt.deriv.DAOD_TOPQ1.e7129_a875_r9364_p4514
mc16_13TeV.412067.aMcAtNloPy8EG_A14_ttbar_hdamp258p75_ljets_BFiltBBVeto.deriv.DAOD_TOPQ1.e7129_a875_r9364_p4514
mc16_13TeV.412068.aMcAtNloPy8EG_A14_ttbar_hdamp258p75_ljets_CFiltBVeto.deriv.DAOD_TOPQ1.e7129_a875_r9364_p4514
mc16_13TeV.412069.aMcAtNloPy8EG_A14_ttbar_hdamp258p75_dil_BBFilt.deriv.DAOD_TOPQ1.e7129_a875_r9364_p4514
mc16_13TeV.412070.aMcAtNloPy8EG_A14_ttbar_hdamp258p75_dil_BFiltBBVeto.deriv.DAOD_TOPQ1.e7129_a875_r9364_p4514
mc16_13TeV.412071.aMcAtNloPy8EG_A14_ttbar_hdamp258p75_dil_CFiltBVeto.deriv.DAOD_TOPQ1.e7129_a875_r9364_p4514

Table 21: TOPQ1 DAOD list for $t\bar{t}$ + jets sample in this analysis.

1079 **A.4 $t\bar{t}H$**

1080 Table 22 is the TOPQ1 DAOD list for $t\bar{t}H$ sample in this analysis.

Nominal	
mc16_13TeV.346343.PhPy8EG_A14NNPDF23_NNPDF30ME_ttH125_allhad.deriv.DAOD_TOPQ1.e7148_s3126_r9364_p4514	
mc16_13TeV.346344.PhPy8EG_A14NNPDF23_NNPDF30ME_ttH125_semilep.deriv.DAOD_TOPQ1.e7148_s3126_r9364_p4514	
mc16_13TeV.346345.PhPy8EG_A14NNPDF23_NNPDF30ME_ttH125_dilep.deriv.DAOD_TOPQ1.e7148_s3126_r9364_p4514	
Reference	
mc16_13TeV.346343.PhPy8EG_A14NNPDF23_NNPDF30ME_ttH125_allhad.deriv.DAOD_TOPQ1.e7148_a875_r9364_p4514	
mc16_13TeV.346344.PhPy8EG_A14NNPDF23_NNPDF30ME_ttH125_semilep.deriv.DAOD_TOPQ1.e7148_a875_r9364_p4514	
mc16_13TeV.346345.PhPy8EG_A14NNPDF23_NNPDF30ME_ttH125_dilep.deriv.DAOD_TOPQ1.e7148_a875_r9364_p4514	
Alternative	
mc16_13TeV.346443.aMcAtNloPythia8EvtGen_ttH_noShWe_dilep.deriv.DAOD_TOPQ1.e7310_a875_r9364_p4514	
mc16_13TeV.346444.aMcAtNloPythia8EvtGen_ttH_noShWe_semilep.deriv.DAOD_TOPQ1.e7310_a875_r9364_p4514	
mc16_13TeV.346445.aMcAtNloPythia8EvtGen_ttH_noShWe_allhad.deriv.DAOD_TOPQ1.e7310_a875_r9364_p4514	
mc16_13TeV.346346.PhH7EG_H7UE_NNPDF30ME_ttH125_allhad.deriv.DAOD_TOPQ1.e7148_a875_r9364_p4514	
mc16_13TeV.346347.PhH7EG_H7UE_NNPDF30ME_ttH125_semilep.deriv.DAOD_TOPQ1.e7148_a875_r9364_p4514	
mc16_13TeV.346348.PhH7EG_H7UE_NNPDF30ME_ttH125_dilep.deriv.DAOD_TOPQ1.e7148_a875_r9364_p4514	

Table 22: TOPQ1 DAOD list for $t\bar{t}H$ sample in this analysis.

1081 A.5 $t\bar{t}V$

1082 Table 23 is the TOPQ1 DAOD list for $t\bar{t}V$ sample in this analysis.

Nominal	
mc16_13TeV.410155.aMcAtNloPythia8EvtGen_MEN30NLO_A14N23LO_ttW.deriv.DAOD_TOPQ1.e5070_s3126_r9364_p4514	
mc16_13TeV.410156.aMcAtNloPythia8EvtGen_MEN30NLO_A14N23LO_ttZnunu.deriv.DAOD_TOPQ1.e5070_s3126_r9364_p4514	
mc16_13TeV.410157.aMcAtNloPythia8EvtGen_MEN30NLO_A14N23LO_ttZqq.deriv.DAOD_TOPQ1.e5070_s3126_r9364_p4514	
mc16_13TeV.410218.aMcAtNloPythia8EvtGen_MEN30NLO_A14N23LO_ttee.deriv.DAOD_TOPQ1.e5070_s3126_r9364_p4514	
mc16_13TeV.410219.aMcAtNloPythia8EvtGen_MEN30NLO_A14N23LO_ttmumu.deriv.DAOD_TOPQ1.e5070_s3126_r9364_p4514	
mc16_13TeV.410220.aMcAtNloPythia8EvtGen_MEN30NLO_A14N23LO_ttautau.deriv.DAOD_TOPQ1.e5070_s3126_r9364_p4514	
mc16_13TeV.410276.aMcAtNloPythia8EvtGen_MEN30NLO_A14N23LO_tee_mll_1_5.deriv.DAOD_TOPQ1.e6087_s3126_r9364_p4514	
mc16_13TeV.410277.aMcAtNloPythia8EvtGen_MEN30NLO_A14N23LO_ttmumu_mll_1_5.deriv.DAOD_TOPQ1.e6087_s3126_r9364_p4514	
mc16_13TeV.410278.aMcAtNloPythia8EvtGen_MEN30NLO_A14N23LO_ttautau_mll_1_5.deriv.DAOD_TOPQ1.e6087_s3126_r9364_p4514	
Alternative	
mc16_13TeV.410142.Sherpa_NNPDF30NNLO_ttll_mll5.deriv.DAOD_TOPQ1.e4686_s3126_r9364_p4514	
mc16_13TeV.410143.Sherpa_NNPDF30NNLO_ttZnnqq.deriv.DAOD_TOPQ1.e4686_s3126_r9364_p4514	
mc16_13TeV.410144.Sherpa_NNPDF30NNLO_ttW.deriv.DAOD_TOPQ1.e4686_s3126_r9364_p4514	

Table 23: TOPQ1 DAOD list for $t\bar{t}V$ sample in this analysis.

1083 A.6 Single top

1084 Table 24 is the TOPQ1 DAOD list for single top sample in this analysis.

Nominal
mc16_13TeV.410644.PowhegPythia8EvtGen_A14_singletop_schan_lept_top.deriv.DAOD_TOPQ1.e6527_s3126_r9364_p4514
mc16_13TeV.410645.PowhegPythia8EvtGen_A14_singletop_schan_lept_antitop.deriv.DAOD_TOPQ1.e6527_s3126_r9364_p4514
mc16_13TeV.410646.PowhegPythia8EvtGen_A14_Wt_DR_inclusive_top.deriv.DAOD_TOPQ1.e6552_s3126_r9364_p4514
mc16_13TeV.410647.PowhegPythia8EvtGen_A14_Wt_DR_inclusive_antitop.deriv.DAOD_TOPQ1.e6552_s3126_r9364_p4514
mc16_13TeV.410658.PhPy8EG_A14_tchan_BW50_lept_top.deriv.DAOD_TOPQ1.e6671_s3126_r9364_p4514
mc16_13TeV.410659.PhPy8EG_A14_tchan_BW50_lept_antitop.deriv.DAOD_TOPQ1.e6671_s3126_r9364_p4514
Reference
mc16_13TeV.410644.PowhegPythia8EvtGen_A14_singletop_schan_lept_top.deriv.DAOD_TOPQ1.e6527_a875_r9364_p4514
mc16_13TeV.410645.PowhegPythia8EvtGen_A14_singletop_schan_lept_antitop.deriv.DAOD_TOPQ1.e6527_a875_r9364_p4514
mc16_13TeV.410646.PowhegPythia8EvtGen_A14_Wt_DR_inclusive_top.deriv.DAOD_TOPQ1.e6552_a875_r9364_p4514
mc16_13TeV.410647.PowhegPythia8EvtGen_A14_Wt_DR_inclusive_antitop.deriv.DAOD_TOPQ1.e6552_a875_r9364_p4514
mc16_13TeV.410658.PhPy8EG_A14_tchan_BW50_lept_top.deriv.DAOD_TOPQ1.e6671_a875_r9364_p4514
mc16_13TeV.410659.PhPy8EG_A14_tchan_BW50_lept_antitop.deriv.DAOD_TOPQ1.e6671_a875_r9364_p4514
Alternative
mc16_13TeV.410654.PowhegPythia8EvtGen_A14_Wt_DS_inclusive_top.deriv.DAOD_TOPQ1.e6552_s3126_r9364_p4514
mc16_13TeV.410655.PowhegPythia8EvtGen_A14_Wt_DS_inclusive_antitop.deriv.DAOD_TOPQ1.e6552_s3126_r9364_p4514
mc16_13TeV.411032.PowhegHerwig7EvtGen_H7UE_704_tchan_lept_antitop.deriv.DAOD_TOPQ1.e6719_a875_r9364_p4514
mc16_13TeV.411033.PowhegHerwig7EvtGen_H7UE_704_tchan_lept_top.deriv.DAOD_TOPQ1.e6719_a875_r9364_p4514
mc16_13TeV.411034.PhHerwig7EG_H7UE_singletop_schan_lept_top.deriv.DAOD_TOPQ1.e6734_a875_r9364_p4514
mc16_13TeV.411035.PhHerwig7EG_H7UE_singletop_schan_lept_antitop.deriv.DAOD_TOPQ1.e6734_a875_r9364_p4514
mc16_13TeV.411036.PowhegHerwig7EvtGen_H7UE_Wt_DR_inclusive_top.deriv.DAOD_TOPQ1.e6702_a875_r9364_p4514
mc16_13TeV.411037.PowhegHerwig7EvtGen_H7UE_Wt_DR_inclusive_antitop.deriv.DAOD_TOPQ1.e6702_a875_r9364_p4514
mc16_13TeV.412002.aMcAtNloPythia8EvtGen_HThalfscale_tW_inclusive.deriv.DAOD_TOPQ1.e6817_a875_r9364_p4514
mc16_13TeV.412004.aMcAtNloPy8EG_tchan_NLO.deriv.DAOD_TOPQ1.e6888_a875_r9364_p4514

Table 24: TOPQ1 DAOD list for single top sample in this analysis.

A.7 tH Table 25 is the TOPQ1 DAOD list for tH sample in this analysis.

Nominal
mc16_13TeV.346676.aMcAtNloPythia8EvtGen_tHjb125_4fl_CPalpha_0.deriv.DAOD_TOPQ1.e7815_a875_r9364_p4514
mc16_13TeV.346678.aMcAtNloPythia8EvtGen_tWH125_4fl_CPalpha_0.deriv.DAOD_TOPQ1.e7816_a875_r9364_p4514

Table 25: TOPQ1 DAOD list for tH sample in this analysis.**A.8 Rare t processes**Table 26 is the TOPQ1 DAOD list for rare t processes' sample in this analysis.

Nominal
mc16_13TeV.410560.MadGraphPythia8EvtGen_A14_tZ_4fl_tchan_noAllHad.deriv.DAOD_TOPQ1.e5803_s3126_r9364_p4514
mc16_13TeV.410408.aMcAtNloPythia8EvtGen_tWZ_Ztoll_minDR1.deriv.DAOD_TOPQ1.e6423_s3126_r9364_p4514
mc16_13TeV.412043.aMcAtNloPythia8EvtGen_A14NNPDF31_SM4topsNLO.deriv.DAOD_TOPQ1.e7101_a875_r9364_p4514

Table 26: TOPQ1 DAOD list for rare processes' sample in this analysis.

A.9 Vector bosons plus jets**A.9.1 $W + \text{jets}$** Table 27 is the TOPQ1 DAOD list for $W + \text{jets}$ sample in this analysis.

Nominal
mc16_13TeV.364170.Sherpa_221_NNPDF30NNLO_Wenu_MAXHTPTV0_70_CVetoBVeto.deriv.DAOD_TOPQ1.e5340_s3126_r9364_p4512
mc16_13TeV.364171.Sherpa_221_NNPDF30NNLO_Wenu_MAXHTPTV0_70_CFilterBVeto.deriv.DAOD_TOPQ1.e5340_s3126_r9364_p4512
mc16_13TeV.364172.Sherpa_221_NNPDF30NNLO_Wenu_MAXHTPTV0_70_BFilter.deriv.DAOD_TOPQ1.e5340_s3126_r9364_p4512
mc16_13TeV.364173.Sherpa_221_NNPDF30NNLO_Wenu_MAXHTPTV70_140_CVetoBVeto.deriv.DAOD_TOPQ1.e5340_s3126_r9364_p4512
mc16_13TeV.364174.Sherpa_221_NNPDF30NNLO_Wenu_MAXHTPTV70_140_CFilterBVeto.deriv.DAOD_TOPQ1.e5340_s3126_r9364_p4512
mc16_13TeV.364175.Sherpa_221_NNPDF30NNLO_Wenu_MAXHTPTV70_140_BFilter.deriv.DAOD_TOPQ1.e5340_s3126_r9364_p4512
mc16_13TeV.364176.Sherpa_221_NNPDF30NNLO_Wenu_MAXHTPTV140_280_CVetoBVeto.deriv.DAOD_TOPQ1.e5340_s3126_r9364_p4512
mc16_13TeV.364177.Sherpa_221_NNPDF30NNLO_Wenu_MAXHTPTV140_280_CFilterBVeto.deriv.DAOD_TOPQ1.e5340_s3126_r9364_p4512
mc16_13TeV.364178.Sherpa_221_NNPDF30NNLO_Wenu_MAXHTPTV140_280_BFilter.deriv.DAOD_TOPQ1.e5340_s3126_r9364_p4512
mc16_13TeV.364179.Sherpa_221_NNPDF30NNLO_Wenu_MAXHTPTV280_500_CVetoBVeto.deriv.DAOD_TOPQ1.e5340_s3126_r9364_p4512
mc16_13TeV.364180.Sherpa_221_NNPDF30NNLO_Wenu_MAXHTPTV280_500_CFilterBVeto.deriv.DAOD_TOPQ1.e5340_s3126_r9364_p4512
mc16_13TeV.364181.Sherpa_221_NNPDF30NNLO_Wenu_MAXHTPTV280_500_BFilter.deriv.DAOD_TOPQ1.e5340_s3126_r9364_p4512
mc16_13TeV.364182.Sherpa_221_NNPDF30NNLO_Wenu_MAXHTPTV500_1000.deriv.DAOD_TOPQ1.e5340_s3126_r9364_p4512
mc16_13TeV.364183.Sherpa_221_NNPDF30NNLO_Wenu_MAXHTPTV1000_E_CMS.deriv.DAOD_TOPQ1.e5340_s3126_r9364_p4512
mc16_13TeV.364156.Sherpa_221_NNPDF30NNLO_Wmumu_MAXHTPTV0_70_CVetoBVeto.deriv.DAOD_TOPQ1.e5340_s3126_r9364_p4512
mc16_13TeV.364157.Sherpa_221_NNPDF30NNLO_Wmumu_MAXHTPTV0_70_CFilterBVeto.deriv.DAOD_TOPQ1.e5340_s3126_r9364_p4512
mc16_13TeV.364158.Sherpa_221_NNPDF30NNLO_Wmumu_MAXHTPTV0_70_BFilter.deriv.DAOD_TOPQ1.e5340_s3126_r9364_p4512
mc16_13TeV.364159.Sherpa_221_NNPDF30NNLO_Wmumu_MAXHTPTV70_140_CVetoBVeto.deriv.DAOD_TOPQ1.e5340_s3126_r9364_p4512
mc16_13TeV.364160.Sherpa_221_NNPDF30NNLO_Wmumu_MAXHTPTV70_140_CFilterBVeto.deriv.DAOD_TOPQ1.e5340_s3126_r9364_p4512
mc16_13TeV.364161.Sherpa_221_NNPDF30NNLO_Wmumu_MAXHTPTV70_140_BFilter.deriv.DAOD_TOPQ1.e5340_s3126_r9364_p4512
mc16_13TeV.364162.Sherpa_221_NNPDF30NNLO_Wmumu_MAXHTPTV140_280_CVetoBVeto.deriv.DAOD_TOPQ1.e5340_s3126_r9364_p4512
mc16_13TeV.364163.Sherpa_221_NNPDF30NNLO_Wmumu_MAXHTPTV140_280_CFilterBVeto.deriv.DAOD_TOPQ1.e5340_s3126_r9364_p4512
mc16_13TeV.364164.Sherpa_221_NNPDF30NNLO_Wmumu_MAXHTPTV140_280_BFilter.deriv.DAOD_TOPQ1.e5340_s3126_r9364_p4512
mc16_13TeV.364165.Sherpa_221_NNPDF30NNLO_Wmumu_MAXHTPTV280_500_CVetoBVeto.deriv.DAOD_TOPQ1.e5340_s3126_r9364_p4512
mc16_13TeV.364166.Sherpa_221_NNPDF30NNLO_Wmumu_MAXHTPTV280_500_CFilterBVeto.deriv.DAOD_TOPQ1.e5340_s3126_r9364_p4512
mc16_13TeV.364167.Sherpa_221_NNPDF30NNLO_Wmumu_MAXHTPTV280_500_BFilter.deriv.DAOD_TOPQ1.e5340_s3126_r9364_p4512
mc16_13TeV.364168.Sherpa_221_NNPDF30NNLO_Wmumu_MAXHTPTV500_1000.deriv.DAOD_TOPQ1.e5340_s3126_r9364_p4512
mc16_13TeV.364169.Sherpa_221_NNPDF30NNLO_Wmumu_MAXHTPTV1000_E_CMS.deriv.DAOD_TOPQ1.e5340_s3126_r9364_p4512
mc16_13TeV.364184.Sherpa_221_NNPDF30NNLO_Wtaunu_MAXHTPTV0_70_CVetoBVeto.deriv.DAOD_TOPQ1.e5340_s3126_r9364_p4512
mc16_13TeV.364185.Sherpa_221_NNPDF30NNLO_Wtaunu_MAXHTPTV0_70_CFilterBVeto.deriv.DAOD_TOPQ1.e5340_s3126_r9364_p4512
mc16_13TeV.364186.Sherpa_221_NNPDF30NNLO_Wtaunu_MAXHTPTV0_70_BFilter.deriv.DAOD_TOPQ1.e5340_s3126_r9364_p4512
mc16_13TeV.364187.Sherpa_221_NNPDF30NNLO_Wtaunu_MAXHTPTV70_140_CVetoBVeto.deriv.DAOD_TOPQ1.e5340_s3126_r9364_p4512
mc16_13TeV.364188.Sherpa_221_NNPDF30NNLO_Wtaunu_MAXHTPTV70_140_CFilterBVeto.deriv.DAOD_TOPQ1.e5340_s3126_r9364_p4512
mc16_13TeV.364189.Sherpa_221_NNPDF30NNLO_Wtaunu_MAXHTPTV70_140_BFilter.deriv.DAOD_TOPQ1.e5340_s3126_r9364_p4512
mc16_13TeV.364190.Sherpa_221_NNPDF30NNLO_Wtaunu_MAXHTPTV140_280_CVetoBVeto.deriv.DAOD_TOPQ1.e5340_s3126_r9364_p4512
mc16_13TeV.364191.Sherpa_221_NNPDF30NNLO_Wtaunu_MAXHTPTV140_280_CFilterBVeto.deriv.DAOD_TOPQ1.e5340_s3126_r9364_p4512
mc16_13TeV.364192.Sherpa_221_NNPDF30NNLO_Wtaunu_MAXHTPTV140_280_BFilter.deriv.DAOD_TOPQ1.e5340_s3126_r9364_p4512
mc16_13TeV.364193.Sherpa_221_NNPDF30NNLO_Wtaunu_MAXHTPTV280_500_CVetoBVeto.deriv.DAOD_TOPQ1.e5340_s3126_r9364_p4512
mc16_13TeV.364194.Sherpa_221_NNPDF30NNLO_Wtaunu_MAXHTPTV280_500_CFilterBVeto.deriv.DAOD_TOPQ1.e5340_s3126_r9364_p4512
mc16_13TeV.364195.Sherpa_221_NNPDF30NNLO_Wtaunu_MAXHTPTV280_500_BFilter.deriv.DAOD_TOPQ1.e5340_s3126_r9364_p4512
mc16_13TeV.364196.Sherpa_221_NNPDF30NNLO_Wtaunu_MAXHTPTV500_1000.deriv.DAOD_TOPQ1.e5340_s3126_r9364_p4512
mc16_13TeV.364197.Sherpa_221_NNPDF30NNLO_Wtaunu_MAXHTPTV1000_E_CMS.deriv.DAOD_TOPQ1.e5340_s3126_r9364_p4512

Table 27: TOPQ1 DAOD list for $W + \text{jets}$ sample in this analysis.**A.9.2 $Z + \text{jets}$** 1093 Table 28 is the TOPQ1 DAOD list for $Z + \text{jets}$ sample in this analysis.

Nominal

Table 28: TOPQ1 DAOD list for $Z + \text{jets}$ sample in this analysis.

1094 A.10 Diboson

1095 Table 29 is the TOPQ1 DAOD list for diboson sample in this analysis.

Nominal
mc16_13TeV.364250.Sherpa_222_NNPDF30NNLO_llll.deriv.DAOD_TOPQ1.e5894_s3126_r9364_p4512
mc16_13TeV.364253.Sherpa_222_NNPDF30NNLO_lllv.deriv.DAOD_TOPQ1.e5916_s3126_r9364_p4512
mc16_13TeV.364254.Sherpa_222_NNPDF30NNLO_llvv.deriv.DAOD_TOPQ1.e5916_s3126_r9364_p4512
mc16_13TeV.364255.Sherpa_222_NNPDF30NNLO_lvvv.deriv.DAOD_TOPQ1.e5916_s3126_r9364_p4512
mc16_13TeV.364288.Sherpa_222_NNPDF30NNLO_llll_lowMllPtComplement.deriv.DAOD_TOPQ1.e6096_s3126_r9364_p4512
mc16_13TeV.364289.Sherpa_222_NNPDF30NNLO_lllv_lowMllPtComplement.deriv.DAOD_TOPQ1.e6133_s3126_r9364_p4512
mc16_13TeV.364290.Sherpa_222_NNPDF30NNLO_llvv_lowMllPtComplement.deriv.DAOD_TOPQ1.e6096_s3126_r9364_p4512
mc16_13TeV.363355.Sherpa_221_NNPDF30NNLO_ZqqZv.deriv.DAOD_TOPQ1.e5525_s3126_r9364_p4512
mc16_13TeV.363356.Sherpa_221_NNPDF30NNLO_ZqqZll.deriv.DAOD_TOPQ1.e5525_s3126_r9364_p4512
mc16_13TeV.363357.Sherpa_221_NNPDF30NNLO_WqqZvv.deriv.DAOD_TOPQ1.e5525_s3126_r9364_p4512
mc16_13TeV.363358.Sherpa_221_NNPDF30NNLO_WqqZll.deriv.DAOD_TOPQ1.e5525_s3126_r9364_p4512
mc16_13TeV.363359.Sherpa_221_NNPDF30NNLO_WpqqWmlv.deriv.DAOD_TOPQ1.e5583_s3126_r9364_p4512
mc16_13TeV.363360.Sherpa_221_NNPDF30NNLO_WplvWmqq.deriv.DAOD_TOPQ1.e5983_s3126_r9364_p4512
mc16_13TeV.363489.Sherpa_221_NNPDF30NNLO_WlvZqq.deriv.DAOD_TOPQ1.e5525_s3126_r9364_p4512
mc16_13TeV.363494.Sherpa_221_NNPDF30NNLO_vvvv.deriv.DAOD_TOPQ1.e5332_s3126_r9364_p4512
mc16_13TeV.364283.Sherpa_222_NNPDF30NNLO_llljjj_EW6.deriv.DAOD_TOPQ1.e6055_s3126_r9364_p4512
mc16_13TeV.364284.Sherpa_222_NNPDF30NNLO_llvjjj_EW6.deriv.DAOD_TOPQ1.e6055_s3126_r9364_p4512
mc16_13TeV.364285.Sherpa_222_NNPDF30NNLO_llvijj_EW6.deriv.DAOD_TOPQ1.e6055_s3126_r9364_p4512
mc16_13TeV.364287.Sherpa_222_NNPDF30NNLO_llvijj_ss_EW6.deriv.DAOD_TOPQ1.e6055_s3126_r9364_p4512
mc16_13TeV.345705.Sherpa_222_NNPDF30NNLO_ggllll_0M41130.deriv.DAOD_TOPQ1.e6213_s3126_r9364_p4512
mc16_13TeV.345706.Sherpa_222_NNPDF30NNLO_ggllll_130M41.deriv.DAOD_TOPQ1.e6213_s3126_r9364_p4512
mc16_13TeV.345723.Sherpa_222_NNPDF30NNLO_ggllvvZZ.deriv.DAOD_TOPQ1.e6213_s3126_r9364_p4512

Table 29: TOPQ1 DAOD list for diboson sample in this analysis.

1096 **B Signal/background comparisons**

1097 **B.1 BDT input variables**

1098 Figures 56(a) to Fig.56(n) compare the shape of the variables included in the BDT for all H^+ signal masses
1099 and background.

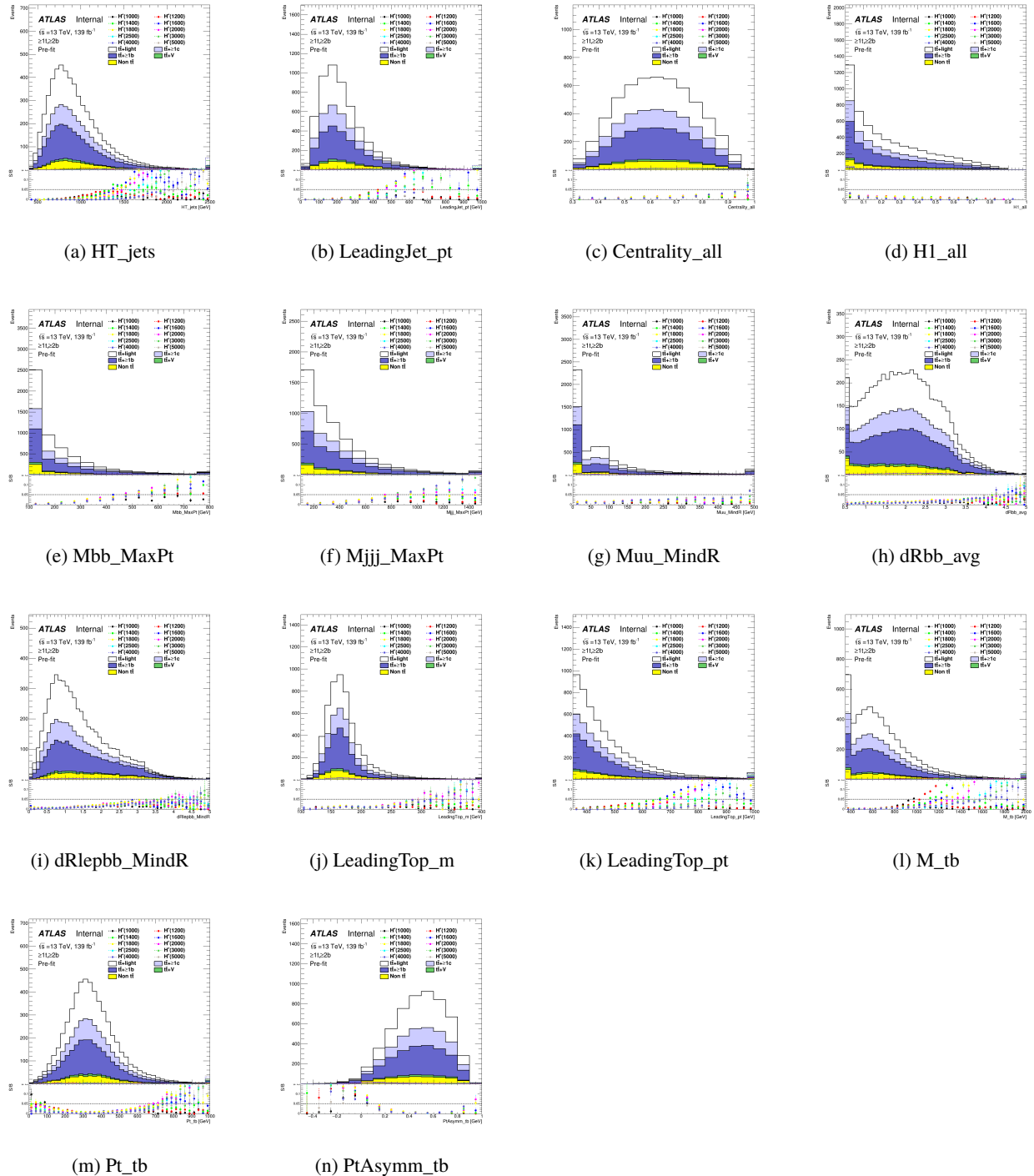
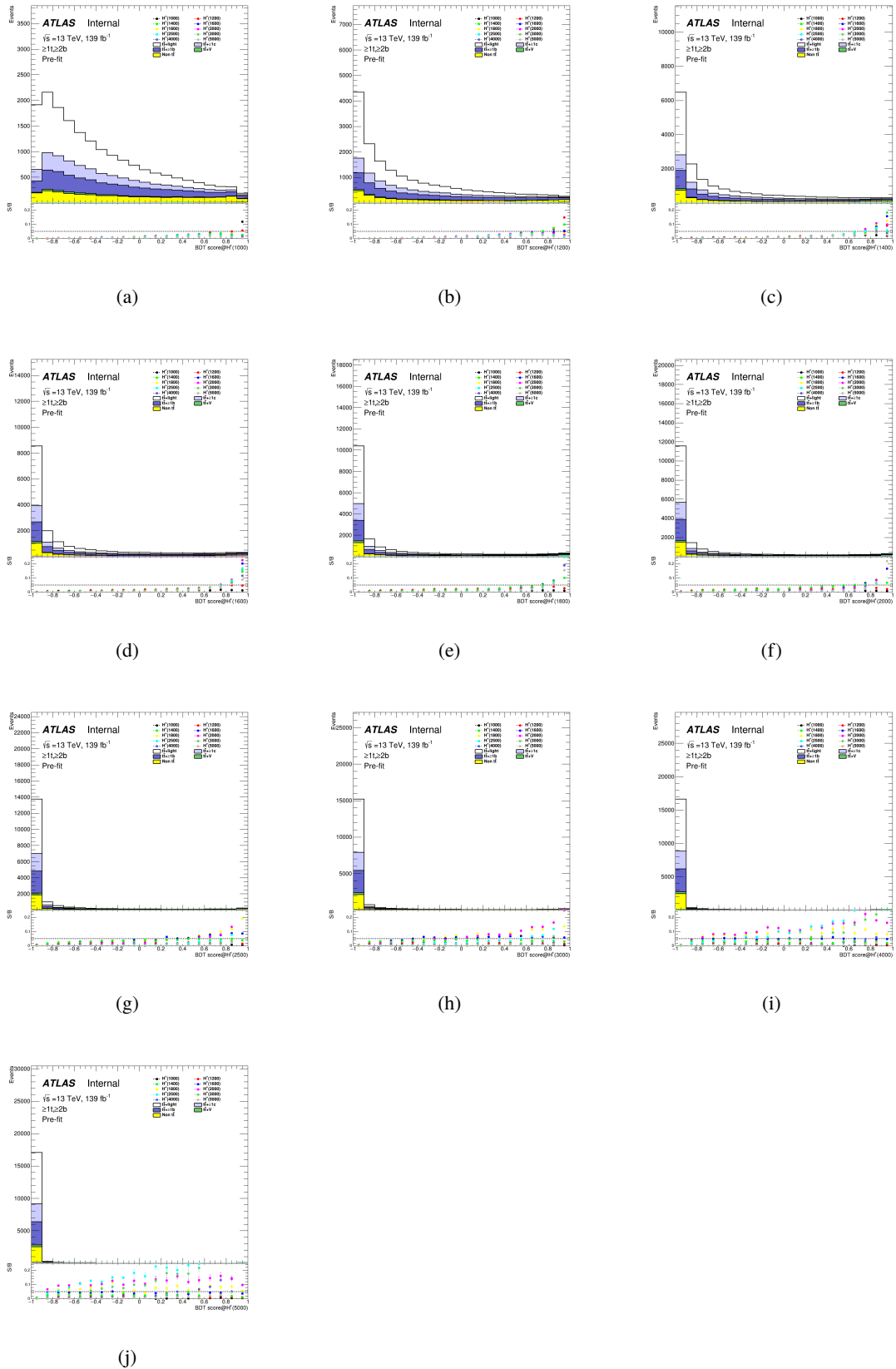


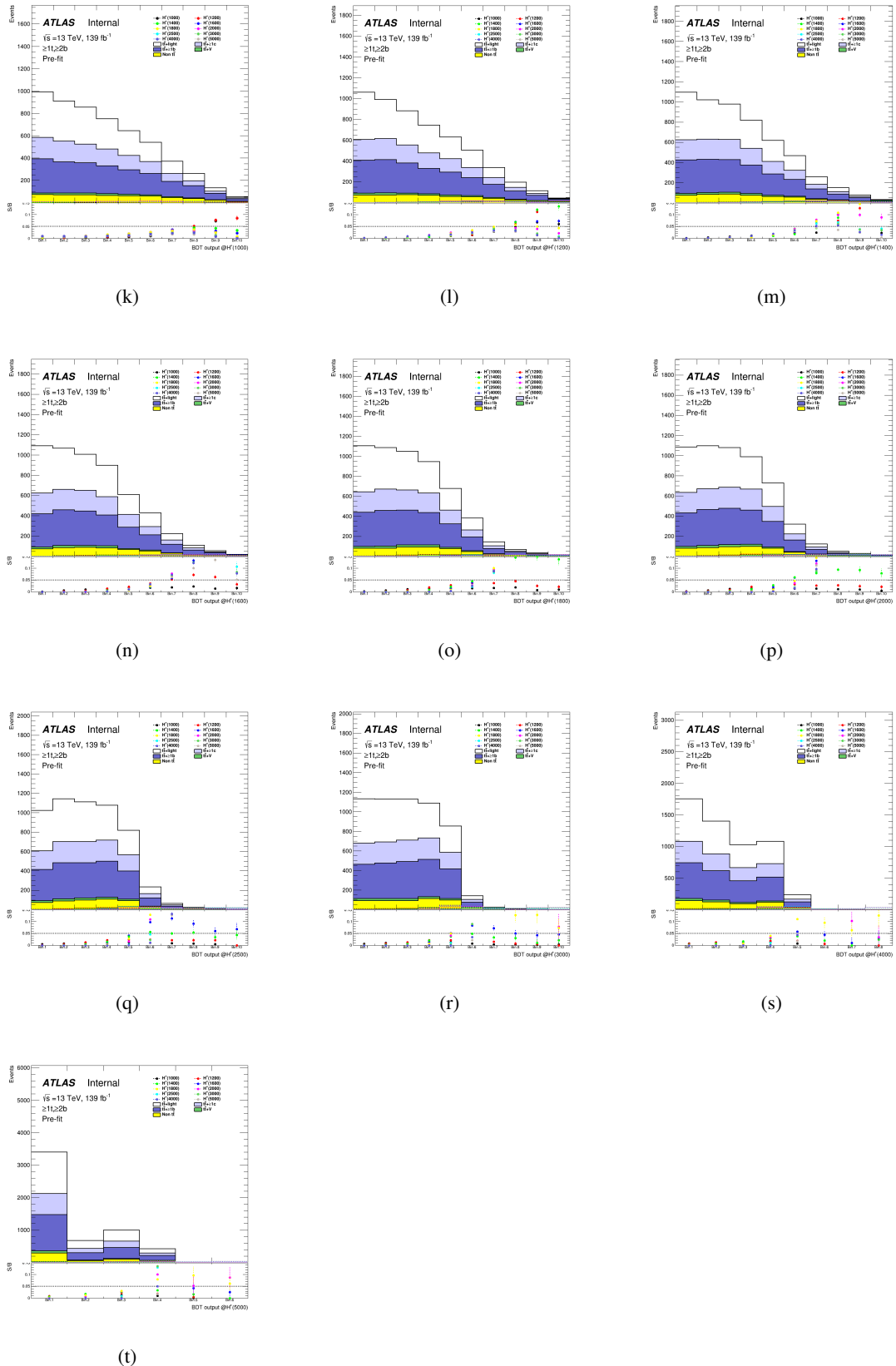
Figure 56: Comparison of the kinematic variables included in the BDT in the SR for the various H^+ signal masses between signal and background.

1100 B.2 BDT output

1101 Figures 57(a) to Fig.57(j) compare the shape of BDT output distribution in SR region between the signal
1102 and background on each H^+ signal mass hypothesis at equal bin intervals.



1103 Figures 57(k) to Fig.57(t) compare the shape of BDT output distribution in SR region between the signal
1104 and background on each H^+ signal mass hypothesis at not equal bin intervals. These binning is optimised
1105 using TRExFitter.



₁₁₀₆ **C Pruning**

₁₁₀₇ **C.1 Asimov fit**

₁₁₀₈ Figures 57 to 63 show the pruning applied in the systematic uncertainties for the Asimov fits for all the H^+
₁₁₀₉ mass fits.

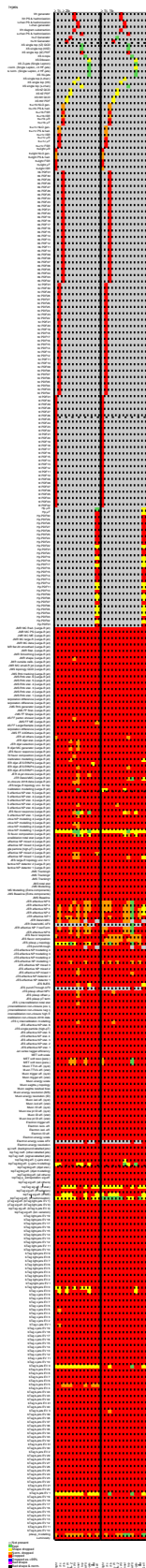


Figure 57: Pruned systematic uncertainties in the 1000 GeV H^+ mass Asimov fits

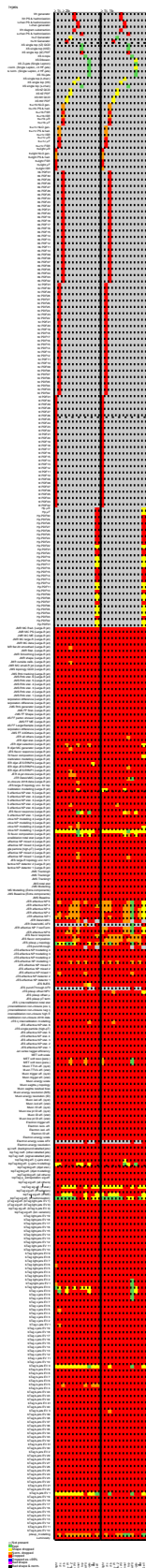


Figure 58: Pruned systematic uncertainties in the 1200 GeV H^+ mass Asimov fits

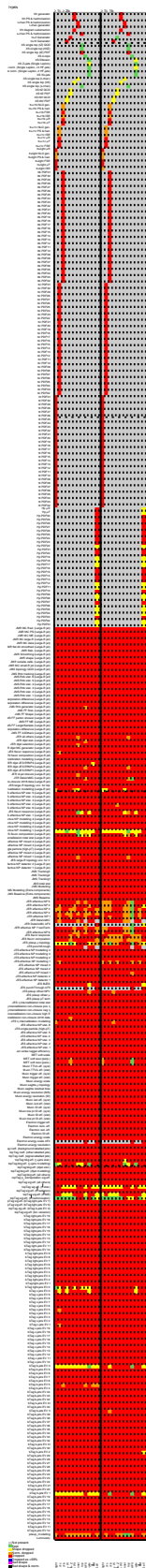


Figure 59: Pruned systematic uncertainties in the 1400 GeV H^+ mass Asimov fits

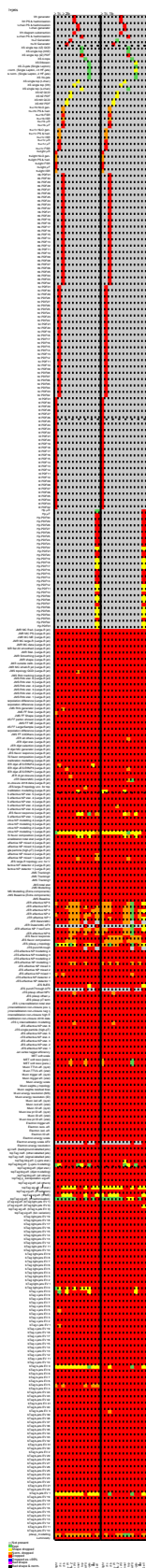


Figure 60: Pruned systematic uncertainties in the 1600 GeV H^+ mass Asimov fits

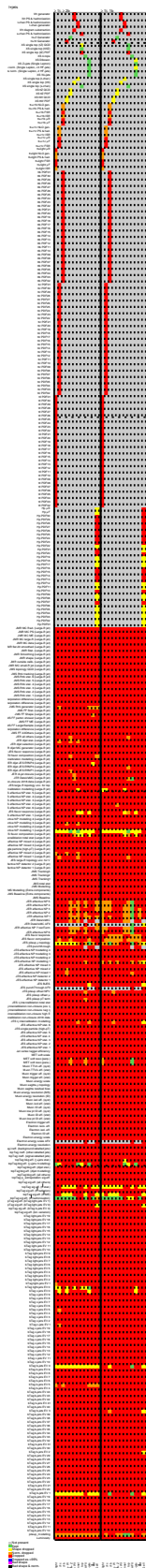


Figure 61: Pruned systematic uncertainties in the 2000 GeV H^+ mass Asimov fits

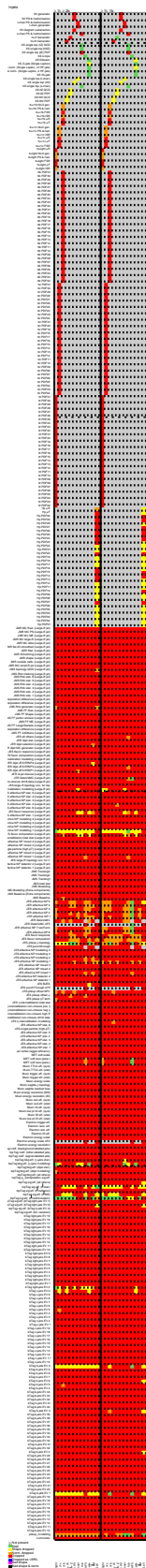


Figure 62: Pruned systematic uncertainties in the 2500 GeV H^+ mass Asimov fits

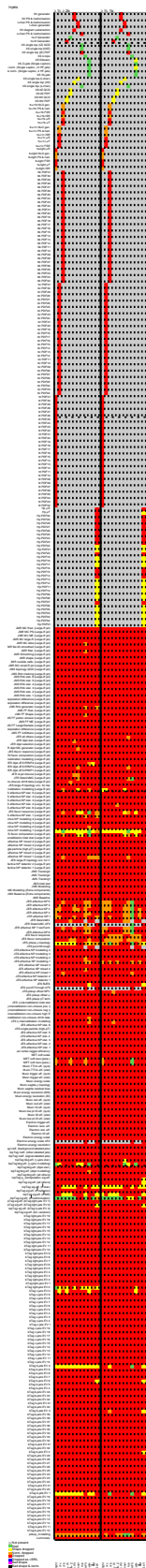


Figure 63: Pruned systematic uncertainties in the 3000 GeV H^+ mass Asimov fits